6-9-2016

Polarization characterization of nonlinear laser propagation

Shermineh Rostami

Shermineh Rostami

Candidate

Optical Science and Engineering

Department

This dissertation is approved, and it is acceptable in quality and form for publication:

Approved by the Dissertation Committee:

Jean-Claude M. Diels , Chairperson

Ladan Arissian

James L. Thomas

Martin C. Richardson

William P. Roach

Polarization characterization of nonlinear laser propagation

by

Shermineh Rostami

B.S., Physics, Tehran University 2005

M.S., Photonics, Laser and plasma research institute,

Shahid Beheshti University, 2008

DISSERTATION

Submitted in Partial Fulfillment of the

Requirements for the Degree of

Doctor of Philosophy

Optical Science and Engineering

The University of New Mexico

Albuquerque, New Mexico

May, 2016

Dedication

To my parents
Shahram Rostami and Shahrzad Movassaghi
and
my husband, Jeffrey B. Fairchild

Acknowledgements

Firstly, I would like to show my gratitude for my advisors Dr. Jean- Claude Diels and Dr. Ladan Arissian.

I'm very proud to be associated with Dr. Diels in the filamentation community as in my opinion he is one of the greatest minds in this field. His unbelievable enthusiasm for science and experimental physics has always been an inspiration for me.

I worked closely with Dr. Ladan Arissian and she helped me a lot during my PhD. Her great ideas and smart discussions about results kept me motivated.

I would like to thank Dr. James Thomas, Dr. Martin Richardson and Dr. Patrick Roach for accepting to be in my dissertation committee. Dr. Richardson and Dr. Roach have supported me throughout my graduate school and I am forever thankful to them.

I would like to show my appreciation for the help and support of my colleagues in Dr. Diels's research group. From the very early days of me joining the group, they all stepped in to help me in many different ways. Dr. Daniel Mirell and Dr. Rodrigo A. F. Inzunza helped me to get familiar with experimental optics. All the students and graduates from the group, Dr. Andreas Schmitt-Sody, Dr. Andreas Velten, Dr. Xiaozhen Xu, Dr. Koji Masuda, Dr.

Xuan Luo, Chengyong Feng, Brian Kamer, Amin Rasoulof, Ali Rastegari, Hanieh Afkhami, James Hendri and Ning Hsu, became my good friends who helped me to get comfortable in the Lab as well as in the group. I worked closely with Brian and Amin and all the long hours of doing experiments and brain storming wasn't possible without their help. Brian joined me for much of the polarization studies and together taking shifts for 10 days straight, we were able to complete one round of polarization studies. He was always around to help in the lab especially with the electronics and Labview. Amin started a series of experiments on filament emission (side, backward and forward) in parallel with my measurements and wasn't able to finish his work. When I picked up where he left off, he didn't leave any details out, explaining the whole experiment so I could move on quickly and finish a very nice team work (results presented in Section 6.2).

Dr. Andreas Schmitt-Sody and Dr. Andreas Velten have been collaborating with Dr.Diels after their graduation and together, with them and the entire filamentation team, we were able to perform promising sets of experiments and introduce a novel ultrafast method to characterize nonlinear laser propagation (presented in Section 6.4). I never forget their pep talks trying to keep me encouraged when things weren't going in the right direction, and I can't forget all the cupcakes and BBQs that we've had together.

I was also able to take advantage of working with Dr. Matthias Lenzner with his extraordinary patience and his love for teaching.

Sharing an office with Ali and Hanieh helped me to stay sane while writing my thesis. We probably annoyed a lot of people by talking a lot and laughing loudly.

I would like to thank all UNM (Physics and CHTM) facility team especially John DeMoss, Anthony Gravagne, Joel Straquadine, Mike and Lee. Sorry if I popped couple of fuses here and there. Joseph Sadler for taking care of our virtual world, Doris Williams for reminding us about all the important dates and seminars and having all the right answers to our academic problems. To Tamara Martinez, Jessica Breckenridge, Karen Walker and Juliet Montoya who always reminded me to not miss a deadline, especially when it came to purchasing close to the holidays and signing my contracts. Juliet's emails about food or cake in the lobby were my favorites.

I would also like to acknowledge our MURI collaborators, Dr. Eric Johnson and Dr. Tamar Seideman.

I can not thank Dr. Martin Richardson enough, for believing in me and giving me a great opportunity to join his team after my PhD. I'm very grateful to have met him and his wife Dr. Kathleen Richardson. They don't just have great minds, but they are true caring people and a constant reminder that "this is not just a job" but great things get accomplished when one feels as if they are part of a big family.

I worked with Dr. Michael Chini, Dr. Khan Lim and Dr. Matthieu Baudelet for a week in 2014 that lead to very interesting results (presented in Section 5.3).

The LPL family have supported me like one of their own since the first day I joined them in October 2015. Matthieu, Larry and Cheonha helped tremendously to make my transition to the real world with bigger responsibilities very smooth.

Dr. John Palastro patiently helped us with simulations and modeling in Sec-

tion 5.3 to be able to explain a very interesting and unexpected experimental observation.

I would also like to thank Dr. Mansoor Sheik-Bahae, Dr. Michael Hasselbeck, Dr. Denis Seletskiy and my friends Aram, Ali, Mehran and Ben for helping me to adapt to the new american lifestyle and not want to leave just because I was homesick. I met Dr. Mohammad Zonoubi at one of the first conferences I went to in the U.S.. Since the first time we met, he has helped me to meet new people in my field and create a strong network. I commend him for that quality as it's becoming a rare trait.

My extended family Shadi, Nader, Layla, Mina and Behshad have listened to all of my complaints during these years and they've been given me nothing but love and support. I especially thank Shadi and Nader for bringing Eliana to this world as she's been the joy of my life ever since. Lucas, Raleigh, Billy and Rachel became part of my family when I met my husband in 2011. They've been such good friends making my social life very interesting. Having them around helps me to escape my nerdiness sometimes. It's absolutely true that great friends are sometimes closer than family.

Starbucks has been a big part of my life and I want to thank their whole team all around the U.S. for providing me with tremendous dosage of caffeine when I needed to pull an all nighter, which was at least 25% of the time. Not to mention all the good memories.

I would'nt have been able to stay in the U.S. for all of these hard years to pursue my passion and career if it hadn't been for my parents. They sacrificed all they've had to see the success of their children and I don't even know how to begin thanking them. I hope they are as proud of me as I

am of them. My brothers Shahdad and Sajjad, my aunts Goli and Nahid, my uncle Shahriar and especially my grandparents have always shown me so much love to remind me I'm not alone in this world. My great uncles and aunts, Nasser, Jaleh, Sirous and Elfride have been a great support since I left my country and my family.

My mother in law Susie has been like a true mom to me since the day we met. She even insisted on sitting through the painful 45 minutes of my defense. She is one of the strongest and loving women I've ever known.

I'm especially thankful to UNM and their "end of the semester" parties that brought Jeff and I together. He's been behind me like a rock, truly in sickness and health. He always tells me that he is proud to have such a "brilliant" wife with "excellent" social skills. I am still alive because of him, literally!! He always made sure that I ate and slept when I was working so hard to the point that basic things in life didn't seem necessary.

I am extremely thankful to God for putting me in a path to meet all these great people. I went through a lot during these years and I know I am a better and stronger person for it. I've been told over and over that I should be really proud of myself for such a big accomplishment. To be honest, I am more proud to have tried my best to be an honest and caring person who has no fear of working to death towards her goals. I want to apologize to anybody whom I unintentionally hurt because I was so overwhelmed with work and life of a graduate student. I also want to thank all the people who never doubted my honesty and decency when I made mistakes and gave me the chance to make things right. I hope I can make a difference in this world by first being a decent human being and second a scientist.

Polarization characterization of nonlinear laser propagation

by

Shermineh Rostami

B.S., Physics, Tehran University 2005

M.S., Photonics, Laser and plasma research institute,

Shahid Beheshti University, 2008

PhD., Optical Science and Engineering, University of New Mexico, 2016

Abstract

High power laser pulses propagate nonlinearly in media transparent to their wavelength. Self-induced nonlinearities lead to strong modifications of the spatial, spectral as well as temporal characteristics of the pulse. The interaction of the high power laser pulses with the propagation medium leads to partial ionization of the latter. This highly complex and dynamic nonlinear process, induced by the high power laser pulses, with a narrow high intensity core that is maintained over long distances is known as "*filamentation*". Filaments created from a linearly polarized electric field have been studied by different research groups. However, it is interesting to know how the properties of the filament change with polarization and most importantly whether

the polarization state is maintained during the nonlinear propagation of the laser pulse.

This dissertation addresses the polarization evolution of a laser beam going through a nonlinear medium which can be expanded to filamentation. It is shown that the presence of the nonlinear interaction before the starting point of the filament, leads to polarization modification of an initially elliptically polarized light and the rotation of polarization ellipse with propagation can be used to measure the intensity.

Filaments generated in different gas media are also investigated to provide a better understanding of matter-light interaction when we deal with a highly nonlinear process such as filamentation. For gases such as N_2 and O_2, an extra component of optical nonlinearity due to the delayed rotational response (molecular alignment) is present which has been shown to have an effect on propagation and properties of the filament. Instabilities of the polarization of the filament lead to observation of an anomalous spectral broadening phenomenon due to molecular effects which is further investigated with a theoretical model.

This dissertation leads to recognition of polarization as a new dimension to characterize nonlinear laser propagation and facilitates polarization dependent applications such as THz emission and supercontinuum generation.

Contents

Contents

List of Figures

List of Figures

List of Figures

List of Figures

List of Figures

List of Figures

List of Figures

List of Figures

List of Figures

List of Tables

Chapter 1

Introduction

High power laser pulses propagate nonlinearly in media transparent to their wavelength. Self-induced nonlinearities lead to strong modifications of the spatial, spectral as well as temporal characteristics of the pulse. Self focusing, self guiding [19–21], four wave mixing [22], self phase modulation [23–25], self steepening [26–28] and pulse splitting [29] are some examples of these nonlinear processes. The interaction of the high power laser pulses with the propagation medium leads to partial ionization of the latter. [30–33]. The interest in filamentation and its unique applications has grown rapidly since Braun et al. [21] first reported on the observation of the air filaments with short pulses.

Filamentary propagation in gases, especially in atmosphere, is of great interest both from a fundamental and practical point of view. In the monatomic gas, self-focusing is caused by the instantaneous, electronic nonlinear optical response. For diatomic gases such as N_2 and O_2, an extra component of optical nonlinearity due to the delayed rotational response (molecular align-

ment) is present which has been shown to have an effect on propagation and properties of the filament.

Filaments created from a linearly polarized electric field have been studied by different research groups. However, it is crucial to know how the properties of the filament change with polarization and most importantly whether the polarization state is maintained during filamentation. There has been an ongoing controversy over stability of the polarization after a nonlinear process such as filamentation, started by Close et al. [34].

This dissertation will address the polarization evolution of a laser pulse, propagating through a nonlinear medium which can be expanded to filamentation. Filaments generated in different gas media are also investigated to provide a better understanding of matter-light interaction when we deal with a highly nonlinear process such as filamentation. To facilitate this study, different characterization tools and protocols have been developed (presented in chapter 2): an aerodynamic window to study the effect of nonlinear losses in the preparation phase of the filament, and a linear attenuator to make the filament measurements possible. A polarization measurement system was used to analyze the spatially and spectrally resolved polarization ellipse at different stages of the IR-filament. Chapter 3 introduces nonlinear ellipse rotation (NER) as a unique tool to measure the nonlinear index of refraction in different materials also to measure the intensity in the filament. Chapter 4 describes the evolution of the polarization in different stages of the filament (preparation, propagation and post filamentation) for different spatial and spectral components across the beam profile. Chapter 5 discusses the effect of polarization on the dynamics of the filaments prepared in vacuum or air

and propagated in air, molecular or atomic gasses. Chapter 6 is a study of plasma radiation from vortex filaments and molecular alignment enhanced ionization in the plasma.

The results and conclusions in this dissertation contribute to a better understanding of nonlinear laser propagation including filamentation, towards future applications.

1.1 Theory of filamentation

For a long time, Kerr focusing effect was believed to lead to a catastrophic collapse, inducing in turn a dense absorbing plasma, ruling out the propagation of intense ultrashort laser pulses in air. However, Braun et al. [21] reported in 1995 the first observation of self-channeling of GW laser in air for more than 20m. This new propagation regime where the laser beam does not experience diffraction over several meters was called "$filamentation$". Self-focusing by the Kerr effect and defocusing by the plasma were identified as the two main mechanisms driving this particular propagation regime.

The development of the chirped pulse amplification (CPA) technique [35, 36] has considerably transformed filament studies since it generates ultrashort laser pulses with high intensities. High power CPA lasers allow the observation of highly nonlinear propagation in media with weak nonlinearities such as air or atmospheric pressure gases.

Nevertheless, the development of applications of filamentation requires an understanding of the physical mechanisms involved. In the present document, we focus on the interaction between femtosecond IR filaments and

the media of preparation and propagation and how they affect the filament characteristics and properties.

1.1.1 Kerr self-focusing

At high powers (few GW in gases), the refractive index of a medium is modified by the Kerr effect [27, 28]; $n = n_0 + n_2 I(r,t)$, where n_0 and n_2 present the linear and nonlinear index of refraction and $I(r,t)$ intensity at a specific space and time. As the intensity of the laser beam is higher on axis than the periphery, the refractive index on axis is larger than on the side (assuming a Gaussian beam) (Fig. 1.1a). Since most materials have positive n_2, a radial gradient of refractive index similar to a converging lens is induced by the laser beam. If the beam power exceeds a critical value, P_{cr}, Kerr effect overcomes normal diffraction leading to self focusing and further increasing the intensity, to the point of collapse at a distance dependent on the initial beam characteristics (polarization, power, pulsewidth, chirp...). If Kerr self-focusing was the only process at play, it would lead to a collapse and prevent high power laser pulses from propagation in air. Richardson et al., were one of the first to report filamentation in gases. In their experiments the formation of a linear micron-scale filament in argon at the focus of a single-mode ruby laser having Rayleigh diameter more than 10× larger, was observed [37].

As mentioned above, the power at which self-focusing and linear diffraction will balance each other is called "critical power". There have been different approaches to define the critical power [38] which lead to $P_{cr} = 2-3.2GW$ in air at 800 nm [39–42]. The critical power for a perfect Gaussian, CW beam

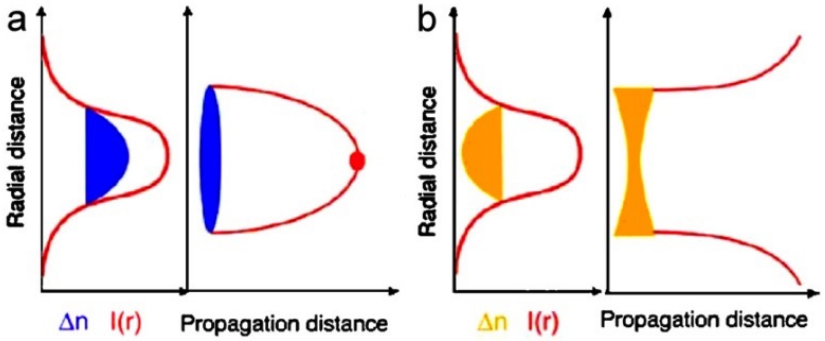

Figure 1.1: (a) Kerr self-focusing and beam collapse. (b) Beam defocusing due to ionization at the non-linear focus [1].

is commonly shown by [42]

$$P_{cr} = \frac{3.77\lambda^2}{8\pi n_0 n_2} \tag{1.1}$$

Pulse compression and splitting [43–45] during filamentation result in spectral broadening, leading to a higher threshold for self-focusing [46] than for CW pulses [40, 47]. A recent work reported the value of critical power between 13 and 20GW [48], which is in agreement with our observation in the lab; we don't see a filament with a power below 36GW. The self-focusing distance for a CW Gaussian beam follows [40]

$$L_{sf} = \frac{0.367\frac{ka_0^2}{2}}{\sqrt{[\sqrt{P/P_{cr}} - 0.852]^2 - 0.0219}} \tag{1.2}$$

with k being the wavenumber of the electromagnetic field and a_0 the radius (at $1/e^2$ of the peak intensity) of the laser beam. In a laboratory setting, the beam is commonly focused using optics of focal length f, modifying the self-focusing distance L'_{sf} as [49]

$$\frac{1}{L'_{sf}} = \frac{1}{f} + \frac{1}{L_{sf}} \tag{1.3}$$

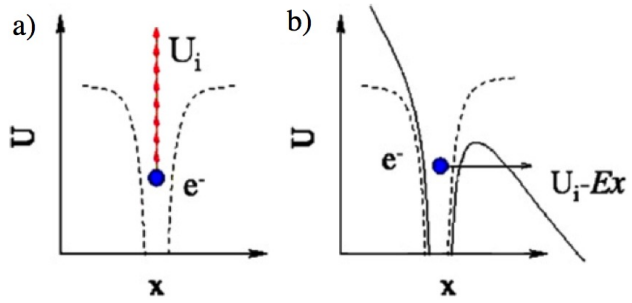

Figure 1.2: Schematic of: (a) multiphoton and (b) tunnel ionization [1].

1.1.2 Plasma generation

Once self-focusing starts, the beam size keeps reducing and increasing the intensity in the beam. The ionization of the medium implies the absorption of a large number of photons $K \approx U_i/\hbar\omega_0$. When the beam approaches collapse, the pulse intensity reaches $10^{13} - 10^{14}$ W/cm^2 and ionization becomes possible. Photo-ionization includes both multiphoton (MPI) and tunnel ionization.

The MPI occurs when multiple photons are simultaneously absorbed by the electron, providing enough energy to overcome the ionization potential U_i (Fig. 1.2a). In air, oxygen is the first ionized constituent with $U_i \approx 12eV$. Photons in 800nm beam each have energy $\hbar\omega \approx 1.55$eV, therefore 8 photons are enough to overcome U_i. The MPI rate scales as I^K with $K \sim 8$ oxygen at 800 nm. Nitrogen, with ionization energy of 15.6 eV will require 11 photons to be ionized in a filament and its contribution is negligible.

Tunnel ionization is described as the escape of an electron across the highly perturbed barrier of Coulomb potential of the nucleus and occurs at higher intensities (Fig. 1.2b). The typical length for multiphoton absorption can be

presented as

$$L_{MPA} = \frac{1}{2K\hbar\omega_0\sigma_K I^{K-1}\rho_{atm}} \tag{1.4}$$

where σ_K is the ionization cross section and ρ_{atm} the atom density. The intensity of the pulse, I, is attenuated by a factor $[(K+1)/2]^{1/(K-1)}$ over this length. Typical values for 800 nm filaments in air (K = 8, $\sigma_8 = 3.7 \times 10^{-96}$ $\mathrm{cm}^{16}/\mathrm{W}^8/\mathrm{s}$), are $L_{MPA} \sim 160\mu m$ for I $=5 \times 10^{13}\mathrm{W/cm}^2$ [1].

The Keldysh parameter γ, determines the dominant photo-ionization regime in laser filamentation:

$$\gamma = \frac{\omega}{e}\sqrt{\frac{m_e U_i n_0 c\epsilon_0}{I}} \tag{1.5}$$

with ω being the angular frequency, e and m_e the charge and mass of the electron, U_i the potential energy, c and ϵ_0 the speed of light in vacuum and the permittivity of free space respectively. MPI is the main ionization process with $\gamma >> 1$, tunneling ionization is the dominant process otherwise. It has been shown that the approximation of the ionization by MPI for the case of 800nm filaments in air, $\gamma \approx 1.8$, provide a good agreement with experimental results [50, 51]. In a more recent study by Arissian et al. [52] it was demonstrated that for $0.58 \leq \gamma \leq 1.53$, tunneling ionization is dominant at 800nm.

The evolution equation for the electron density can be presented as:

$$\frac{\partial\rho}{\partial t} = \sigma_K I^K(\rho_{nt} - \rho) + \frac{\sigma}{U_i}\rho I \tag{1.6}$$

with ρ_{nt} being the density of neutrals in the medium, σ the cross section for inverse Bremsstrahlung. The free electrons generated by the filament reduce

the index of refraction of the medium as [53, 54]:

$$n(r,t) \approx n_0 - \frac{\rho(r,t)}{2\rho_c} \tag{1.7}$$

with $\rho(r,t)$ being the density of free electrons at a specific space and time, and $\rho_c = \epsilon_0 m_e \omega_0^2 / e^2$ ($\sim 1.7 \times 10^{21} cm^{-3}$ at 800nm) the value of the critical plasma density (plasma becomes opaque above this value).
The change in the refraction index due to the generated plasma acts as a diverging lens, counteracting the collapse of the beam (Fig. 1.1b).

1.2 Filament models

Considerable number of models and numerical simulations have been developed to explain nonlinear laser propagation and filamentation. In the following sections, some of the presented models will be discussed briefly.

1.2.1 Moving focus model

One of the first theories to explain the appearance of filamentation was the moving focus model. In this model the laser pulse could be viewed as a longitudinal stack of temporal slices that will act independently of each other [26, 55, 56]. The slices that have powers above the critical power P_{cr} (see Section 1.1.1) will have foci positioned at different locations along the length of the filament (Fig. 1.3).
Nonlinear effects generated by the preceding portions of the self-focusing parts of the pulse such as plasma formation and GVD are not considered in this model. The nonlinear foci are successively positioned before the geomet-

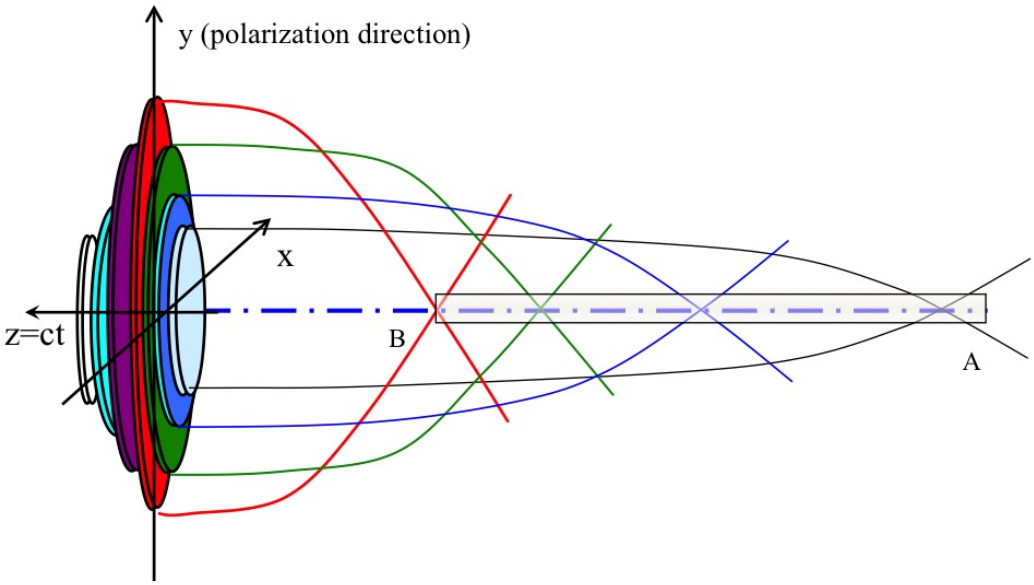

Figure 1.3: Presentation of the moving focus model (Courtesy of J.-C. Diels).

ric focus [57]. Any forward propagation beyond the geometric focus is then not expected which contradicts with many experimental studies.

Once the intensity becomes high enough to overcome the ionization threshold of the medium, coupling between the trailing time slices is induced. Energy can propagate beyond the linear focus since the collapse of the slices in the trail of the pulse is delayed by this coupling.

1.2.2 Self guiding model

The self-guiding model goes beyond the moving focus model, taking into account different linear and nonlinear processes that create the dynamic focusing and defocusing of the beam. This model was proposed based on a balance between self-focusing and the combination of normal diffraction and

plasma defocusing [21].

Creating the filament from a focus in the transition between vacuum and air (see Section 2.1.3) agrees only with this model. Another model that was proposed recently by Loriot et al. (HOKE [58]) and has raised a lot of controversy, is based on self-guiding by higher orders of n_2. This model claims that the higher orders with negative sign, rather than the plasma, contribute to defocusing.

1.2.3 Dynamic spatial replenishment

The dynamic spatial replenishment model was introduced by Mlejnek et al. [59, 60]. Plasma is generated in the wake of the leading peak of the self-focused pulse, causing the trail of the pulse to defocus. The leading edge becomes less intense simultaneously, due to multi-photon absorption, turning off the plasma generation letting the beam to re-focus if the remaining power is still above the critical value. These focusing, de-focusing events will continue until there is an exhaustion of power in the pulse due to the nonlinear losses (see Section 5.1 for more details). The absorption of photons by MPI or generation of longer pulsewidths by GVD, effectively lower the peak power in temporal slices to a point that they may no longer exceed the P_{cr}.

1.2.4 Bessel beam model

It was shown by Dubietis et al. that the filament is sustained by the energy flux from the periphery of the beam [61]. Their numerical study in the CW case accounts only for Kerr focusing, diffraction and nonlinear losses. In this approach the guiding effect is induced as a result of the spontaneous transfor-

mation of a Gaussian beam into a conical wave according to the principles of maximum stationarity, maximum localization and minimum nonlinear losses. To understand the difference between self guiding (Section 1.2.2) and Bessel beam model qualitatively, "the stationary approach of Akhmanov" [41, 62, 63] can be used [2]. This theory relies on Maxwell's equation, representing a continuous beam in cylindrical symmetry and in the slowly varying envelope approximation [2]:

$$2i\partial_z \tilde{E}_n = (\frac{\partial^2}{\partial r^2} + \frac{1}{r}\frac{\partial}{\partial r})E_n + \mid E_n \mid^2 E_n - \frac{\gamma_k}{2}E_n^{2K-2}E_n \tag{1.8}$$

with the electric field of the light being written as $E(t,z) = 1/2\tilde{E}(z)$ $\exp(i\omega t - kz) + c.c.$, $\tilde{E}_n = \tilde{E}(z)/E_0$ the electric field complex envelope normalized to a field $E_0 = \sqrt{\eta_0/n_2}$ (η_0 is the characteristic impedance of the medium, and $n_2 I = n_2 \mid \tilde{E}(z) \mid^2 /(2\eta_0)$ the nonlinear index of refraction). The higher order nonlinear term, $\frac{\gamma_k}{2}E_n^{2K-2}E_n$, is written in a form suggested by Dubietis et al. [61]

The two main approaches to model filamentation can be differentiated using the equation above. The key is the parameter γ_k, including high orders of nonlinearities. The plasma channel-based model relies on a real value for this parameter, inducing self-defocusing to counter the Kerr effect (Fig. 1.4a). The other approach is based on an imaginary value for γ_k. This represents absorption by MPA, leading to the creation of a conical phase front that distributes the intensity like a Bessel beam [61, 64, 65]. This controversy between the two models has been resolved in solids and liquids in favor of the Bessel beam model [66]. In an attempt by Diels et al. [2] to find out which models explain the filamentation process accurately, the mechanism of plasma confinement was confirmed and the formation of a Bessel beam wasn't

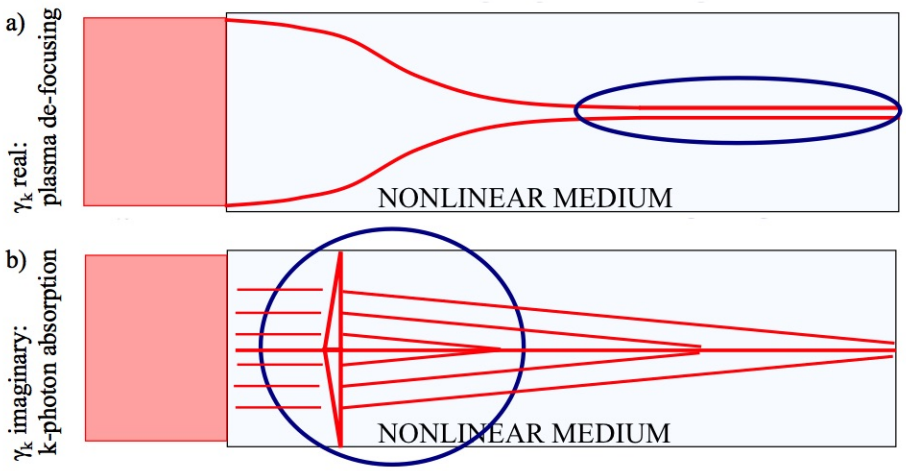

Figure 1.4: Filamentation according to (a) the self-guiding model, and (b) the Bessel beam model (Courtesy of J.-C. Diels) [2].

excluded. In order to evaluate the Bessel beam theory, the filament should be launched in vacuum after preparation in air, eliminating the medium required to create a waveguide.

1.2.5 Theoretical Model, Nonlinear Schrödinger Equation

The evolution of the filament can be derived from the nonlinear Schrödinger equation (NLSE) and using the slowly varying envelop (SVE) approximation. For electric field envelope $E(r, z, t)$ in the reference frame that's moving at

the group velocity [59, 67]:

$$\frac{\partial E}{\partial z} = \frac{i}{2k}(\frac{\partial^2}{\partial r^2} + \frac{1}{r}\frac{\partial}{\partial r})E - \frac{ik''}{2}\frac{\partial^2 E}{\partial t^2} - \frac{\sigma}{2}(1 + i\omega\tau)\rho E - \frac{\beta^{(K)}}{2} \mid E \mid^{2K-2} (1 - \frac{\rho}{\rho_{nt}})E + ik_0(1-f)n_2 \mid E \mid^2 E + ik_0 f n_2[\int_{-\infty}^{\infty} R(t-t') \mid E(t') \mid^2 dt']E \quad (1.9)$$

"The terms on the right hand side represent diffraction, GVD, defocusing due to free electrons in the plasma, multi-photon absorption and nonlinear self focusing". $k = n\omega/c$ is the wavenumber, ω the optical frequency, $k'' = \partial^2 k/\partial\omega^2$, σ the inverse Bremsstrahlung cross-section, τ the electron collision time, ρ the electron density, $\mid E \mid^2$ the intensity, $\beta^{(K)}$ the K-photon absorption coefficient, ρ_{nt} density of neutrals and $n_2 \mid E \mid^2$ is the nonlinear index of refraction for a continuous wave. "$R(t)$ is the normalized response function that accounts for delayed molecular Raman Kerr" with f to repartition the Kerr effect to the instantaneous electronic Kerr and the delayed rotational Raman scattering. The evolution of the electron density is described by Eq. 1.6. Some typical values for air with ionization energy of $E_g = 11\text{eV}$ are, $\beta^{(K)} = K\hbar\omega_0\rho_{nt}\sigma_K$ with $K = 7$ for the order of MPA and $\beta^{(7)} = 6.5 \times 10^{-104}$ $\text{m}^{11}/\text{W}^{-6}$ [59]. Also $\tau = 3.5 \times 10^{-13}\text{s}$, $\sigma = 5.1 \times 10^{-24}\text{m}^2$ [53] and $k'' = 2\text{fs}^2\text{cm}^{-1}$. $R(t) = \frac{\Gamma^2 - \omega_R^2}{\omega_R^2}\exp(-\Gamma t)\sin(\omega_R t)$ where Γ^{-1} is the typical molecular response time and ω_R the molecular rotational frequency. In atmospheric conditions, $\Gamma = 1/70$ fs, $\omega_R = 16 \times 10^{12}$ s^{-1} and $f = 0.5$ has been shown to provide a good fit [68].

1.3 Properties of filaments

Intensity clamping, As mentioned above, MPI starts when the beam is intense enough to create free electrons. Self-focusing is saturated locally by the generation of electron density and by defocusing the beam, limits the peak intensity inside the filament. The clamping intensity can be estimated through this simple idea, which is about ($\approx 1.8 \times 10^{13}$W/cm^2 for a 800nm pulse with $t_p = 100$fs pulse duration) [5, 6, 21]. The filament contains a limited amount of power, roughly equal to P_{cr} [21]. The transverse size of a filament was first measured by Diels et al. [2] using a linear attenuator, to be 200μm for filaments prepared in vacuum (see Section 2.1.3) and 200-300 μm for air filaments. Another evidence of the clamping intensity was obtained from analyzing the supercontinuum generated in water and glass by filaments [69]. The energy independence of the maximum blue shift, due to self-phase modulation, above a critical value was explained by the clamping phenomenon.

Despite these claims, Diels et al. [2] showed that for focusing in vacuum, while higher intensities may be reached at the vacuum-air transition, the clamping intensity still applies to the filament. Intensity in the filament was also measured in this work (see Section 3.3.2) to be one order of magnitude higher than the "published" value for intensity clamping.

Self phase modulation, Self phase modulation (SPM) refers to the temporal variation of the refractive index induced by the time dependent intensity as $n = n_0 + n_2 I(r,t)$ leading to generation of new frequencies in the spectrum of the laser pulse. The link between intensity of the pulse and the

instantaneous frequencies can be shown as [1]:

$$\omega(t) = -\frac{\partial \phi}{\partial t} \sim \omega_0 - \frac{n_2 \omega_0}{c} z \frac{\partial I(r,t)}{\partial t} \tag{1.10}$$

The front part of the pulse, interacting with a Kerr medium, generates redder frequencies and the bluer frequencies are created by the back part. Self-phase modulation along with other nonlinear processes (to be explained later in this section) is responsible for creating a broad continuum covering the range from visible to IR.

Self-steepening, Intensity dependent change of the refractive index leads to the peak intensity of the pulse having smaller velocity than the trailing edge [70]. For a Gaussian pulse, the GVD slows down the front part of the pulse, forming a steep edge in the trailing part [1]. Self- steepening slows down the self-focusing of the leading part of the pulse compare to the trailing part generating shorter wavelengths in the steep trailing edge [71]. Self-steepening can also be a result of the correction to the SVEA, which has been shown to create an optical shock at the trailing edge of the pulse [72].

Self-compression, Competition between several effects in filamentation leads to a significant pulse duration shortening. Nearly single optical cycle pulses can be produced from pulses with an initial duration of a few tens of femtoseconds [73]. The experimental generation of atto-second XUV pulses has been benefited from the filament induced pulse self-compression [74, 75].

Chirp, The adjustment of both the peak power and pulse duration during experiments with CPA lasers is usually achieved by chirping the pulse using the final compression stage. Chirping the pulse initially and SPM induced chirp (an intrinsically chirped process), may have different effects even for short propagation distances.

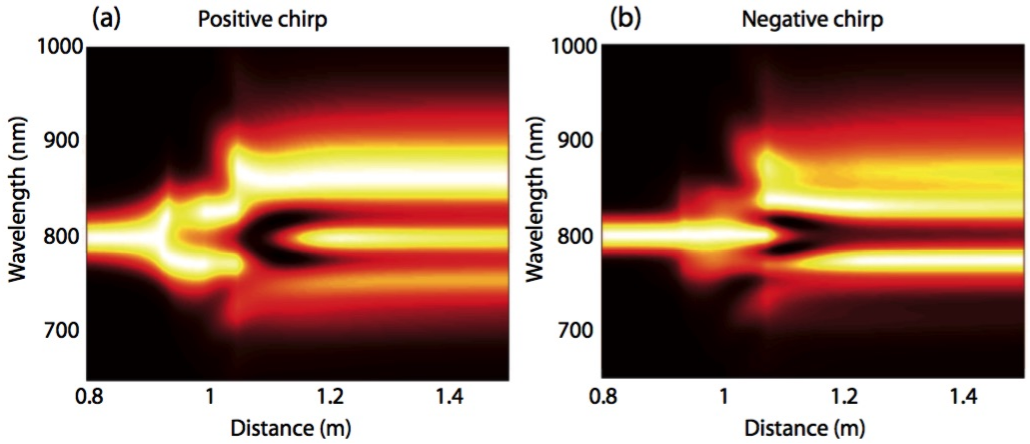

Figure 1.5: "Spectral broadening for a) positively (b) and negatively chirped pulses as a function of the propagation distance" [3].

For a positively chirped pulse, the redder spectral components are located in the temporal front-end of the pulse and experience a red shift due to the intrinsic chirped nature of self-phase modulation. This process leads to broadening of the spectrum and consequently depletion of the central frequency (Fig. 1.5a). On the contrary, this red shift reinforces the central frequency for negatively chirped pulses (Fig. 1.5b) [3]. The effect of chirp on the fluorescence from the filament plasma is briefly addressed in Section 5.2.
Supercontinuum, Filaments prepared in a nonlinear medium are accompanied by a strong spectral broadening, characterized by a white core surrounded by colored rings referred as conical emission. The field at the raising edge is red-shifted while the trailing edge is blue-shifted. A combination of several nonlinear effects such as SPM, self-steepening and ionization of the medium are responsible for the spectral broadening. Self-steepening of the pulse and ionization of the medium, induced by self-focusing, amplify the

spectral broadening compared to SPM acting alone [76–79]. The conversion rate into supercontinuum varies from a few tenth of percent to a significant fraction of the initial energy for an initially collimated or a convergent beam, respectively [1]. Generation of supercontinuum could be used to extract shorter pulses from a filament [51, 74, 80, 81], also allows filaments to be used in spectroscopy and sensing applications [82]. Supercontinuum generated from a 800nm single filament in molecular and atomic gasses with different initial conditions is studied in Section 5.5.

1.3.1 Filament plasma

The plasma channel is intrinsic to the filament, supporting its existence as well as providing information about it. The filament induced plasma channel can also be used in different unique applications such as microwave guiding [83–85], discharge guiding [86–89], and condensation [90–92].

The plasma channel has an emission lifetime of several nanoseconds after the laser pulse. The electronic density in the plasma channel is typically between 10^{16} and 10^{17}cm^{-3}, and depending on the focusing conditions can be significantly different [93].

Clean fluorescence, The emission from the nitrogen molecules excited by MPI is one of the main indicators of air ionization. The fluorescence spectra of molecules are much cleaner than those obtained with longer pulses, due to the absence of emission from atomic lines and the hot plasma [6, 9, 11, 94]. Breakdown can't occur in the case of short pulses since the pulse is not long enough to allow any collisional absorption of the light through inverse

Bremsstrahlung. Plasma emission from nitrogen molecules is studied in Section 5.2 which provides valuable information about the effect of different variables in creating and propagating femtosecond filaments.

THz emission, Filament induced plasma in gases emit a broadband EMP of radiation in the direction transverse to the propagation of the filament [95]. THz pulses have the potential to combine identification through spectroscopy and safe-to-use high-resolution imaging. Conventionally generated THz pulses from emitters such as nonlinear crystals or semiconductor antenna can not propagate over a long distance in the atmosphere (due to beam diffraction and strong attenuation due to water vapor), making the femtosecond laser remote filamentation in gases, especially in air, a promising alternative THz generation source. Remarkable properties of the filaments such as mode improvement, pulse self-compression and spectrum broadening as well as creating a clean florescence make it a unique source for applications [96].

1.4 Applications of filamentation

1.4.1 Guiding applications

It has been shown that the plasma column generated by the filament can be used as a conductive channel to guide an electrical current [97–102]. If the plasma channel is dense, persistent and long enough (100's of meters), these filaments can be used to trigger and guide a lightning strike in a pre-existing lightning conditions. Protection of people and properties from lightning is the main purpose for laser induced lightning. However, guiding through the

atmosphere has been challenging since it requires maintaining the plasma channel for a sufficient length in both time and space. In a smaller scale, this guiding property of the filament induced plasma can be used to trigger spark gaps [86] and generate ad-hoc antennas [88].

Filaments are capable of guiding electromagnetic radiation along their length (typically in the radio-frequency range) [103–105]. The RF waves, having frequencies lower than the frequency of the filament induced plasma, can be trapped and guided in a conductive barrier created by a dense ring of filaments [83, 84]. It was also shown that virtual hyperbolic metamaterials created by an array of plasma channels can be used to manipulate microwave beams in air [85].

1.4.2 Remote sensing applications

Filaments are ideal for remote sensing applications due to their ability to convey high intensity and fluence over long distances, as well as the generation of a broad supercontinuum [9, 106].

Absorption LIDAR measurements can be used for atmospheric chemical analysis, collecting the backscattered supercontinuum light after being selectively absorbed by the molecules. This filament-based LIDAR technique has been demonstrated by identifying the absorption lines of water vapor and oxygen in the atmosphere [82, 107], as well as the possibility of detecting trace gases [108].

The laser-induced breakdown spectroscopy (LIBS) technique can be extended to filament induced breakdown spectroscopy (FIBS) [109], using a filament

as the source instead of the focused nanosecond pulse. Filamentation makes it possible to deliver the intensities needed for LIBS over long range of propagation allowing this analysis to be performed as a stand-off technique [110–114].

Chapter 2

Experimental section

2.1 Filament formation

2.1.1 UNM's laser

The majority of the experiments presented in this thesis were performed with a 800 nm commercial system (Coherent HIDRA) at UNM. Two different outputs from this system are available to use:

- Full-energy line: 10 Hz repetition rate, ∼40 fs pulse duration, ∼ 50 mJ pulse energy.
- Kilohertz line: 1 kHz repetition rate, ∼40 fs pulse duration, ∼1 mJ pulse energy.

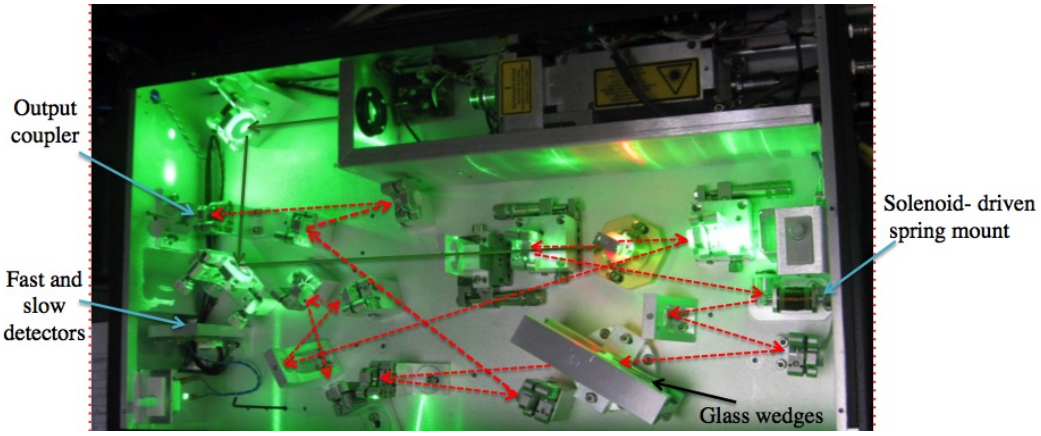

Figure 2.1: Picture of the oscillator (Mantis), used in the CPA system at UNM. Both pump and 800nm beam paths are shown with the appropriate colored arrows. One of the mirrors is mounted on a solenoid- driven spring to change the cavity length and initiate the Kerr lens modelocking. The net dispersion can be finely controlled with the glass wedges included in the cavity. There are 2 detectors installed in the oscillator that are used to monitor the power (slow detector) and for the RF synch, monitoring the pulse train and triggering the timing box (SDG).

HIDRA sub-systems

Oscillator, The oscillator (Mantis-5) is a modelocked Ti:sapphire laser system producing broad-band pulses centered around 800nm. The design incorporates a Coherent Optically Pumped Semiconductor (OPS) pump laser (5W) and negative dispersion mirror technology into a single compact laser head and power supply (Fig. 2.1).

The output of the Mantis is normally around 300-400 mW at the repetition rate of 80 MHZ with about 70nm band-width (FWHM).

Stretcher, In order to be able to amplify laser pulses without destroying the optics, they (out of the oscillator) need to be stretched to maintain a low

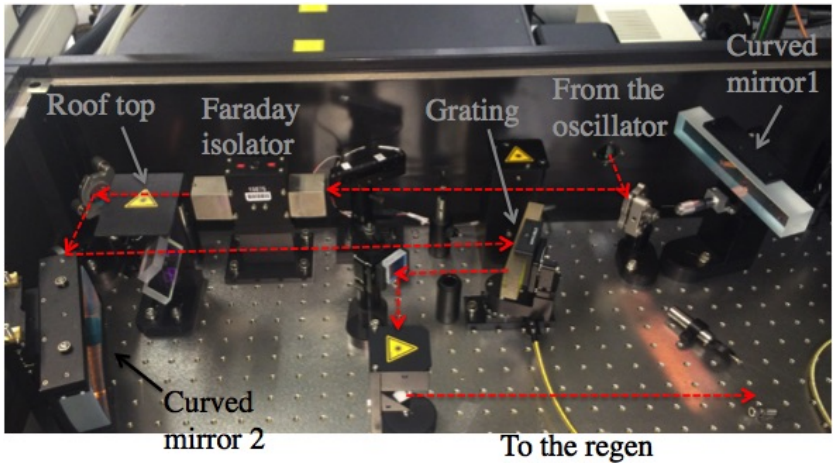

Figure 2.2: Picture of the stretcher between the oscillator and regen. Red arrows show the beam path going in and out of the stretcher. 2 curved mirrors and the roof top provide the 4 passes to the grating to ensure the spatial reconstruction of the stretched beam.

peak power during the amplification process. The stretcher consists of a 1200 line/mm grating and 0.5 meter focusing mirror to stretch the pulse to up to 100 ps (Fig 2.2). The grating is setup such that the redder frequencies travel a shorter distance through the stretcher than the bluer components resulting in redder components to exit first; therefore the pulse has been stretched.

Regenerative amplifier, The regenerative amplifier (or "regen") with a Ti:sapphire gain medium is directly pumped from one side. The transmitted green from the crystal is collected using a mirror and reflected back to the gain medium. The pump (Evolution-15) is a diode-pumped intra-cavity doubled Q-switched Nd:YLF laser emitting about 8 W (right before the crystal) of 527nm pulses at 1kHz.

The principle of regen amplifier is to confine, by polarization, a single pulse, amplify it and cavity dump the output. Two Pockels cells in the cavity which

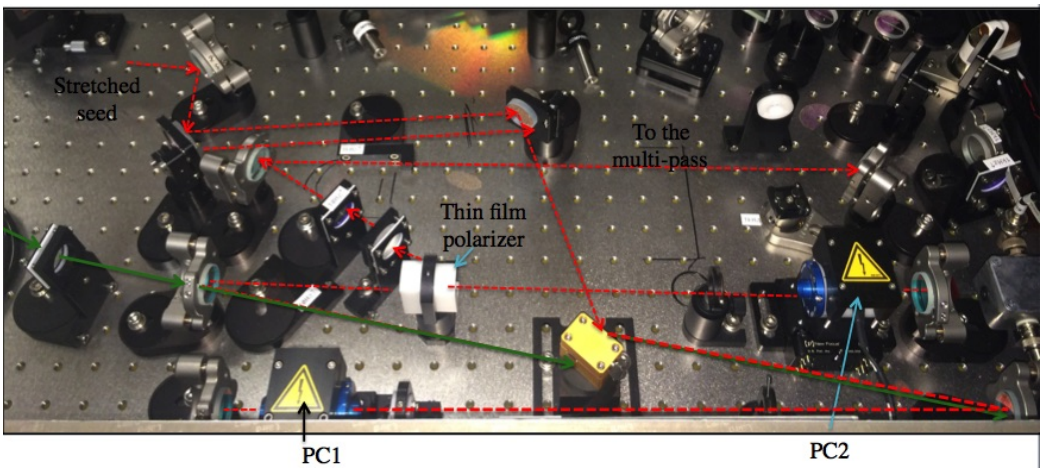

Figure 2.3: Picture of the regen amplifier consisting of 2 Pockels cells in the laser cavity with a Ti:Sapphire crystal as the gain medium. The crystal is pumped with a kHz Evo-15. The output of the regen after passing a telescope is sent to either the compressor for the final 1kHz output or to the second stage amplifier for the 10Hz operation.

allow the amplification of one pulse in the cavity and ejection of the output after amplification, can operate at 1kHz or 10Hz (Fig. 2.3). The seed pulse energy is amplified to ∼2.1W and sent through a telescope to increase the beam size and then to either the compressor for the 1kHz operation or the multi-pass amplifier for the full energy, 10Hz operation.

Multi-pass amplifier, In the case of full energy operation which is at 10 Hz repetition rate, the output of the regen amplifier is sent to the second stage amplifier. Multi-pass consists of a Ti:sapphire crystal which is pumped at 10 Hz from one side. The 10 Hz pump used in this CPA system is a Q-switch Nd:YAG Continuum Surelite II with a single rod oscillator design and 260mJ output at 532nm. Second stage of amplification (to about 60mJ) is done in 4 passes through the crystal. The amplified output is sent to the

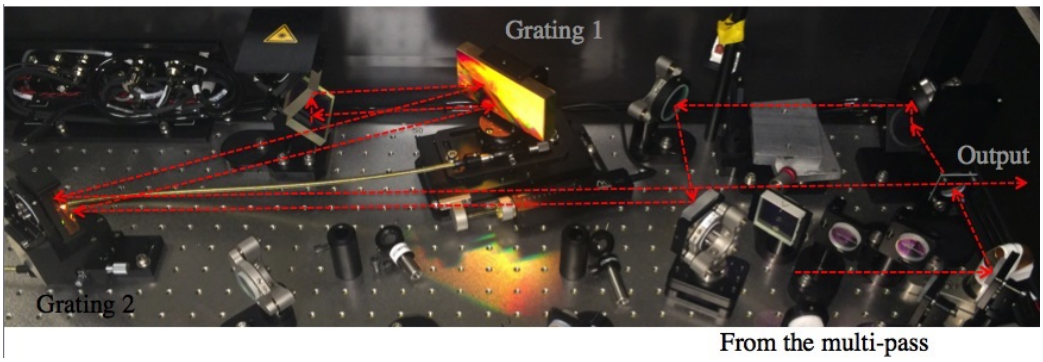

Figure 2.4: Picture of UNM's compressor.

compressor to create femtosecond pulses.

Compressor, The amplified laser pulse is recompressed back to the original pulsewidth by going through the grating based compressor (reversal process of stretching)(Fig. 2.4). Compressor includes two 1500 line/mm gratings, placed parallel to each other. The output of the compressor is about 40 fs, and ∼50mJ for the 10Hz beam and ∼1 mJ for the 1kHz operation.

SDG (Synchronization and Delay Generator), Amplification in both stages is dependent on the precise coordination of the modelocked seed (from Mantis), amplifier pump (Evolution and Surelite) and regen's Pockels cells which control pulse injection and ejection. The SDG accepts inputs from the seed laser (from the fast detector inside the Mantis box) and pump lasers, and outputs a trigger signal for each Pockells cell at an adjustable delay. Additional delay signals (8 total) are available for synchronization with diagnostics equipments and /or other aspects of an experiment. The trigger frequency can be divided from 1 to 1023 for output on selected channels. This feature is used to switch between 10Hz and 1kHz outputs. More details on this system can be found in the manuals provided by Coherent.

2.1.2 UCF's laser

The Multi-Terawatt Filamentation Laser (MTFL) system is a Chirped Pulse Amplification (CPA) system capable of delivering ultrashort pulses with high enough energy for long range, multi-filament applications. This laser was used for the supercontinuum and ellipticity measurements performed in Section 5.3. A detailed description of this laser can be found in reference [12].

2.1.3 Aerodynamic window

Self-focusing of the pulse in air will induce filamentation to begin at a distance that changes with beam characteristics (polarization, energy, chirp, etc.) but always prior to the geometrical focus. To control the definite start point for the filaments, a unique tool that had been developed in Diels's research group is used [2, 115].

The pulse is focused in vacuum and launched into air at a point that the beam waist is already about the filament size (100-200μm). This transition between vacuum and air should be through a substrate that does not suffer from significant nonlinear effects or damage that could potentially disturb or interrupt the filamentation process. An aerodynamic window is used for this transition, since no solid or liquid substance is known to possess these properties.

The main feature of an aerodynamic window is a supersonic air flow that runs through an engineered channel (Fig. 2.5) creating a pressure gradient separating the low pressure vacuum chamber (below 35 Torr) from atmo-

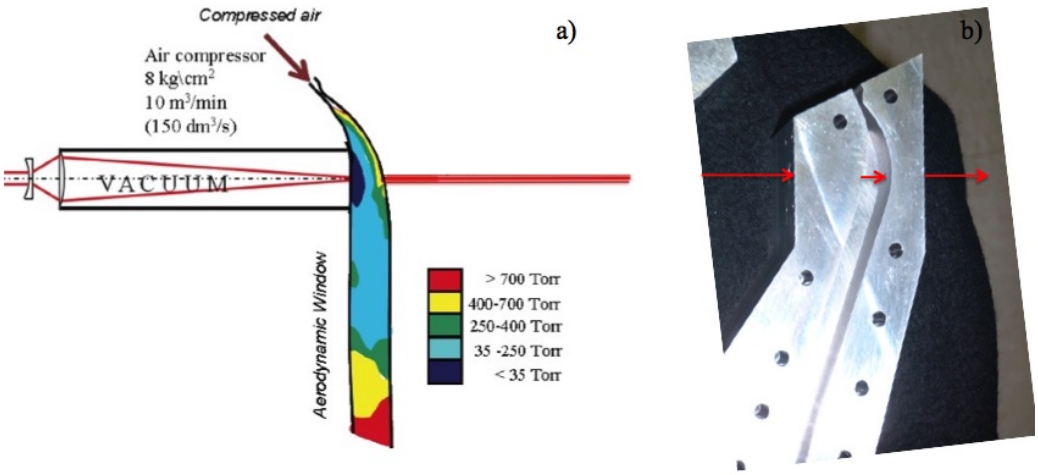

Figure 2.5: a) schematic of the aerodynamic window with the color coded pressure gradient b) picture of the cross section of the window.

spheric pressure. Color coding in Fig. 2.5a indicates the pressure in different parts of the aerodynamic window.

In the measurements performed in the loose focusing condition (3m), a 2.8m vacuum tube is placed collinear with the beam path on the vacuum side of the window which makes focusing in vacuum possible (Fig. 2.5a). The pressure in the transition region is brought down to 8 Torr where the pulse is focusing, using the supersonic flow of air through the window, combined with a vacuum pump attached to the tube [115]. This pressure is low enough to eliminate the significant nonlinear effects that might otherwise take place during the focusing process in air. Using the aerodynamic window in creating the filament rules out all the models except self- induced guiding (see Section 1.2). A 6mm thick BK7 substrate was chosen as an entrance window to the tube. A telescope was used to create the 3m focal length to avoid creating white light in the entrance window at higher energies.

2.2 Diagnostics

2.2.1 Linear attenuation

One of the challenges in the filamentation studies is to experimentally measure the electric field of a filament. Linear attenuation of the field is required for any reliable measurement. One solution, introduced by Diels et al. [2], is a large diameter coated mirror with a maximum reflectivity at grazing incidence. A standard coated Nd:YAG mirror (maximum reflectivity for 1.06 μm with s-polarization at normal incidence) was shown to have a transmission of less than 0.5×10^{-6} at 89° incidence. This method of attenuation is nevertheless limited to linearly s-polarized beams and basically acts as a polarizer.

The other solution is a thin fused silica plate at grazing incidence. This method was used to observe the first UV filaments [116] and also employed by other groups. Self phase modulation and the wavefront distortion can be minimized by using a thin plate ($\leq$ 1mm). In the measurements reported in this document, a 3 inch fused silica plate with thickness of $1mm$ at grazing incidence ($\theta_i \approx 87°$) was used to attenuate the beam. Since the transmission of the plate is polarization dependent, calibration based experimental measurement of weak field was performed (following section).

2.2.2 Polarization measurement technique

One of the main goals in this thesis is the polarization measurement along nonlinear laser propagation with different initial conditions. The initial polarization of the laser beam is controlled by a wave plate (HWP/QWP). In

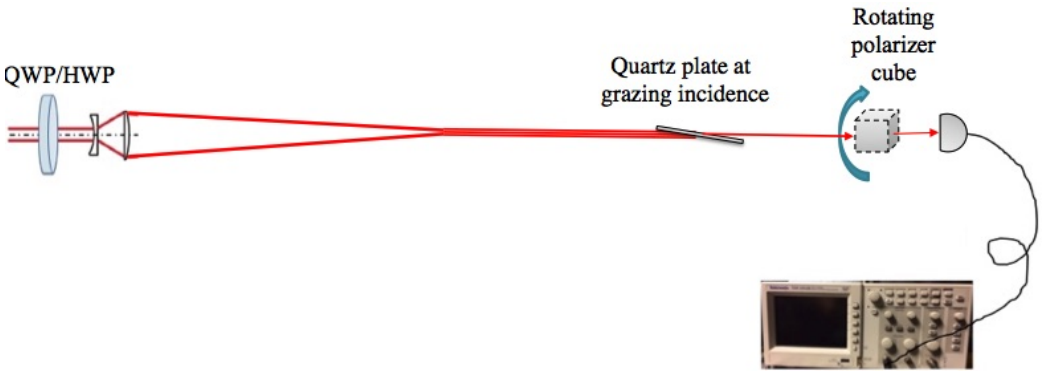

Figure 2.6: Schematic of the polarization measurement apparatus. A QWP/HWP is used to control the initial polarization of the laser. Attenuated beam after a 1mm thickness quartz plate at grazing incidence is sent to a rotating polarizer cube. The polarization ellipse is retrieved using the transmission of the cube, rotating incrementally.

the experiments involving measurements of the high intensity beam, a thin quartz plate (see Section 2.2.1) at grazing incidence is used to attenuate the beam, prior to analysis by a rotating polarizing cube (Fig. 2.6). The projected polarization is measured over 180° degrees of rotation of the polarizer cube (with 2° increments), and detected by a silicon photodetector (Newport 818-SL) that is sensitive from 400 to 1100nm. This detector is connected to an oscilloscope (Tektronix TDS 1012B) which is triggered at the repetition rate of the laser (using one of the outputs of the SDG box (see Section 2.1.1)). An example of the measured signal from the scope for different angles of the cube is shown in Fig. 2.7.

The polarization state of a polarized beam can be written as a "Jones vector":

$$\mathbf{E} = \begin{bmatrix} E_x \\ E_y e^{i\delta} \end{bmatrix} \tag{2.1}$$

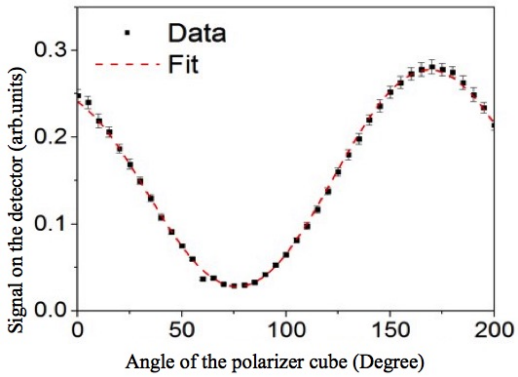

Figure 2.7: An example of the measured signal from the scope and the fit using our algorithm. This example is from the measurements done in Section 5.3 [4].

that represents an electric field vector tracing out an ellipse with symmetry axis inclined at a general angle (α) relative to the x, y-coordinate system (Fig. 2.8). The angle between major axis of the ellipse and a horizontal line, "α", defines the orientation of the polarization ellipse as

$$\tan(2\alpha) = \frac{2E_x E_y \cos\delta}{E_x^2 - E_y^2} \tag{2.2}$$

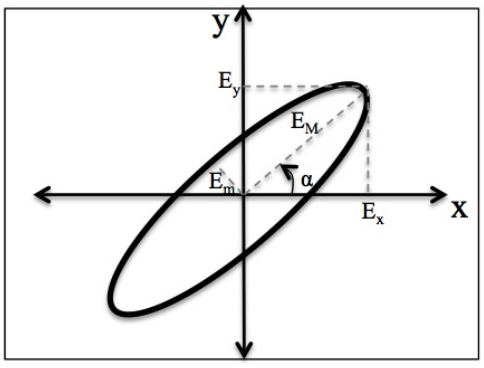

Figure 2.8: The polarization ellipse is defined in space with its ellipticity ($\epsilon = E_m/E_M$), and the angle of major axis with respect to the horizontal axis (α).

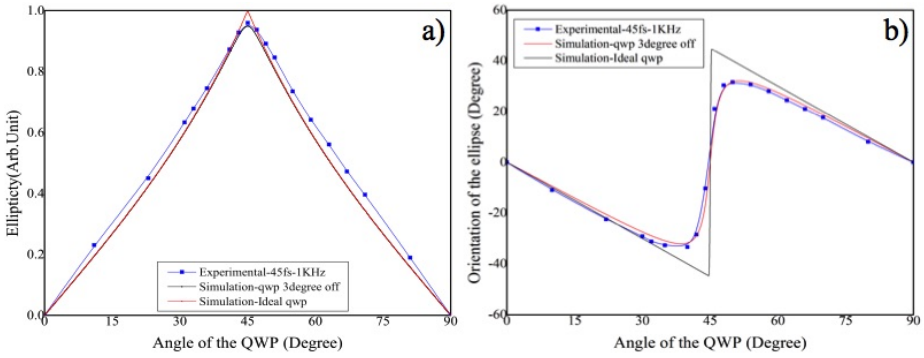

Figure 2.9: Linear response of the polarization measurement system with respect to the QWP angle. a) Ellipticity and b) the angle of the ellipse, with respect to the horizontal axis, for an initially linearly polarized beam are shown for the ideal case of a 90° phase retardation (solid black line).The QWP used in the experiments presented in this thesis, shows a retardation of 87° (experimental blue dotted curves and the red fitted curves)

with δ being the relative phase between E_x and E_y. Once the Jones vector is known, the angle α and the major E_M and minor E_m axis of the electric field ellipse can be recovered. In this study the ellipse is defined in the laboratory frame by its angle α in degrees, and its ellipticity $\epsilon = E_m/E_M$, a number between 0 (i.e. linear, horizontal polarization) and 1 (circular polarization). Figure 2.9 shows the linear response of the measurement system (at a pulse energy of 0.1 mJ at 1 kHz) as a function of the QWP angle. The straight line represents the ideal case of a phase retardation of 90°. The measurement shows that the QWP used here has an actual retardation of 87°. These measurements are used as a calibration (linear response) throughout the thesis.

Chapter 3

Nonlinear index measurement by polarization rotation

3.1 Origin of nonlinear index of refraction

Interaction of an intense elliptically polarized light with an isotropic medium creates different indices of refraction for left and right circular components leading to nonlinear ellipse rotation. In an isotropic medium, the third order nonlinear susceptibility tensor consists of two terms [18]

$$P^{NL} = 6\epsilon_0\chi_{1122}(\mathbf{E}\cdot\mathbf{E}^*)\mathbf{E} + \mathbf{3}\boldsymbol{\epsilon_0\chi_{1221}}(\mathbf{E}\cdot\mathbf{E})\mathbf{E}^* \tag{3.1}$$

Using the same notations as Maker and Terhune [117]

$$A = 6\chi_{1122} \quad (\text{or} \quad A = 3\chi_{1122} + 3\chi_{1212}) \tag{3.2}$$

and

$$B = 6\chi_{1221} \tag{3.3}$$

The nonlinear polarization Eq. 3.1 can be written as

$$P^{NL} = \epsilon_0 A(\mathbf{E}\cdot\mathbf{E}^*)\mathbf{E} + \mathbf{1/2}\epsilon_\mathbf{0}\mathbf{B}(\mathbf{E}\cdot\mathbf{E})\mathbf{E}^* \tag{3.4}$$

The first term in this equation produces a nonlinear polarization with the same handedness as **E** while the second term has the opposite handedness. The ratio of coefficients A and B depends on the the origin of the optical nonlinearity, for example [18]:

$$B/A = 6 \qquad \text{for molecular orientation} \tag{3.5}$$

$$B/A = 1 \qquad \text{for pure nonresonant electronic response} \tag{3.6}$$

$$B/A = 0 \qquad \text{for electrostriction} \tag{3.7}$$

The ratio can be intermediate between these values when different contributions compete, such as appear to be the case in fused silica where reference [118] finds the value $B/A = 0.3$.

3.1.1 Molecular orientation

The tendency of molecules to align with the electric field of an applied optical field is the origin of this nonlinearity, which depends strongly on the material. Molecular alignment changes the average polarizability per molecule and causes the optical wave to experience a different value of index of refraction [18].

$$n^2 = 1 + \chi = 1 + N\langle\alpha\rangle \tag{3.8}$$

with N being the number density of molecules and $\langle\alpha\rangle$ the expectation value of the molecular polarizability, experienced by the aligning electric field.

$$\langle\alpha\rangle = \alpha_\parallel\langle\cos^2\theta\rangle + \alpha_\perp\langle\sin^2\theta\rangle = \alpha_\perp + \Delta\alpha\langle\cos^2\theta\rangle \tag{3.9}$$

Where $\Delta\alpha = \alpha_{\parallel} - \alpha_{\perp}$ is the anisotropy in polarizability of the molecules. In the case of a weak optical field (no molecular alignment), the average polarizability is [18]

$$\langle\alpha\rangle_0 = \frac{1}{3}\alpha_{\parallel} + \frac{2}{3}\alpha_{\perp} = \alpha_{\parallel} - \frac{2}{3}\Delta\alpha \tag{3.10}$$

leading to the linear index of refraction given by

$$n_0^2 = 1 + N(\alpha_{\parallel} - \frac{2}{3}\Delta\alpha) \tag{3.11}$$

The polarizability in the direction of the symmetry axis of the molecule, $\alpha_{\parallel}$, defines the refractive index for the molecules with low $\Delta\alpha$. In the case of intense optical field we have [18]

$$n^2 = 1 + N[\alpha_{\perp} + \Delta\alpha\langle\cos^2\theta\rangle] \tag{3.12}$$

$$n^2 - n_0^2 = N\Delta\alpha(\langle\cos^2\theta\rangle - 1/3) \tag{3.13}$$

Since $n^2 - n_0^2$ is usually much smaller than n_0^2,

$$n^2 - n_0^2 \simeq 2n_0(n - n_0) \tag{3.14}$$

and the molecular alignment induced refractive index change can be shown as

$$\Delta n \equiv n - n_0 = \frac{N}{2n_0}\Delta\alpha(\langle\cos^2\theta\rangle - 1/3) \tag{3.15}$$

3.1.2 Electronic response

The electronic response resulting from the displacement of bound electrons has usually the largest contribution (typically $\chi^{(3)} \sim 10^{-22}\mathrm{m}^2/\mathrm{V}^2$ [18]). Using

the classical, anharmonic oscillator model applied to the case of the nonlinear refractive index [18]

$$\chi^{(3)}_{ijkl}(\omega = \omega + \omega - \omega) = \frac{Nbe^4[\delta_{ij}\delta_{kl} + \delta_{ik}\delta_{jl} + \delta_{iljk}]}{3\epsilon_0 m^3 D(\omega)^3 D(-\omega)} \tag{3.16}$$

with b being a phenomenological nonlinear constant with a value of the order of ω_0^2/d^2, d is a typical atomic dimension, e and m charge and mass of an electron, respectively. $D(\omega) = \omega_0^2 - \omega^2 - 2i\omega\gamma$ (2γ is the FWHM of the atomic linear absorption profile [Hz] and ω_0 the frequency for atomic resonance), leading to (Eq. 3.1 and 3.3)

$$A = B = \frac{2Nbe^4}{\epsilon_0 m^3 D(\omega)^3 D(-\omega)} \tag{3.17}$$

For the case of far-off-resonant excitation $D(\omega)$ can be replaced by ω_0^2 and we find [18]

$$\chi^{(3)} \simeq \frac{Ne^4}{\epsilon_0 m^3 \omega_0^6 d^2} \tag{3.18}$$

For the typical values $e = 1.6\times10^{-19}$C, $m = 9.1\times10^{-31}$kg, $N = 4\times10^{22}$ cm^{-3}, $d = 3\times10^{-10}$m and $\omega_0 = 7\times10^{15}$rad/s we have $\chi^{(3)} \simeq 3\times10^{-22}$m^2/V^2 [18].

3.1.3 Electrostriction

"Electrostriction is the tendency of materials to become compressed in the presence of an intense laser field" [18]. If a change of susceptibility is represented by $\Delta\chi$, we have [18]

$$\Delta\chi = \frac{1}{2}\epsilon_0 C\gamma_e^2 \langle \tilde{\mathbf{E}} \cdot \tilde{\mathbf{E}} \rangle = \epsilon_0 C_T \gamma_e^2 \mathbf{E} \cdot \mathbf{E}^* \tag{3.19}$$

where γ_e is the electrostrictive constant and C_T the compressibility. Nonlinear polarization is

$$\mathbf{P} = \mathbf{\Delta}\chi\mathbf{E} = \epsilon_\mathbf{0}\mathbf{C_T}\gamma_\mathbf{e}^\mathbf{2} \mid \mathbf{E} \mid^\mathbf{2} \mathbf{E} \tag{3.20}$$

Identifying the third order of susceptibility with

$$\mathbf{P} = \mathbf{3}\epsilon_\mathbf{0}\chi^{(\mathbf{3})}(\omega = \omega + \omega - \omega) \mid \mathbf{E} \mid^\mathbf{2} \mathbf{E} \tag{3.21}$$

gives

$$\chi^{(3)}(\omega = \omega + \omega - \omega) = \frac{1}{3}\epsilon_0 C_T \gamma_e^2 \tag{3.22}$$

Comparing Eq. 3.20 to Eq. 3.4 for nonlinear polarization, gives us $A = C_T\gamma_e^2$ and $B = 0$. In order to estimate $\chi^{(3)}$, we have [18]

$$\gamma_e \equiv \rho(\delta\epsilon/\delta\rho) = (n^2 - 1)(n^2 + 2)/3 \tag{3.23}$$

where ρ is the density of the material. γ_e is of the order of unity for condensed matter. $C_T = \rho^{-1}(\partial\rho/\partial p)$ with p being electrostrictive pressure is approximately equal to $10^{-9}\mathrm{m^2N^{-1}}$, which gives $\chi^{(3)} = 3 \times 10^{-21}\mathrm{m^2V^{-2}}$ for condensed matter. For ideal gas $C_T = 1/p$ and $\gamma_e = n^2 - 1$ which lead to $\chi^{(3)}$ of the order of $1 \times 10^{-23}\mathrm{m^2V^{-2}}$ in atmospheric pressure [18]. The nonlinear index of refraction can be expressed as [18]

$$n_2 = \frac{3}{4n_0^2\epsilon_0 c}\chi^{(3)} \tag{3.24}$$

or

$$n_2(m^2/W) = \frac{283}{n_0^2}\chi^{(3)}(m^2/V^2) \tag{3.25}$$

All the physical processes explained above are listed in Table 3.1, with typical values of n_2, $\chi^{(3)}$ and the characteristic time scale for the nonlinear response to develop.

Mechanism	n_2 (m^2/W)	$\chi^{(3)}_{1111}$ (m^2/V^2)	Response Time (s)
Electronic polarization	10^{-20}	10^{-22}	10^{-15}
Molecular orientation	10^{-18}	10^{-20}	10^{-12}
Electrostriction	10^{-18}	10^{-20}	10^{-9}

Table 3.1: Values of nonlinear refractive index induced by different processes and their response time [18].

3.2 Propagation of a polarized light through isotropic nonlinear media

The nonlinear propagation of light through a material is highly dependent on the orientation of its polarization with respect to the material's axes (such as in the case of birefringence). Nevertheless, even in isotropic media (e.g. gases), nonlinearities can be different for each orientation of the electric field. This section presents a review on the nonlinear propagation of polarized light, introducing a method to extract information about the propagation medium trough polarization measurement. Electric field can be presented in left and right hand circular basis as:

$$E_{\pm} = (E_x \pm iE_y)/\sqrt{2} \tag{3.26}$$

Rewriting Eq. 3.4 in circular basis we get,

$$P_{\pm} = \epsilon_0 A \mid E_{\pm} \mid^2 E_{\pm} + \epsilon_0 (A + B) \mid E_{\mp} \mid^2 E_{\pm} \tag{3.27}$$

using the wave equation for plane wave propagation leads to [18],

$$n\pm \simeq n_0 + \frac{1}{2n_0}[A \mid E_\pm \mid^2 + (A+B) \mid E_\mp \mid^2] \tag{3.28}$$

and

$$\Delta n \equiv n_+ - n_- = \frac{B}{2n_0}(\mid E_- \mid^2 - \mid E_+ \mid^2) \tag{3.29}$$

This means left and right circular components of the beam experience different indices of refraction, propagating with different phase velocities. Consequently if an elliptically polarized beam propagates through a nonlinear medium, the polarization ellipse will rotate. In the case of linearly polarized light, we have $\mid E_- \mid^2 = \mid E_+ \mid^2$, which leads to $n_+ - n_- = 0$ and consequently no rotation in the polarization [18]. For the total field amplitude of the linearly polarized light we have $\mid E \mid^2 = 2 \mid E_+ \mid^2 = 2 \mid E_- \mid^2$, from Eq. 3.28 ($n_{linear} = n_0 + \delta n_{linear}$), we get

$$\delta n_{linear} = \frac{1}{2n_0}(A + \frac{1}{2}B) \mid E \mid^2 \tag{3.30}$$

For the circularly polarized light, only one of the components of the electric field is present and from Eq. 3.28 change in refractive index is given by [18]

$$\delta n_{circular} = \frac{1}{2n_0} A \mid E \mid^2 \tag{3.31}$$

Since both A and B are usually positive, circularly polarized light experiences a smaller nonlinear change compare to linearly polarized light. Coefficient B can be found out by measuring the ratio of index change for circular and linear polarizations, leading to the origin of the nonlinearity in the media of interest.

With $\hat{\sigma}\pm$ being circular polarization wave vectors:

$$\hat{\sigma}\pm = \frac{\hat{x} \pm i\hat{y}}{\sqrt{2}} \tag{3.32}$$

field amplitude can be shown as [18]

$$\begin{aligned} & E(z) \\ & \quad = E_+\hat{\sigma}_+ + E_-\hat{\sigma}_- \\ & \quad = A_+e^{in_+\omega z/c}\hat{\sigma}_+ + A_-e^{in_-\omega z/c}\hat{\sigma}_- \\ & \quad = (A_+e^{i(1/2)\Delta n\omega z/c}\hat{\sigma}_+ + A_-e^{-i(1/2)\Delta n\omega z/c}\hat{\sigma}_-)e^{i(1/2)(n_++n_-)\omega z/c} \end{aligned} \tag{3.33}$$

Introducing $k_m = 1/2(n_+ + n_-)\omega/c$ and the rotation angle of

$$\theta = \frac{1}{2}\Delta n\frac{\omega}{c}z \tag{3.34}$$

Eq. 3.33 becomes

$$E(z) = (A_+e^{i\theta}\hat{\sigma}_+ + A_-e^{-i\theta}\hat{\sigma}_-)e^{ik_mz} \tag{3.35}$$

This equation describes a rotated polarization ellipse (see Fig. 3.1). The circular components could be related to the optical field and the degree of polarization, $\epsilon = \tan\phi$, ϕ being the angle between the fast axis of the wave-plate and input linear polarized beam ($\phi = 0°$ for linear polarization and $\phi = 45°$ for circular polarization) as [119]

$$\mid E\pm \mid^2 = \frac{(1 \pm \epsilon)^2}{2(1+\epsilon^2)} \mid E \mid^2 \tag{3.36}$$

Substituting Eq. 3.29, 3.36 and $\mid E \mid^2 = I/(2n_0\epsilon_0c)$ in Eq. 3.34, we have:

$$\theta = -\frac{\omega}{c}[\frac{\epsilon}{1+\epsilon^2}][\frac{B}{4n_0^2\epsilon_0c}]Iz \tag{3.37}$$

For a linearly polarized light with frequency of ω, interacting with a sample of thickness L, phase change for non resonant electronic process ($A = B$) is:

$$\Delta\phi = k\Delta nL = \frac{\omega}{c}[\frac{3B}{8n_0^2\epsilon_0c}]LI = \frac{\omega}{c}n_2LI \tag{3.38}$$

Using Eq. 3.38 in 3.37 we could present (for non resonant electronic process):

$$\theta = \frac{\omega}{c}[\frac{\epsilon}{1+\epsilon^2}][\frac{n_2}{3}]IL \tag{3.39}$$

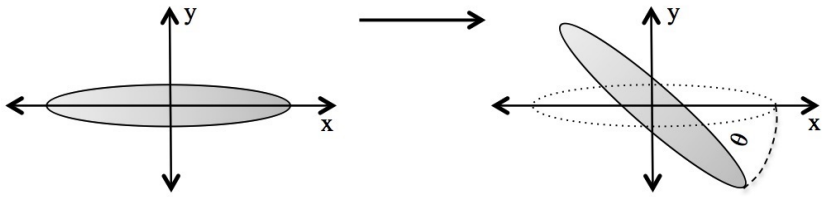

Figure 3.1: Initial and rotated polarization ellipse .

3.2.1 Intensity at focus

In this section an example to measure n_2, using rotation of the ellipse, is provided. First step would be to estimate the intensity (spot size) at the focus point in the nonlinear medium.

Spot size at focus in Air

We start with a Gaussian beam with radius w, at the input of a focusing lens (focal length of f). The wavefront radius of curvature, when modified by the lens, will be $R(z)$ (Eq. 3.40) with the lens located at $-d$ from the beam waist (at $z = 0$) (Fig. 3.2).

$$R(z) = z[1 + (\frac{z_R}{z})^2] \tag{3.40}$$

Where z_R is the Rayleigh range. In a tight focus regime and $\lambda = 800$ nm (laser wavelength used in this work), $R(-f) \approx -f$. Using this approximation along with

$$\frac{1}{q(z)} = \frac{1}{R(z)} - \frac{i\lambda}{\pi w(z)^2} = \frac{1}{R(z)} - \frac{i}{\rho} \tag{3.41}$$

for the beam parameters at the lens we have:

$$\frac{1}{q_{in}} = -\frac{1}{f} - \frac{i}{\rho} \tag{3.42}$$

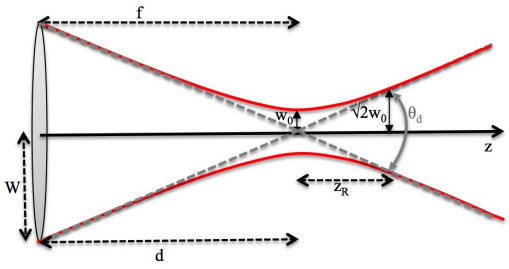

Figure 3.2: Schematic of a Gaussian beam focused by a lens in air to calculate the beam waist and intensity at the focal point of the lens.

Using the ABCD matrix method after the propagation length d, we get:

$$\frac{1}{q_{outair}} = \frac{\frac{1}{q_{in}}}{1 + \frac{d}{q_{in}}} \tag{3.43}$$

Substituting Eq. 3.42 in 3.43 with the minimum beam waist at distance d ($R(d) = \infty$ and $w(d) = w_0$):

$$\begin{aligned} \frac{1}{q_{0air}} &= -\frac{i\lambda}{\pi w_0^2} \\ &= -\frac{(\frac{1}{f} + \frac{i}{\rho})((1-\frac{d}{f}) - \frac{id}{\rho})}{(1-d(\frac{1}{f} + \frac{i}{\rho}))((1-\frac{d}{f}) - \frac{id}{\rho})} \\ &= -\frac{(\frac{1}{f} - d(\frac{1}{f^2} + \frac{1}{\rho^2})) + \frac{i}{\rho}}{(1-\frac{d}{f})^2 + (\frac{d}{\rho})^2} \\ &= \frac{1}{R_1} - \frac{i}{\rho_1} \end{aligned} \tag{3.44}$$

In order to satisfy the equality and find d, the real part of Eq. 3.44 should be equal to zero:

$$\frac{d}{f} = \frac{1}{1 + \frac{f^2}{\rho^2}} \tag{3.45}$$

Using this condition for d and putting the imaginary part of Eq. 3.44 equal to $\frac{\lambda}{\pi w_{0air}^2}$, the beam size at the focus of the lens of focal length f, can be found in air. For this case, the following approximation can be used:

$$\theta_d = \frac{2w_0}{z_R} = \frac{2\lambda}{\pi w_0} \tag{3.46}$$

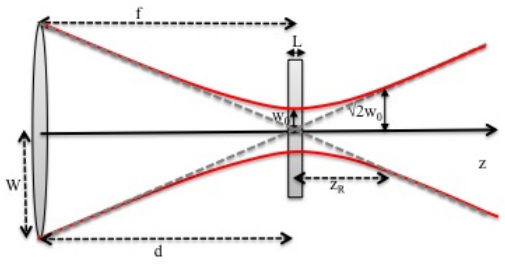

Figure 3.3: Schematic of a Gaussian beam focused by a lens in a piece of glass with thickness of L .

where θ_d is the full angle beam divergence, also

$$\theta_d \approx \frac{2w}{f} \tag{3.47}$$

which gives us

$$w_{0air} = \frac{f\lambda}{\pi w} \tag{3.48}$$

Spot size at focus in nonlinear material

For a more general case, we consider focusing the Gaussian beam in a nonlinear material with index of refraction n. Distance from the lens to the sample is d ($d \approx f - n \times L/2$) and L is the thickness of the sample (Fig. 3.3). In the tight focus regime with $\lambda = 800$nm pulses, $(1 - \frac{d}{f}) >> \frac{d}{\rho}$, so from Eq. 3.44 for the beam parameters entering the sample we have:

$$\frac{1}{q_{inglass}} = -\frac{1}{f(1-\frac{d}{f})} - \frac{i}{\rho(1-\frac{d}{f})^2} \tag{3.49}$$

ABCD matrix from entering the sample to the focus point, is

$$\begin{pmatrix} 1 & \frac{L}{2n} \\ 0 & \frac{1}{n} \end{pmatrix}$$

Consequently for $q_{outglass}$ which is the point with the minimum beam waist in glass, we have

$$\frac{1}{q_{outglass}} = \frac{\frac{1}{nq_{inglass}}}{1 + \frac{L}{2nq_{inglass}}} \tag{3.50}$$

Using Eq. 3.44 and 3.50 for the beam parameters at the focus we get:

$$\begin{aligned} \frac{1}{q_{outglass}} &= \frac{-i}{Z_R} \\ &= \frac{1}{n} \frac{(\frac{1}{R_1} - \frac{i}{\rho_1})(1 + \frac{L}{2nR_1} + i\frac{L}{2n\rho_1})}{(1 + \frac{L}{2nR_1} - i\frac{L}{2n\rho_1})(1 + \frac{L}{2nR_1} + i\frac{L}{2n\rho_1})} \\ &= \frac{1}{n} \frac{(\frac{1}{R_1} + \frac{L}{2nR_1^2} + \frac{L}{2n\rho_1^2}) - \frac{i}{\rho_1}}{(1 + \frac{L}{2nR_1})^2 + \frac{L^2}{4n^2\rho_1^2}} \end{aligned} \tag{3.51}$$

To find the position of the focus (minimum beam waist) in the sample, the real part of Eq. 3.51 should be equal to zero:

$$(\frac{1}{R_1} + \frac{L}{2nR_1^2} + \frac{L}{2n\rho_1^2}) = 0 \tag{3.52}$$

which leads to

$$\frac{L}{2n} = \frac{-\frac{1}{R_1}}{\frac{1}{R_1^2} + \frac{1}{\rho_1^2}} \tag{3.53}$$

Using this condition and putting the imaginary part of Eq. 3.51 equal to $\frac{1}{Z_R}$ lead to the minimum beam waist in the material with index of refraction n and thickness L.

$$\frac{1}{Z_R} = \frac{\lambda}{n\pi w_{0glass}^2} = \frac{\rho}{n} \frac{[\frac{1}{\rho^2} + [\frac{1}{f} - d(\frac{1}{\rho^2} + \frac{1}{f^2})]^2]}{(1 - \frac{d}{f})^2 + (\frac{d}{f})^2} \tag{3.54}$$

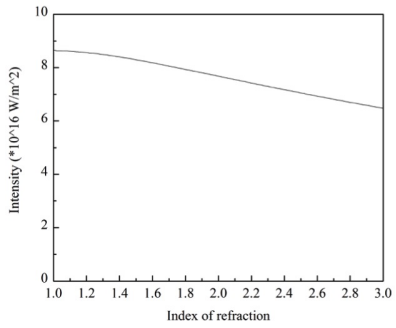

Figure 3.4: Peak intensity for a 100nj, 800nm, 100fs laser beam at focus in a material with index of refraction n using a 5cm focal length lens. Calculated beam waist at focus is $w_0 \approx 2.55\mu m$.

Note that the beam waist at the focus is independent of index of refraction. The intensity however, changes with index of refraction which can be calcu-

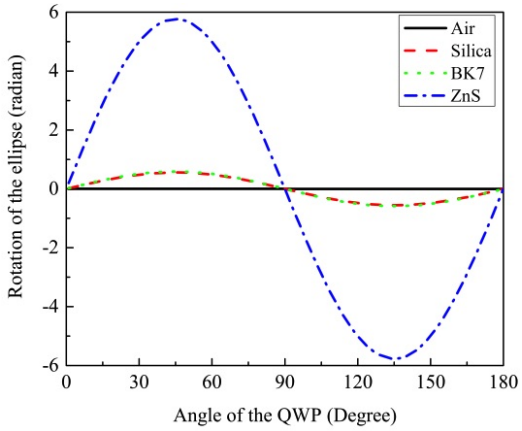

Figure 3.5: Nonlinear ellipse rotation (in radian) versus angle of the QWP that creates the initial elliptical polarization. 800 nm, 1kHz laser pulses with 100nJ input energy and 100fs pulse width are tightly focused in air (black-solid) and 1mm of silica (red-dashed), Bk7 (green-dotted) and ZnS (blue-dash dotted). Nonlinear ellipse rotation is almost the same for BK7 and silica.

Material	n_0	n_2 (m^2/W)	I_{focus} ($\times 10^{16} W/m^2$)	Experimental n_2 (m^2/W)
Air	1.0003 [18]	5.57×10^{-23} [68]	8.63	
Silica	1.47 [18]	3.2×10^{-20} [18]	8.32	2×10^{-20}
BK7	1.52 [18]	3.4×10^{-20} [18]	8.27	
ZnS	2.31 [120]	38×10^{-20} [121]	7.28	30×10^{-20}

Table 3.2: Values for linear and nonlinear index of refraction and intensity at focus in different materials. 100nJ, 800nm, 100fs beams at 1 kHz are focused with a 5cm focal length lens. Conversion from electrostatic unit system is $n_2[m^2/W] = 4.19 \times 10^{-7} n_2$ [esu]$/n_0$.

lated using Fresnel coefficients at normal incidence. Intensity after transmission through glass is lower by a factor of $\frac{4n}{(n+1)^2}$. Figure 3.4, shows the peak intensity of a 800nm beam with 100nJ energy and 100fs pulsewidth, focused in different materials, using a 5cm focal length lens. Using the results from this section for the value of intensity at focus in Eq. 3.39, nonlinear ellipse rotation can be calculated.

Figure 3.5 shows rotation of the polarization ellipse due to interaction of tightly focused 1kHz, 800nm laser pulses with 100nJ input energy and 100fs pulse width, in air and in 1mm of Silica, BK7 and ZnS. Values for linear and nonlinear index of refraction and intensity are presented in table 3.2. Experimental results from nonlinear ellipse rotation can be used to find the nonlinear index of refraction for a known intensity.

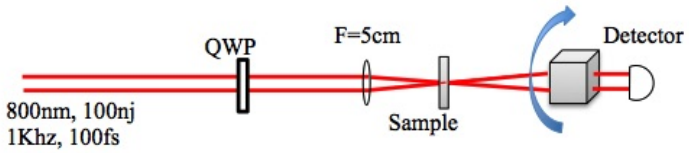

Figure 3.6: Experimental setup to measure the nonlinear ellipse rotation resulting from tight focusing of 800nm, 100nJ, 100fs laser pulses in a sample. Polarization after transmitting the sample, is analyzed with a rotating polarizer cube.

3.3 Experimental details

3.3.1 Nonlinear ellipse rotation for different samples

The experimental setup to measure the nonlinear ellipse rotation is shown in Fig. 3.6. 100nJ, 800nm laser beams are used at 1kHz repetition rate and 100fs pulse width. Initial beam diameter is 5mm and tightly focused in a sample by a 5cm focal length lens. Initial polarization is controlled and changed with a zero order quarter wave plate (QWP). To characterize the measurement system and the QWP, the polarization created with the QWP without the sample was measured (see Fig. 3.7a, blue curve). The measurements were repeated for 1mm thick Silica (Fig. 3.7a, red curve) and Zinc sulfide (ZnS) (Fig. 3.7b, red curve) placed at focus. The expected orientation of the polarization ellipse can be calculated (black curves in Fig. 3.7) from the initial polarization of the beam sent to the samples (blue curves in Fig. 3.7) and the calculated induced nonlinear ellipse rotation (Fig. 3.5). The nonlinear indices of refraction for Silica and Zinc sulfide, using the experimental curve and the calculated intensity at focus (Table 3.2), are $n_2 = 2 \times 10^{-20} m^2/W$ and $n_2 = 30 \times 10^{-20} m^2/W$, respectively (green curves in Fig. 3.7).

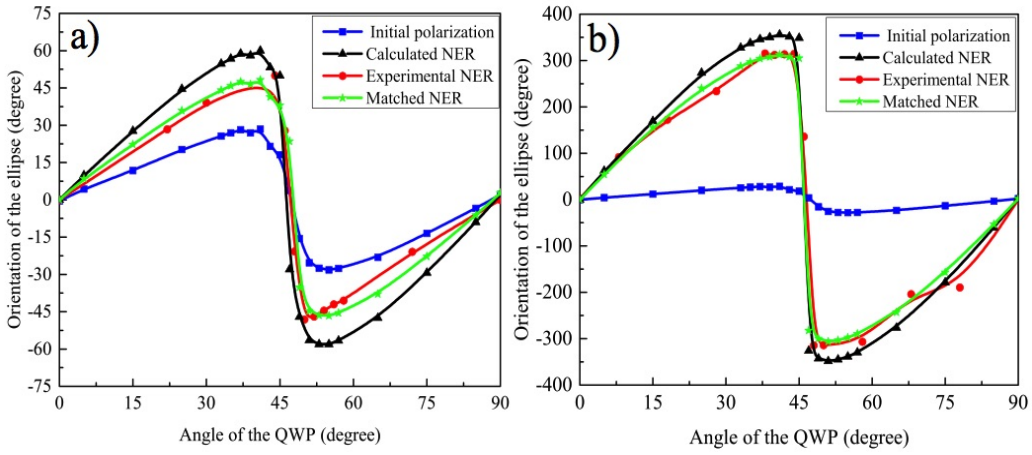

Figure 3.7: Orientation of the ellipse versus QWP angle when 800nm, 100 nJ, 100 fs, 1kHz laser pulses are tightly focused in 1 mm thick a) Silica and b) ZnS. Calculated NER curves are the results of using nonlinear ellipse rotation from last section, for initial polarization (blue curve) focused in the samples. Matched curves (green) show the calculated result with $n_2 = 2 \times 10^{-20} m^2/W$ for Silica and $n_2 = 30 \times 10^{-20} m^2/W$ for ZnS.

3.3.2 Calculating intensity clamping value through NER

As mentioned in the previous section, measuring the nonlinear ellipse rotation provides an accurate way to measure the nonlinear ($n_2 I$) contribution to the index of refraction. Using the experimental results obtained after 60 cm of filament propagation, created with 5mJ, 60fs 800nm beams at 10Hz (see Section 4.2) the value of the intensity in the filament is measured to be 4×10^{14}W/cm^2 (Fig. 3.8).

3.3.3 Conclusion

It was shown in this chapter that the nonlinear ellipse rotation could be used as an accurate way to measure the nonlinear index of refraction in

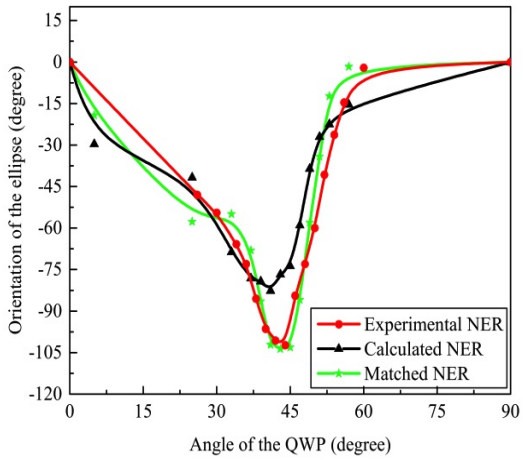

Figure 3.8: Orientation of the ellipse versus QWP angle after 60 cm propagation of a filament created with 800nm, 5mJ, 60fs, 10Hz laser pulses. Calculated NER curve is obtained using the published clamping intensity value [5–7], 5×10^{13}W/cm^2. The matched curve (green) with 4×10^{14}W/cm^2 shows a really good agreement with the experimental data.

different materials. Experimental results and theoretical calculations were presented for different samples. Using this method to measure the intensity in the filament leads to a higher value of 4×10^{14}W/cm^2 than the reported intensity clamping, 5×10^{13}W/cm^2.

Chapter 4

Evolution of filament polarization

Propagation properties of laser filaments are commonly measured trough study of the plasma fluorescence [16] (see Section 5.1), the electron density [122] and the conductivity of electrons [33]. We believe that the study of the filament polarization and how it evolves under different conditions, could be a unique approach to measure nonlinear properties of the propagation medium and the characteristics of the filament itself (see Section 3.2). Recently many studies have addressed the polarization dependence of strong field propagation. The terahertz signal [123], the current in the plasma [124] as well as the ionization yield [125], electron index [126] and molecular alignment [127] are polarization dependent.

In an investigation by Schjødt-Eriksen et al. [128], it was shown that the propagation distance needed for the occurrence of pulse splitting is dependent on the distribution between the two linearly polarized modes and that

higher amplitudes can be reached. This phenomenon was explained by a polarization instability equalizing the energy contained in each circularly polarized component [1]. The linearly and circularly polarized beams were concluded to be unstable and stable respectively.

Following this study, Kolesik et al. [129] did a numerical investigation on the effects of the polarization state on the filament-induced supercontinuum and plasma. It was shown that changing the polarization from linear to circular decreases the plasma generation. The "critical power" for self-focusing is (1.5×) higher for circular than linear polarization, delaying the onset of filament formation for circularly polarized pulses. Nevertheless, plasma dimensions did not depend on the polarization significantly. Starting with an elliptically polarized beam, the polarization state of the beam was changed at the collapse events evolving towards circular polarization. It was also demonstrated that supercontinuum generated by a linearly polarized pulse is much stronger compare to a circularly polarized one [1].

In another study by Fibich and Ilan [130, 131] circularly polarized multiple filaments were investigated. The suppression of multiple filamentation could be seen even for a slightly elliptical polarization (close to circular) within the limits of astigmatism and noise [1].

To address the differences between linear and circular polarized filaments, the first step is to answer the question of the stability of the initial polarization through nonlinear focusing and propagation. In this chapter the stability of the polarization before, at the start point and after the formation of a filament is explored. As mentioned above, THz and supercontinuum generation are polarization dependent. Remote sensing applications based on the fila-

ment remote interactions with the sample (i.e. LIBS or Raman) are highly reliant on this polarization dependency, requiring its complete understanding for quantitative analysis.

4.1 Theory

Following Section 3.2 and Eq. 3.28, nonlinear index change is different for the left and right circular components of the elliptically polarized beam. This birefringence results in the two components of E_+ and E_- to self focus at different rates. For instance a small ellipticity such that $E_- \ll E_+$, according to Eq. 3.28, induces a birefringence of $n_+ \prec n_-$. Since coefficients A and B have positive values, two components are coupled and there will an energy exchange between them. The weaker circular component E_- will feed on the stronger one E_+ (see Section 5.5.6) towards equilibration, creating linear polarization ($E_- = E_+$) [34].

4.2 Measurement results and discussion:

Figure 4.1 shows the polarization measurement setup used in this study. The polarization is measured along the filament, as function of the QWP angle (initial polarization-see Section 2.2.2).

Filaments were created by a commercial Coherent HIDRA laser (see Section 2.1.1) at 10Hz . The waveplate controlling the polarization was followed by a telescope (f_1=-1.2m and f_2=1m) to focus the beam at 3 meters. The

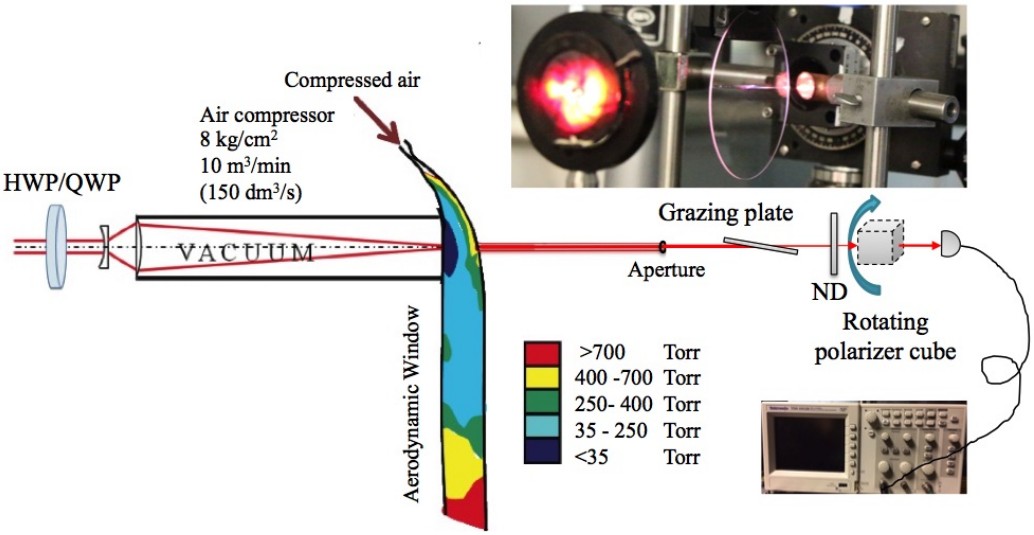

Figure 4.1: The experimental setup to create the laser filaments and polarization measurement (see text for details).

beam is linearly attenuated with a 3" diameter, 1mm thick un-coated fused silica plate near grazing incidence (87° with the normal). In recovering the initial polarization, the effect of the plate and the fact that the transmission is polarization dependent, is taken into account. To ensure only a single filament (the most stable filament in the center) is analyzed, an aperture was placed right before the grazing plate to block most of the energy reservoir. The attenuated transmitted beam is then sent to the rotating polarizer cube. As discussed in Section 3.2, an incoming linear polarization is expected to be maintained along propagation through the nonlinear medium. A HWP was used to create a linearly polarized light at different angles, knowing that the polarization of the beam at the exit of the HIDRA amplifier is also linear. These measurements were done for different conditions (45, 110, 300fs pulses with 9 and 30mJ energy focused in air and vacuum) to confirm that

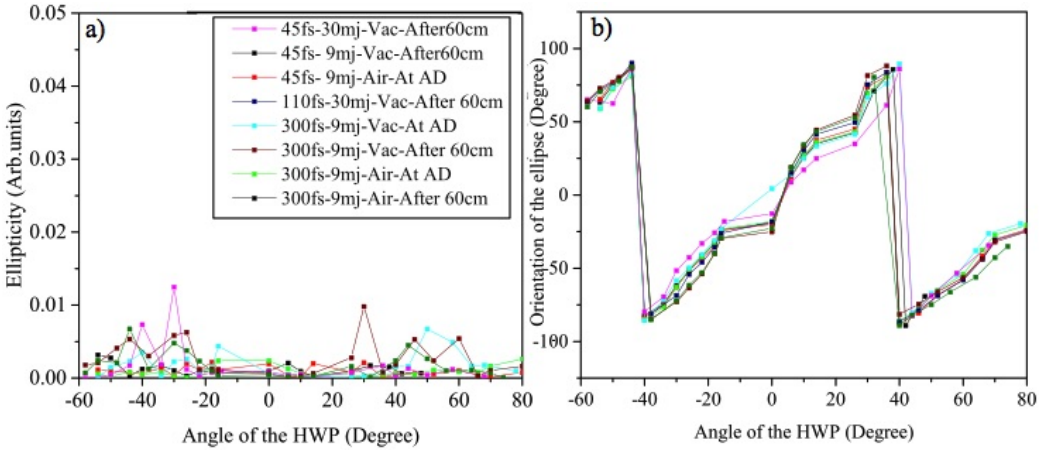

Figure 4.2: a) Measured ellipticity and b) Orientation of the polarization as a function of the HWP angle, 4cm after the focus (At AD) and after 60 cm of filament propagation for 9 and 30 mJ, 45, 110 and 300 fs pulses focused in air and vacuum. 0 for the HWP angle shows the horizontal polarization and ±45 are where the polarization is rotated by 90° (vertical).

the initially linear polarization is unmodified by the filamentation, and there is no nonlinear effect caused by the optics that could modify the prepared polarization. Measurements were performed close to the focus point (At Aerodynamic window (AD)) and after 60 cm of filament propagation. The ellipticity was measured to be less than 0.01 ± 0.01 with an angular resolution of ±1 degree at any waveplate angle (selected cases are shown in Fig. 4.2a). Measurements of the orientation of the polarization also shows a rotation of 90° with the HWP rotating from zero to ±45°, as expected (Fig. 4.2b).

In order to create an elliptical polarization, the HWP was replaced by a QWP (see Section 2.2.2). In order to have a better understanding of how the polarization evolves in each stage of the filament, this study is organized in 3 sets of measurements: "Preparation phase", "Filamentation" and "Post

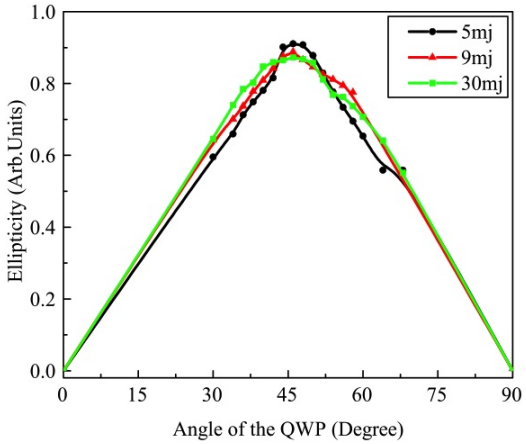

Figure 4.3: Ellipticity measured 4 cm after the focus of the beam in vacuum-air transition, for different energies.

filamentation". "Preparation phase" refers to the first stage of propagation of the light before going through focusing (or self focusing). This stage usually occurs in a nonlinear medium which could potentially change the initial polarization of the light even before the filament starts. The interaction of light with the nonlinear medium could be eliminated by propagating the light in vacuum prior to the focus (see Section 2.1.3). "Filamentation" and "Post filamentation" refer to stages after the focus (starting point of the filament) and after the filament propagation, respectively.

4.2.1 Preparation phase

Light polarization is studied for similar pulse characteristics focused in either air at atmospheric conditions or negligible pressure (1 torr, considered as "vacuum").

Because of the size of the grazing incidence plate (3"), measurements labeled

as "at focus" were in fact done at 4cm after the estimated focal point. There is no change observed in light ellipticity at the focus, with increasing the input energy, for vacuum preparation (Fig. 4.3). This observation shows that 4 cm of nonlinear propagation in air after exiting the vacuum, is not enough to induce any polarization modification.

Figure 4.4a shows the change in ellipticity 4 cm after the focus (beginning of filamentation) for pulses of different initial energies. There is no modification in the ellipticity within 4 cm of the vacuum-air interface (for focusing in vacuum (5mJ case)) compared to the linear case (0.1 mJ- focused in air). In the case of atmospheric focusing, as the input pulse energy is incremented up to 5 mJ, nonlinearities in the preparation phase start to modify the ellipticity *before* reaching the focus (lower ellipticity (≈0.8) for a 45° angle of the QWP). At higher energies this modification is less noticeable due to volume averaging for signal collected at the beam periphery.

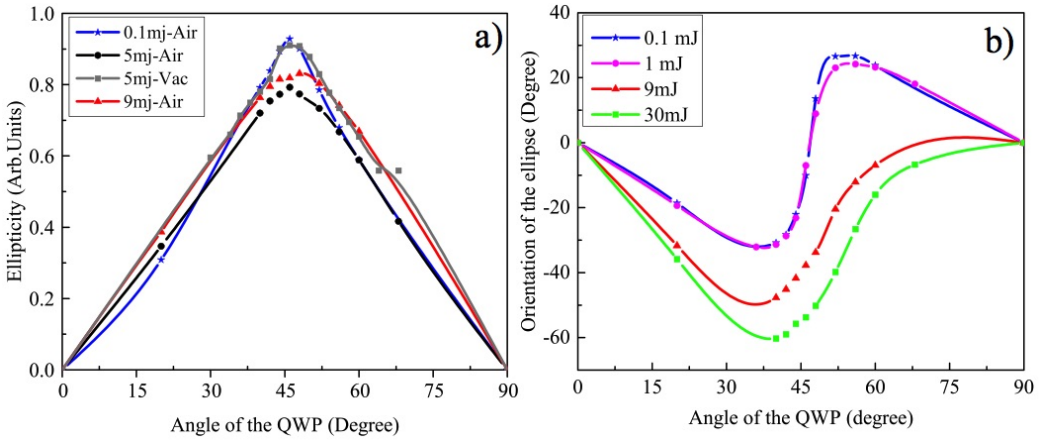

Figure 4.4: a) Light ellipticity measurement at focus for different input pulse energies. b) Orientation of the polarization ellipse at different pulse energies, for different angle of the QWP for a 60fs beam focused in air, measured 4 cm after the geometrical focus [8].

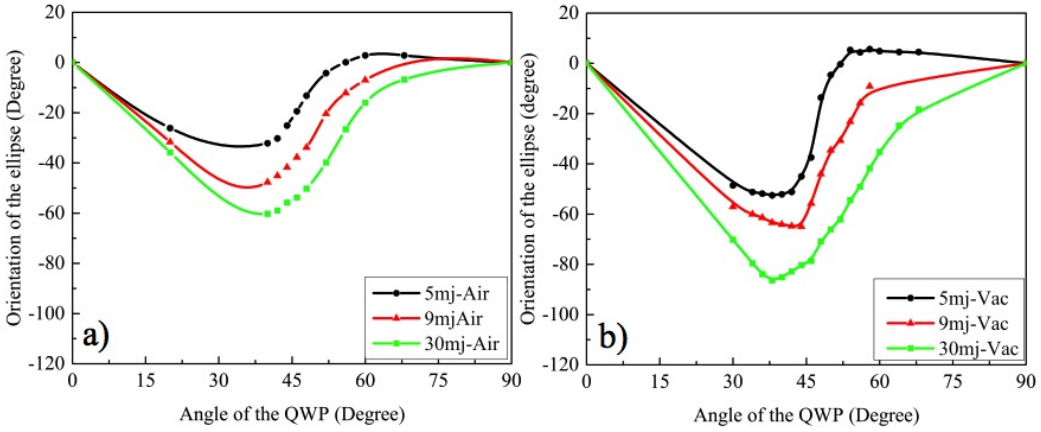

Figure 4.5: Orientation of the ellipse measured 4 cm after the focus, for different QWP angles and different pulse energies of light focused in a) air and b) at the vacuum-air transition [8].

At focus, the angle of the polarization ellipse is also modified with increasing the energy as shown in Fig. 4.4b. Nonlinear contribution to the polarization rotation is confirmed by the visible transition between 1mJ and 9mJ.

Figure 4.5 compares the rotation of the polarization ellipse for filaments at different energies, either prepared in air (Fig. 4.5a) or in vacuum (Fig. 4.5b). At the focus, the increase of rotation with pulse energy suggests that the intensity clamping does not apply prior to filamentation as the intensity increases with energy in both preparation cases.

At a given pulse energy, the polarization rotation is larger for preparation in vacuum, indicating higher intensities at focus, compared to focusing in air. The nonlinear losses for vacuum preparation are negligible while the spot size at the focus is 25% smaller than in air which lead to creating higher intensity when the beam is focused in vacuum [2].

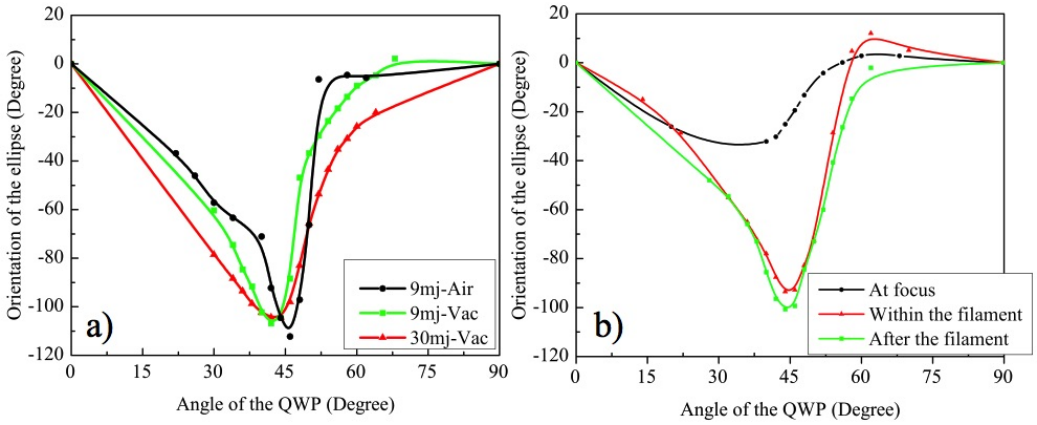

Figure 4.6: Orientation of the polarization ellipse a) measured after 61 cm of filament propagation for a 9 mJ pulse focused in air and vacuum and a 30 mJ beam focused in vacuum, b) for 5mJ light pulses focused in air, measured at different propagation distances [8].

4.2.2 Polarization evolution in filamentation and post filamentation

Figure 4.6 shows the continuation of polarization rotation during the filamentation. A comparison of the ellipse rotation, for a pulse energy of 9 mJ prepared in vacuum and air, is done in Fig. 4.6a. As expected, there is not a drastic difference for preparation in air and vacuum, the clamping intensity being identical. Even though intensity at focus is higher in the case of vacuum focusing very quickly the beam starts to diffract, the intensity drops and reach an equilibration within the filament. The existence of a clamping intensity is further demonstrated by the identical rotation for pulses at 9 mJ and 30 mJ (prepared in vacuum). The angle of the polarization ellipse is no longer modified (for both preparation modes) after the filament (127

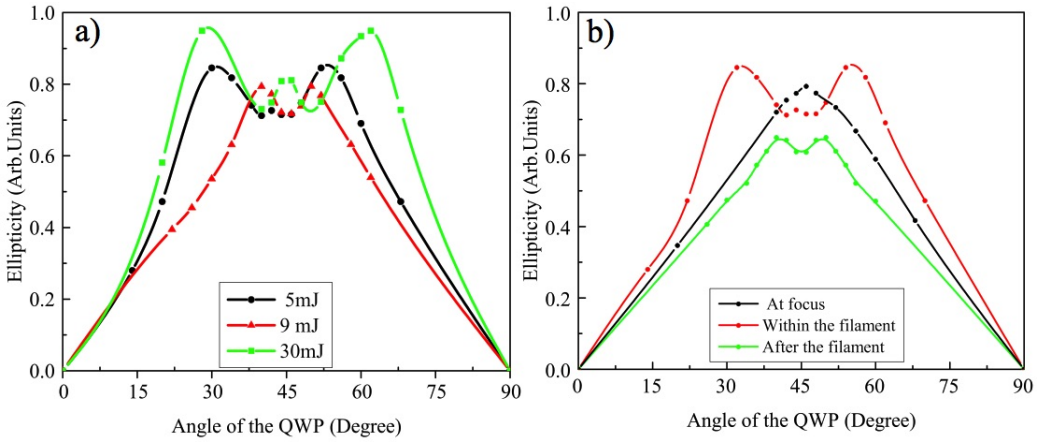

Figure 4.7: a) The effect of the pulse energy on ellipticity for filaments prepared in air. Measurements were done after 61 cm of filament propagation. b) The effect of nonlinear propagation on the filament ellipticity. The initially circularly polarized light becomes more elliptical symmetrically around 45° even after the filament [8].

cm after the focus), because the light intensity has decreased significantly (Fig. 4.6b presents the case of 5mJ pulse prepared in air) and consequently doesn't suffer from further nonlinearities after filamentation. The ellipticity, however, has a different behavior. As seen in Fig. 4.5a the ellipticity is already modified in the preparation phase for the light pulses focused in air. Unlike the polarization angle, the change in ellipticity is dependent on the input energy of the pulse as shown in Fig. 4.7a. While the size and intensity of the single filament remain the same, the ellipticity modifications are increased with the pulse energy in air. We attribute this behavior to the interactions in the beam reservoir. Fig. 4.7b presents the effect of the propagation on the ellipticity of a 5mJ beam focused in air. The modification of ellipticity continues in the filament and even after which is the indication that molecular alignment and conical emission persisting after the filament

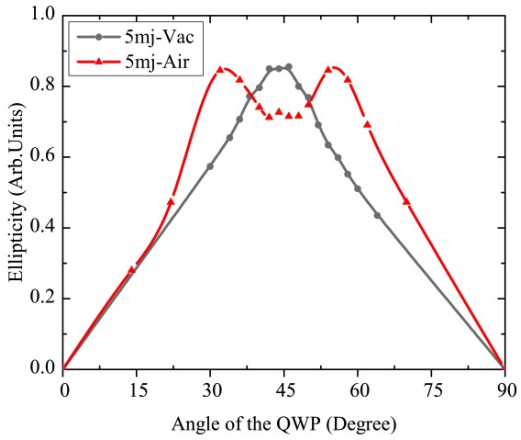

Figure 4.8: Ellipticity measured 127 cm after the focus for air filaments created by focusing a 5mJ beam, in vacuum (gray) and in air (red).

maybe responsible for ellipticity modifications. These results are also confirmed by comparing the change in the ellipticity for a 5mJ beam focused in air and vacuum, measured after the filament (Fig. 4.8). No unusual modification in the ellipticity was observed for filaments prepared under vacuum focusing condition which shows that the nonlinear focusing is necessary, in addition to relating these changes to generation of conical emission (conical emission was barely visible for the filaments prepared in vacuum [2]).

4.3 Effect of the energy "reservoir"

The effect of the energy reservoir surrounding the filament on light polarization is shown in Fig. 4.7a. Since the intensity in the single filament is clamped, increasing the input energy increases the energy in the reservoir enhancing the ellipticity modifications. In order to confirm the contribution of nonlinear processes in the "photon bath" surrounding the filament, on the

polarization change, two approaches were taken. First the polarization was measured after the filament (discussed in the previous Section). The orientation and ellipticity of the polarization ellipse evolve differently after the filament. While Fig. 4.6b suggests that the polarization doesn't rotate more after the filament, the ellipticity still evolves as shown in Fig. 4.7b. Second, the polarization evolution for different parts of the beam (see Section 4.4.1) was analyzed. The ellipticity of the core of the filament was different from the ellipticity of the beam periphery. This is shown in Fig. 4.11a for a 5mJ beam prepared in air and measured at 127 cm after the focus and will be discussed in details in the following section.

4.4 Spatially resolved polarization measurement

As discussed, light polarization propagating in a Kerr medium will be modified through various processes such as non resonant electronic Kerr and molecular Kerr. Like any nonlinear effect, the nonlinear birefringence responsible for polarization will inherit the spatial profile of the propagating beam. In addition, different spectral components of the pulse evolve differently. Results presented in this section show how filament polarization evolves spatially and spectrally. Original spectral components of the beam, components added or removed by changing the chirp (either due to propagation or initial chirp) or new components generated during filamentation have different polarizations after propagation of the filament, than the initial polarization of the beam.

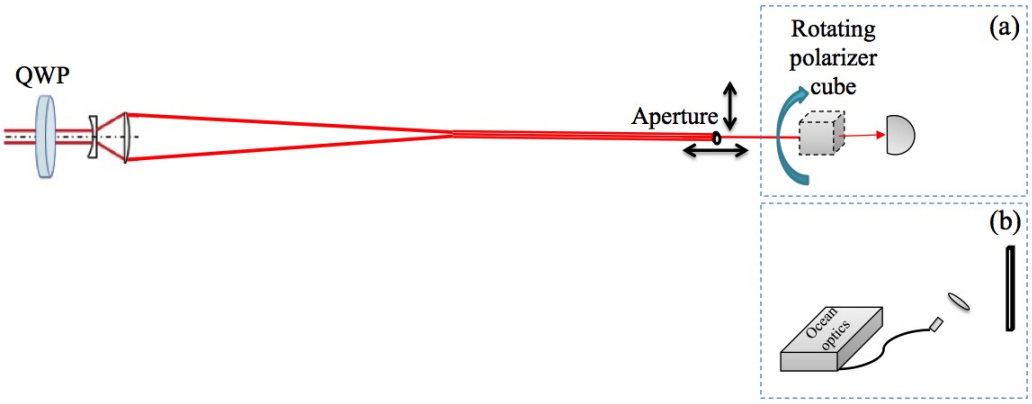

Figure 4.9: Experimental setup to measure a) the polarization change b) spectrum for center and side of the filament created in air.

4.4.1 Experimental setup and results

For the first attempt to study how the polarization changes across the filament, a 100 micron pinhole was scanned across the beam. The filament was created by focusing a 10 Hz, 60 fs, 800nm, 5 mJ beam at 3 meters in air. Similar to the previous setup, the initial polarization was controlled using a zero order QWP (Fig. 4.9a). Polarization was analyzed for the core of the filament and the reservoir (≈1.5mm off axis), at 127cm from the focus. The spectrum of the side and center of the beam, was obtained by collecting the scattered light off a white screen with a lens and focusing it into an Ocean Optics fiber spectrometer (HR2000CG-UV-NIR) (Fig. 4.9b).

Figure 4.10 shows the spectrum change of the center and side of the beam, as a function of the initial polarization. The spectrum of the side is broader and blue shifted compared to the center of the beam. The expected change of the spectrum with polarization, is also more visible (getting narrower around

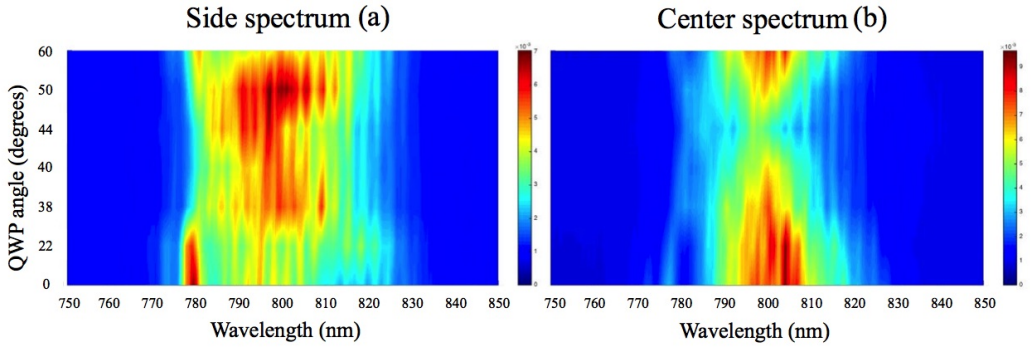

Figure 4.10: Spectrum of the beam a) at the side and b) center. Spectrum of the side is broader and blue shifted with respect to the center of the beam.

circular) in the center of the beam.

Fig. 4.11a shows the ellipticity modification of the beam. The total ellipticity is mostly defined by the energy reservoir since most of the energy is contained in that portion of the beam. The filament core of 200 micron with published peak intensity of 5×10^{13} W/cm^2 holds only 1 mJ (calculated) of the pulse energy. Fig. 4.11b shows more rotation for the side of the beam but the orientation of the ellipse is set by the core since it has higher intensity than the energy reservoir. Beam characteristics of the reservoir define the averaged polarization state. In the weaker portion of the beam, ionization is fairly reduced and other nonlinear and linear processes result in beam reshaping [65, 132, 133]. The large volume around the filament core has sufficient energy to rotate and align molecules leading to the importance of the molecular alignment in the polarization modifications that were shown both in the post-filamentation phase and the energy reservoir.

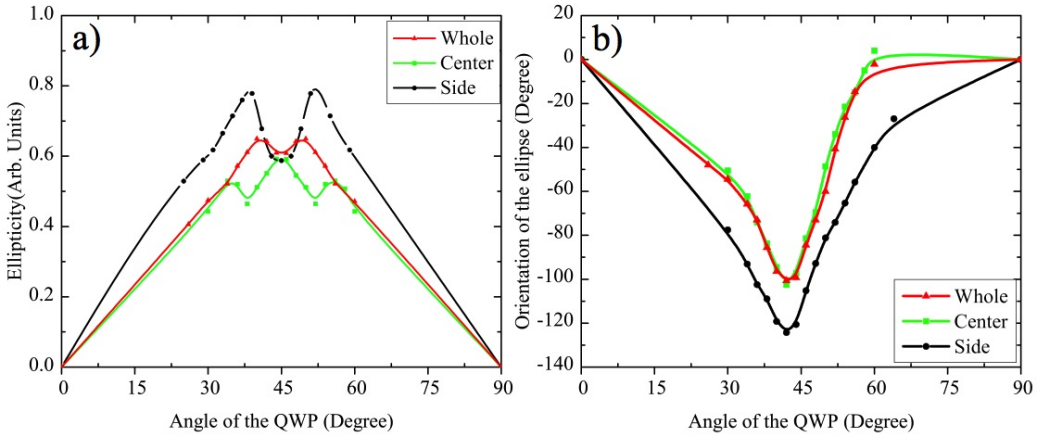

Figure 4.11: a) Ellipticity change [8] b) rotation of the ellipse for a 5mj beam focused in air for the whole (red), center (green) and side (black) of the beam.

4.5 Spectrally resolved polarization measurement

In order to study polarization modifications for different components of the spectrum, 2 prisms and a set of razor blades were used to pick different parts of the spectrum (Fig. 4.12). Selected wavelengths were sent through the rotating polarizer cube followed by a detector (Silicon photodetector 818-SL) to measure the transmission of the cube. An aperture was used before sending the beam through the prisms to be able to resolve the polarization spatially and spectrally at the same time.

Polarization of the light going through the prism set is modified as they are arranged at the minimum deviation angle (which is nearly Brewster's angle), hereby reducing the reflective loss of P-polarized light. The polarization after the filament was analyzed using the same algorithm as in the previous

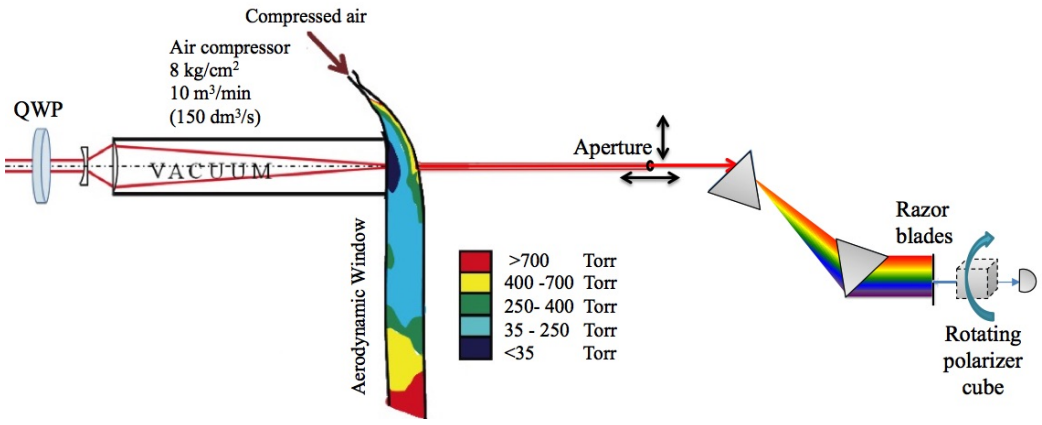

Figure 4.12: Experimental setup of spectrally resolved polarization measurements.

section, taking into account changes that are enforced by the prisms.

The ellipticity change for selected wavelengths for the core of the filament focused in vacuum, is shown in Fig. 4.13a. There is no change in the measured ellipticity in this case, which is in agreement with having no visible blue shifted spectrum in the case of focusing in vacuum (aerodynamic window on) presented by Arissian et al. [134]. Figure 4.13c shows that there is more rotation of the polarization ellipse for shorter wavelength, around circular polarization.

Results for the side of the filament when the beam is focused in vacuum (Fig. 4.13b&d) are in agreement with the core measurements. There is a small change in the ellipticity for the side of the filament, which is in agreement with the results for the 5mJ beam focused in air (Fig. 4.11a), showing ellipticity modifications are more associated with the periphery than the core. The spectral study shows the same behavior for the filaments prepared in either air or vacuum, for both center and the side (Fig. 4.14). The blue shifted light has different ellipticity and rotation than the main beam, showing more

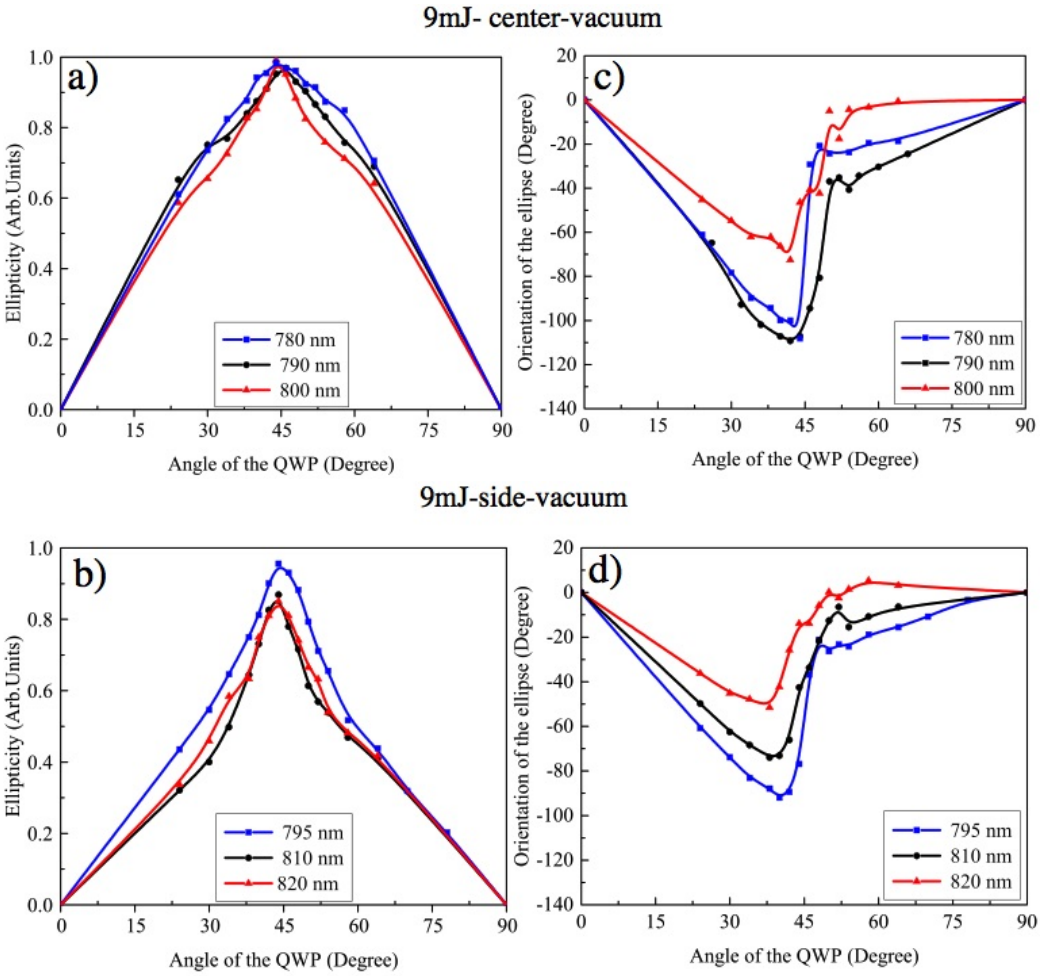

Figure 4.13: a) and b) show ellipticity modifications for the center and side of the beam, respectively. Orientation of the ellipse is presented for c) center and d) side of the filament, created with a 9mJ beam focused in vacuum. Shorter wavelength rotates more than red shifted part of the spectrum.

modification in the ellipticity and rotation in the angle for the shorter wavelengths, around circular polarization. Also comparing the ellipticity changes for the center (Fig. 4.14a) and side (Fig. 4.14b) of the filament, it is clear that the filament reservoir undergoes more changes when it comes to the

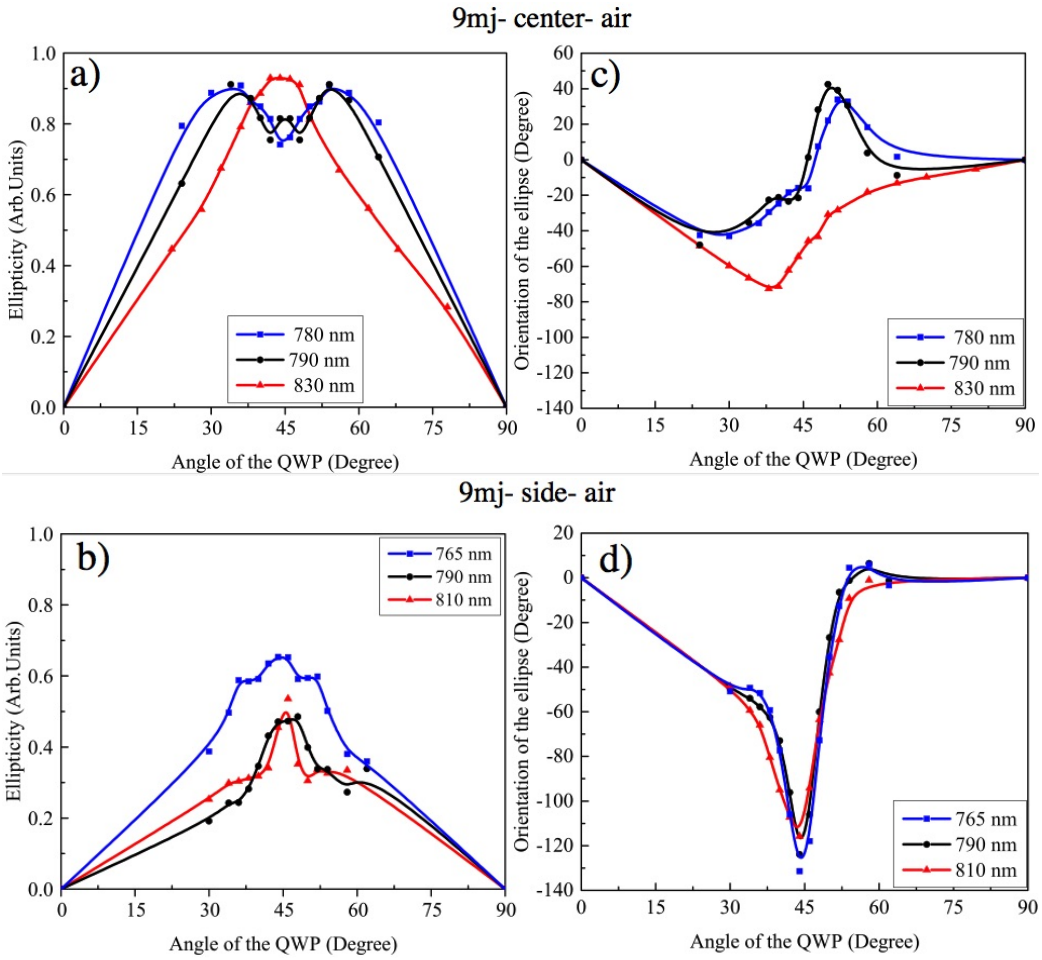

Figure 4.14: a) and b) show ellipticity modifications for the center and side of the beam, respectively. Orientation of the ellipse is presented for c) center and d) side of the filament, created with 9mJ beam focused in air. Blue shifted light has different ellipticity than the rest of the beam and there is more modifications in the periphery than the center of the filament. Shorter wavelength rotates more than red shifted part of the spectrum.

ellipticity.

A second set of experiments that were conducted differently but also confirm the results from the prisms, were done with measuring the spectrum of the

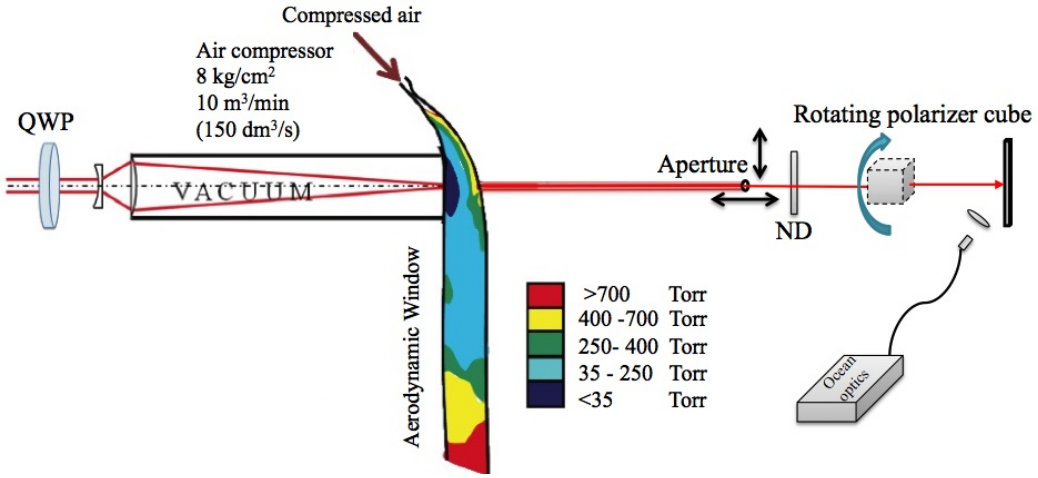

Figure 4.15: Experimental setup of spatially resolved polarization measurements.

light going through the rotating polarizer cube (Fig. 4.15).

The spectrum is divided to different sections (Fig. 4.16) and the polarization is analyzed for each section.

Ellipticity is shown in Fig. 4.17, confirming that the delayed blue shifted

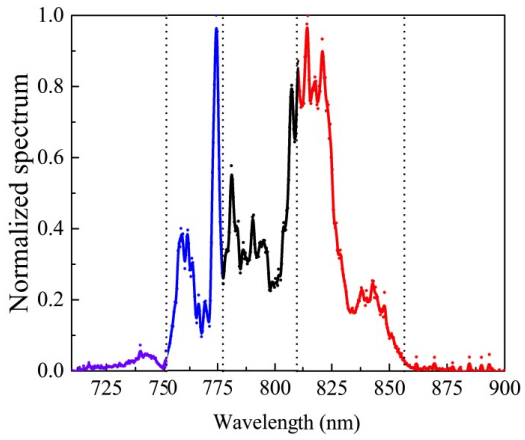

Figure 4.16: Spectrum of the filament reservoir, for 9mJ, 60fs beam, focused in air, divided to different regions to analyze the polarization

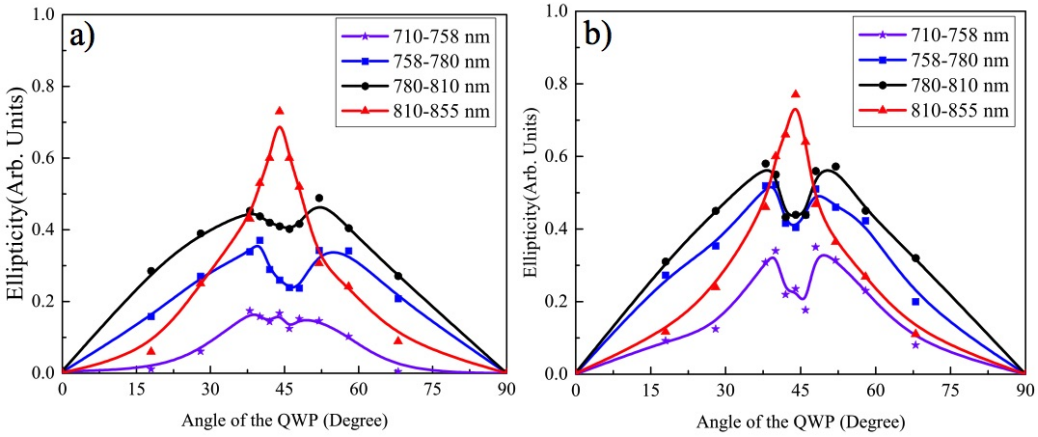

Figure 4.17: Ellipticity measured for the a) center and b) side of the filament, created with 9mj, 60fs pulse focused in air.

light resulting from the chirp, undergoes more change as it sees the tail of the pulse [135].

4.6 Conclusion

The physics of polarization evolution of nonlinear laser propagation, involving electronic Kerr nonlinearity, molecular orientation and electron plasma was studied. A quantitative understanding of the contribution of each element would enable the use of the polarization measurements across the beam profile and along the propagation direction as an accurate diagnostic tool for these nonlinear processes. This study suggests that changes in ellipticity involve energy exchanges related to conical emission and molecular alignment while the polarization angle rotation with propagation, can be a measure of the intensity. This investigation should be extended to more complex polarization conditions such as vortices, radially and azimuthal polarized beams.

Polarization was also analyzed spatially and spectrally for filaments prepared in air and vacuum. It was shown that the polarization change seen after preparation in the nonlinear medium (air) and propagation of the filament, is associated to the periphery of the beam since most of the energy is contained in the reservoir. Ellipticity measurements didn't show any noticeable changes when the beam was focused in vacuum.

Measurements of different spectral regions of the center and side of the beam, showed that blue shifted wavelengths generated during the filament propagation, have different ellipticity than the initial spectral components. Measuring the orientation of the ellipse also confirmed that the blue shifted light goes through more rotation.

Chapter 5

Polarization and dynamics of the filament

5.1 Plasma emission

There have been several studies to measure the characteristics of filament induced plasma such as the electron density. Optical and electrical methods have been used to measure the time dependency of the plasma density [31, 32, 136, 137]. The plasma emission [2, 11], electrical conductivity [2, 138] and acoustic measurements [139, 140] have been used to monitor the longitudinal plasma profile. Plasma emission (fluorescence) is an indicator of the existence, position, length and stability of the femtosecond filament [141]. Properties of the plasma induced by filamentation (lifetime, temperature and diameter) have been studied, using the emission from molecules and ions [1, 93].

Fluorescence from the plasma generated by filaments was first shown for ni-

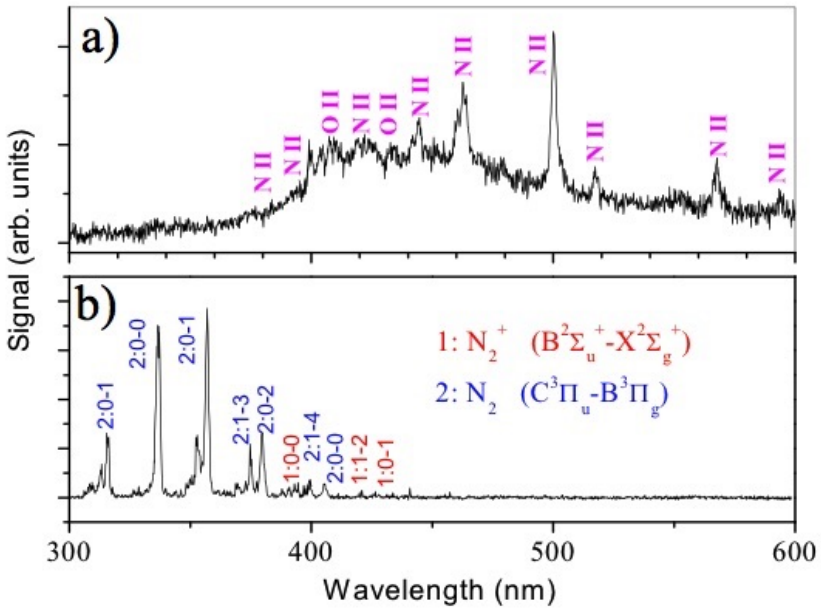

Figure 5.1: a) Long pulse-induced plasma and b) filament-induced fluorescence spectra of air in atmospheric pressure. The short (42fs) and long (200ps) laser pulses with the same energy per pulse (5 mJ), were focused in air using lenses with f = 100 cm and f = 5 cm focal lengths, respectively. (a) Emission lines from singly charged nitrogen and oxygen atoms. (b) Spectral bands resulting from neutral and ionic molecular nitrogen [9].

trogen molecules in air and it was found very "clean" [11], meaning there is no broad component due to a hot plasma or emission from atomic lines. Fig. 5.1 shows the plasma emission induced by 200 ps (a) and 42 fs(b) laser pulses focused in air [9]. In the case of the plasma induced by the femtosecond pulse, energy absorption of the free electrons through inverse Bremsstrahlung is minimized, leading to generation of a clean spectrum in air [142]. Consequently the temperature ($\sim$ 7000K) and the plasma density ($\sim 10^{14} - 10^{16}$ cm^{-3}) [93, 143] are very low in the filament plasma. Figure 5.2a shows the energy-level diagram for nitrogen with the emission spectra in Fig. 5.2b for

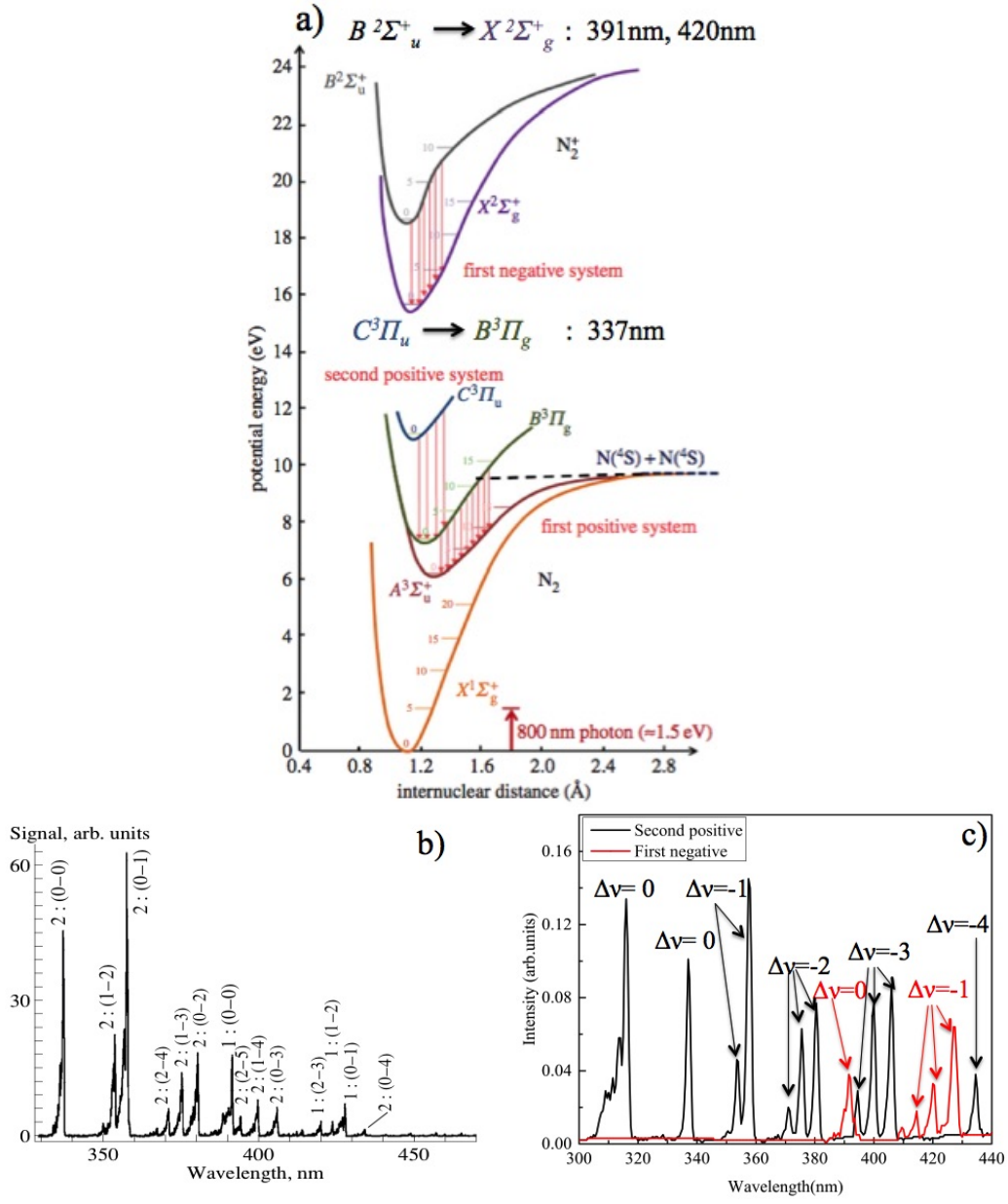

Figure 5.2: a) Energy-level diagram for nitrogen [10]. Emission spectra of air in atmospheric pressure interacting with a Ti:Sapphire laser pulse of duration of b) 200 fs [11] c) our experimental results with 100fs, 30mj pulses.

air in atmospheric pressure interacting with a Ti:Sapphire laser pulse of duration of 200 fs [11]. The lines assigned to the first negative band system of N_2^+ ($B^2\Sigma_u^+ \rightarrow X^2\Sigma_g^+$) and the second positive band system of $N_2(C^3\Pi_u \rightarrow B^3\Pi_g)$ are respectively marked by 1 and 2. In the transitions ($\acute{\nu} - \nu$), $\acute{\nu}$ and ν refer to the vibrational levels of upper and lower electron states, respectively. Experimental results (Section 5.1.2) with 100fs, 30mj pulses are presented in Fig. 5.2c. The intensity of the lines is dependent on the pulse duration.
Having a complete understanding of these emission lines and their dependency on preparation/propagation medium, polarization, chirp, etc., would provide valuable information about filament characteristics. For instance the ratio between the ionic and neutral molecular emission, could be used to evaluate the electronic density or the electric field in the plasma [144].

5.1.1 Dynamic spatial replenishment

The analytical theory of Akhmanov [62] predicted a periodic modulation of the beam diameter and intensity with propagation distance, as the self-focusing and defocusing compete with each other. The same phenomena was predicted by numerical simulation for femtosecond pulses at 800 nm, and called "dynamic replenishment" [59]. Dynamic spatial replenishment was introduced by Mlejnek et al. [59, 67](see Section1.2.3). In this model the beam is considered as a series of thin temporal slices. The dynamic energy exchange between the filament and the energy reservoir is taken into account. The central time slice of the pulse reaches the self-focusing point first due to the highest intensity, ionizing the air and getting defocused into the energy

reservoir by the electrons created in the ionization process. The leading slices with a power above the "critical power" can go through the same process but at longer distances, otherwise they diffract. The plasma created by the leading and central time slices interact with the trailing slices, resulting in their divergence [145, 146]. The focusing-defocusing cycle repeats for the time slices of the pulse that still carry above "*critical*" power. Energy loss from multi photon ionization (MPI) causes the intensity of the leading slices to decay eventually. The energy from the reservoir is fed back to the filament when the trailing slices refocus. The filament evolution presented by this model can be derived using the slowly varying envelop (SVE) approximation in the nonlinear Schrödinger equation (NLSE) (see Section 1.2.5).

Depending on the parameters of the propagation such as, input energy, polarization, chirp, focusing geometry, preparation and propagation media, etc, the fluence distribution can exhibit a regular or irregular resurgence of a fluence peak for each refocusing event. Measurement of the fluorescence in linear polarization was used as an indicator of the intensity fluctuations with propagation of the femtosecond filament [147], an experiment used to justify the plasma model and the dynamic replenishment.

The effects of nonlinear losses prior to filament formation, as well as the pulse characteristics such as input energy, polarization (only parameter that can change electron temperature at a given wavelength and intensity) and chirp on plasma fluorescence at 337 and 420nm are studied in this section. The measurements presented here confirm that filaments prepared in vacuum are consistent with the initial model of self-induced waveguide (Kerr focusing, plasma defocusing), while the properties of most filaments prepared in air

are dominated by the interactions with air prior to the start of a filament.

5.1.2 Experimental details

The experiments were done with a commercial CPA Ti:Sapphire femtosecond laser system (Coherent) at 800nm, 10Hz (see Section 2.1.1). The filament is initiated at 3m of a focusing telescope (f_1=-1.2 m, f_2= +1m) in the case of focalization in vacuum, with the vacuum-air transition located at the focal point. The telescope is adjusted (distance between the negative and positive lenses) to have the geometrical focus at the same location when the beam focused in air. Initial polarization was controlled with a zero order quarter wave plate before the formation of the filament. The induced fluorescence was collected from the side of the filament and then focused into a scanning monochromator (Jobin Yvon SPEX (Model HR-640)). The full spectrum of the filament plasma emission was measured by scanning the grating of the spectrometer.

The $C^3\Pi_u \rightarrow B^3\Pi_g$ (337nm (0-0)) and $B^2\Sigma_u^+ \rightarrow X^2\Sigma_g^+$ (391.1nm (0-0), 414.5nm (2-3), 420nm (1-2) and 427.5nm (0-1)) transitions were studied, focusing on how they change with polarization and preparation medium (Fig. 5.3). These lines are from different transitions and as such, their response to the pulse and medium parameters may differ from one another. It has to be noted that these measurements were done at a fixed position ($\approx$ 5cm from the geometrical focus) and as a consequence, don't reflect the full filament dynamics. But they already provide a preliminary understanding of the effect of polarization on filament formation.

To have a better idea of how these emission lines change the longitudinal

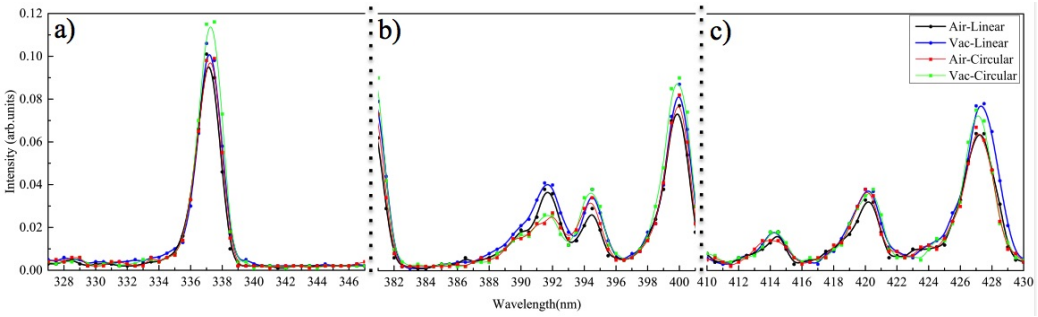

Figure 5.3: Emission of the plasma filament created with a 100fs, 30mJ, 800nm, focused by a 3m lens, measured after 5 cm after the filament starts in air and vacuum, with initial linear and circular polarization at a) 337nm, b) 391nm, 414.5 c) 427.5nm.

spatial distribution of plasma radiation from excited N_2 molecules at 337nm and from excited N_2^+ ions at 414.5nm , 420nm and 427.5nm along the propagation was measured. A 2f imaging configuration was used to collect the N_2 (337nm) and N_2^+(≈420nm) fluorescence from the side (Fig. 5.4). To ensure a good spatial resolution [0.7mm (Fig. 5.4b)] a slit was placed between the 2 fused silica lenses of the same (3.5cm) focal length. Fluorescence intensity was monitored by a photomultiplier tube and narrow band filters at 337 ± 10nm and 420 ± 10nm (Edmund optics band pass filter at 337±10nm and Newport 10BPF10-420).

5.2 Results and discussion

To understand the dynamics of the filament intensity with polarization, the plasma emission is used as a proxy to determine the eventual ionization of the N_2 molecules. As mentioned in the previous section, the detection of the plasma emission is focusing on the bandhead at 337 nm for the neutral N_2

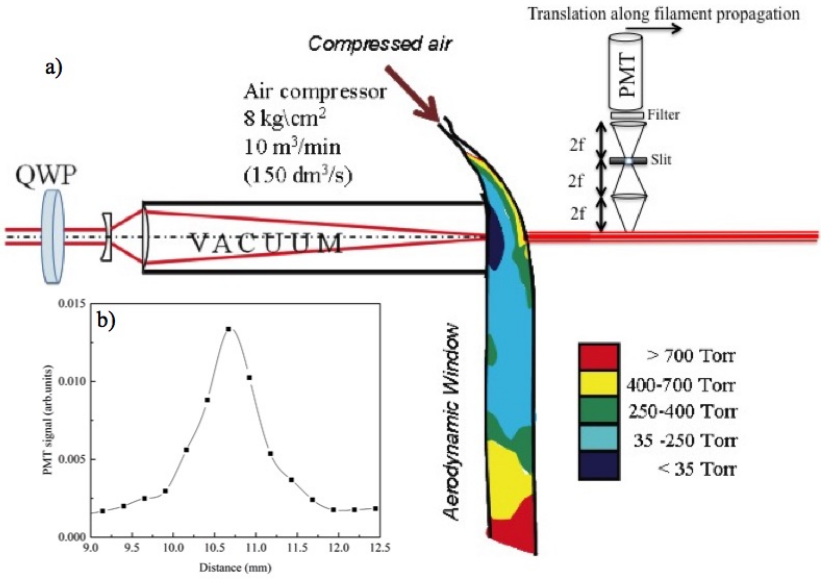

Figure 5.4: a) experimental setup used to measure the emission from the filament prepared in air and vacuum. Zero order QWP was used to control the polarization before the focus. A 2f imaging configuration was used to collect the light from the side to focus on the PMT. b) Spatial resolution of the measurement system. Both imaging lenses, slit and PMT were translated together over a point source.

molecules and the bandhead at 420 nm for the singly-ionized N_2^+ molecules. These results are presented and discussed below.

Nitrogen side emission at 337nm The experiments were performed with the aerodynamic window (see Section 2.1.3), so there is no light matter interaction before the pulse has reached the characteristic size and intensity of a filament. As it enters the atmosphere after the beam waist as a diffracting (diverging) beam, there is no possibility for axicon focusing and the generation of an axicon. Measurements of the beam profile of a filament as a function of propagation distance have shown that the diameter of the filament created in vacuum remains constant ($\approx 200\mu m$) over a longer distance

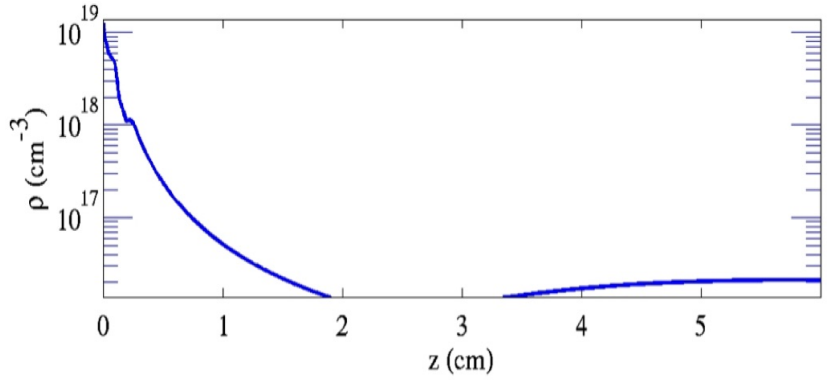

Figure 5.5: Simulated electron density versus propagation distance by A. Couairon.

than the filament created in air [2]. Using the aerodynamic window and eliminating nonlinear losses before the focus, let the beam to reach a smaller size than the usual size of the filament ($\approx 250\mu m$) and consequently higher intensity than the clamping, entering the atmosphere. The propagation of a pulse with such a high intensity was investigated in numerical simulation by Arnaud Couairon (Fig. 5.5). His simulation shows high ionization at the geometrical focus. The spatio-temporal shape of the pulse is very quickly modified, resulting in a rapid decay of the electron density, followed by a resurgence as the pulse takes a quasi steady state shape.

Our experimental results agree with Couairon's simulations (Fig. 5.6). At the first point that the measurement ($z \approx 1.5cm$ after the geometrical focus) could be performed, a high peak in the 337nm emission is observed. This intense radiation from excited nitrogen molecules is followed by a fast decay resulting from photoionization and a second peak (refocusing), depending on the polarization, energy and pulse width. Figure 5.6a shows the same propagation dependence for the plasma radiation at 337 nm in linear (9 mJ)

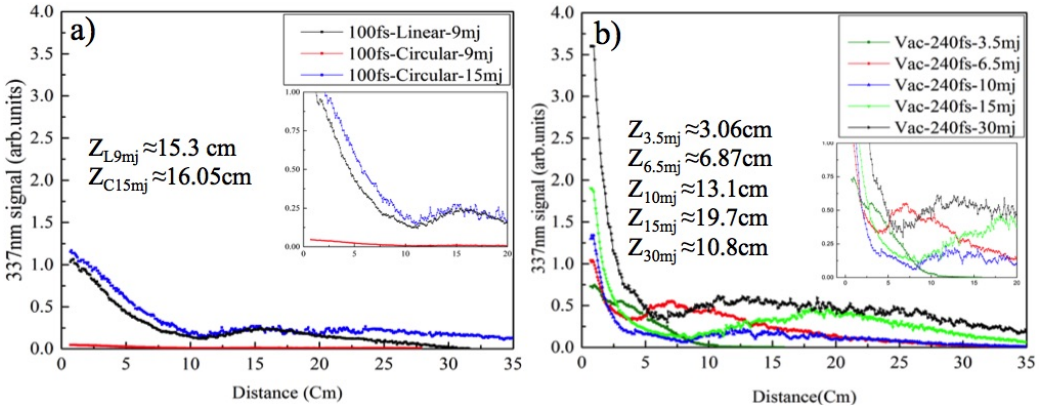

Figure 5.6: 337nm emission from a filament created by focusing a a)100fs and b) 240 fs negatively chirped and linearly polarized beam in transition between vacuum and air for different input energies and polarizations. Zero shows the geometrical focus point and the inserts are focused on the first self-focusing event for each condition.

and circular (15 mJ) polarization, reinforcing that there is no polarization dependency, for equal electric field amplitude. The lower field (9 mJ) circular polarized pulse is seen to be below threshold for filamentation, focusing the beam in the transition between vacuum and air [2] due to lower $\chi^{(3)}$ effects for circular polarization.

To see the effect of pulse duration and chirp, the pulse width was increased to 240fs (measured right after the compressor, before being sent to the QWP) (Fig. 5.4), by increasing the distance between the gratings in the pulse compression system. As the energy of the negatively chirped pulse is increased, the second emission peak moves away from geometrical focus (z=0) and makes the filament longer and more stable (Fig. 5.6b). For 30mJ pulses, re-focusing happens closer to the focus. This observation doesn't agree with what Mlejnek et al, reported in the study of power dependency of the dy-

namic replenishment [67]. They claimed that with increasing the power, the second refocusing event moves closer to the geometrical focus and makes the filament shorter, until the point that there is enough energy to create another re-self focusing.

The simulations of Mlejnek are based on different initial conditions, where different part of the beam are allowed to focus at different distances. In the situation of Fig. 5.6b, as well as in the simulation of Couairon (Fig. 5.5), there is no reservoir, since the initial condition is a Gaussian beam waist. The initial steep decay can be understand as a result from sudden nonlinear high order ionization and defocusing, bringing the intensity down to the range of the clamping intensity. The subsequent defocusing- refocusing for vacuum prepared filaments can be understood as an adiabatic redistribution of intensity, similar to the simulation for the UV filaments [116]. The very high order of ionization and short pulse duration make the situation more complex than in the case of a long pulse and three photon ionization considered in refrence [116]. Figure 5.7 shows the result of 337nm side radiation from the filament with 9mJ (Fig. 5.7a) and 15mJ (Fig. 5.7b), either linear or circularly polarized and focused in air. The onset of the filament is moved well before the geometrical focus due to self focusing in the nonlinear medium (air). Filaments created with linear polarization start before the ones with initial circular polarization as can be seen in the case of 9mJ pulses. This observation can be explained by the lower strength of $\chi^{(3)}$ effects for circular than linear polarization, resulting in a weaker self-focusing and delaying the onset of filamentation [147]. Dynamic replenishment effect in both linear and circular polarizations is clearly seen. Right after the interaction of the pulse

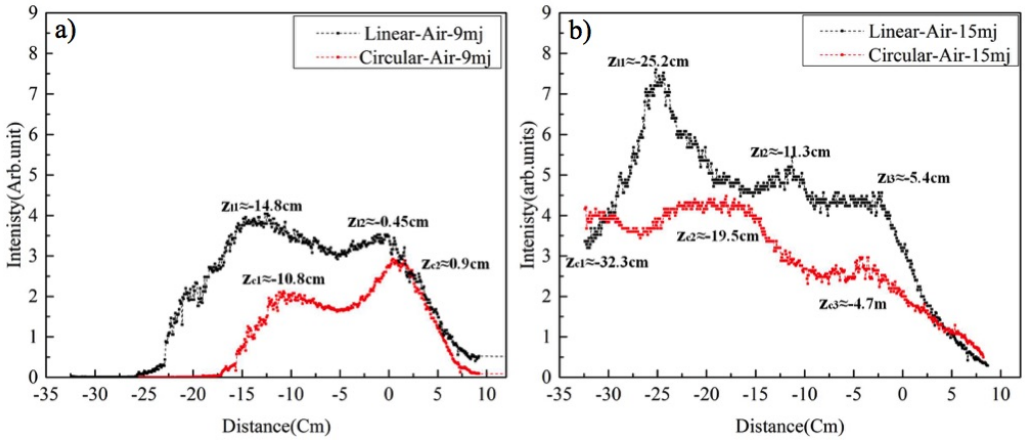

Figure 5.7: a) Side plasma emission at 337nm for a) filament created by focusing a 9mJ beam in air with initial linear (black) and circular (red) polarizations b) filament created by focusing a 15mJ beam in air with initial linear (black) and circular (red) polarizations . Zero shows the geometrical focus

with the nonlinear medium, plasma generated by the wake of the leading edge defocuses the trailing part causing the intensity to drop. Due to the contribution of the negative nonlinear index from the plasma and other high-order nonlinear effects the intensity in the trailing edge becomes much lower than in the leading edge. Then, multi photon absorption causes the power in the leading edge to drop. As the propagation continues, the trailing edge of the pulse experiences positive nonlinearity (nonlinear Kerr index), and the beam in the trailing edge starts to refocus. These de-focusing and re-focusing phenomenon, can be seen at propagation distances $z \approx -5$ cm ("-" refers to positions before the geometrical focus) and $z = 0$ cm (geometrical focus point) in Fig. 5.7a. These processes could be repeated many times as long as the power in the trailing edge of the pulse is larger than the critical power for self focusing. This reoccurrence of the refocusing events could be seen in

Fig. 5.7b , with higher input energies and having a stronger energy reservoir that could feed the filament through providing enough energy to the trailing slices of the pulse to refocus. With higher input energy, a linearly polarized pulse still induces a strong first collapse whereas a circularly polarized pulse induces a more subtle replenishment (Fig. 5.7b). For both energies, in the circular polarized case, the second self focusing happens later and also comparable (stronger in the 9mJ case) with the first one, compared to the linear case. The MPI is more efficient with linear polarization compare to the circular case, creating a larger plasma channel. A larger part of the beam is then defocused by the plasma, making the second self-focusing less visible in the linear polarization case. The plasma channel induced by the circularly polarized filament is smaller, letting a larger off-axis part of the beam to self-focus and create a higher fluorescence signal in the second self-focusing event [147]. These observations also reflect the fact that $\chi^{(3)}$ effects are smaller and MPI is less efficient with circular polarization than linear and the balance between these two manifests through the intensity modulations of the measured fluorescence along propagation. The modulations of the signal with 9mJ beams are 13cm for linear and 12cm apart for the circular case which are in the vicinity of Rayleigh range of the focused beam. As the energy is increased, the distances where the first and second SF events happen, are almost the same. 15mJ provides enough energy to see the third refocusing of the beam happening 7cm and 16cm (close to the geometric focus) after the second peak for linear and circular polarized beams respectively. The end point of the filaments created with different polarizations and also different energies is approximately the same which was also observed by Brodeur et al [56] who

claimed previously that the filament terminates at the diffraction length of the beam (diffraction caused by the focusing lens is stronger than the self focusing effect of the beam).

Comparing the 337nm emission for a filament preparation in air (Fig. 5.7) and vacuum (Fig. 5.6) show that the refocusing events are more pronounced in the former case. When the beam is focused in the transition between vacuum and air, high ionization is observed as soon as the beam exits the vacuum. This high density of the electrons in the plasma lead to a stronger defocusing and depending on how strong the reservoir is (energy of the beam), the filament could recover from that strong defocusing with another refocusing. When the beam is prepared in air, the created electron density which is the source of defocusing, is not as high as the vacuum case. Unfortunately the absolute comparison of the emission intensities for air and vacuum can't be done since the measurements in vacuum weren't possible right at the exit of the window which we believe would give us the highest ionization.

Nitrogen side emission at 420 ± 10 ***nm*** As mentioned previously, since the processes involved in the emission from excited molecules and ions are different the same experiments were performed but with the focus on 420±10nm line which is ($B^2\Sigma_u^+ \rightarrow X^2\Sigma_g^+$) transition. Results presented in (Fig. 5.8) show that there is no clear second peak observed for circular polarization even with 30mJ input energy. As the pulse width is increased, 420nm emission could be observed for longer distances from the geometrical focus, but still without any replenishment (Fig. 5.8b). For the linear case, for both 9 and 30 mJ cases, the negative chirp results in more pronounced re-focusing but the position stay relatively the same. For both 337nm (Fig. 5.6) and

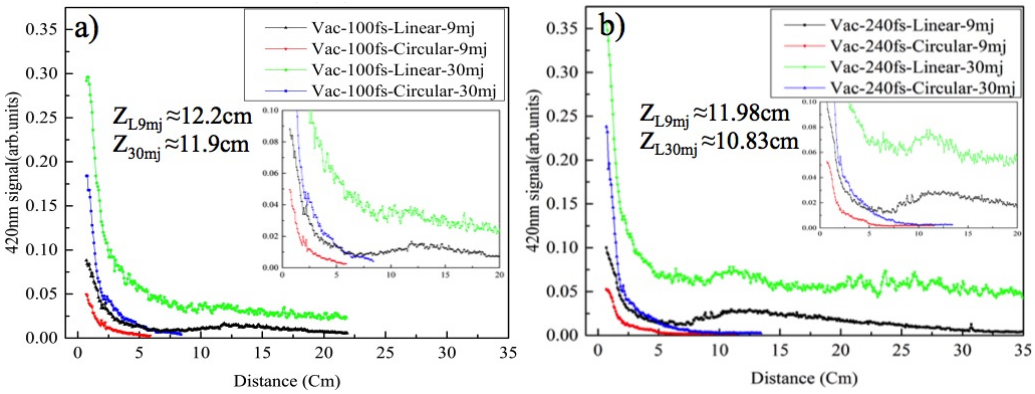

Figure 5.8: 420nm emission from a filament created by focusing a a)100fs and b) 240 fs negatively chirped beam in transition between vacuum and air, for 9 and 30 mJ with linear and circular polarization. Zero shows the geometrical focus point

420nm emissions, the amplitude of the first peak increases with the 240fs negatively chirped pulse. To examine the effect of energy and polarization further, fluorescence at 337 and 420 nm was measured at a fixed position (≈ 3.8 cm after the geometrical focus). Figures 5.9 a&c, show the effect of energy for circular and linear polarization with 100 fs and 240fs negatively chirped pulses. The overall trend is that the 337 and 420nm signals increase as the energy is increased. There is an unexpected increase in the signal around 9mJ for all cases, which is more pronounced for negatively chirped linear polarized light. Repeating the same measurements for the beam focused at the transition between air and vacuum shows an increase in the signal with increasing the input energy (Fig. 5.9b&d).

In an ideal case, the fluorescence signal is expected to decrease when the polarization changes from linear to circular, as seen in Fig. 5.10 b&d. Preparation of the filament in vacuum helps maintaining the initial polarization

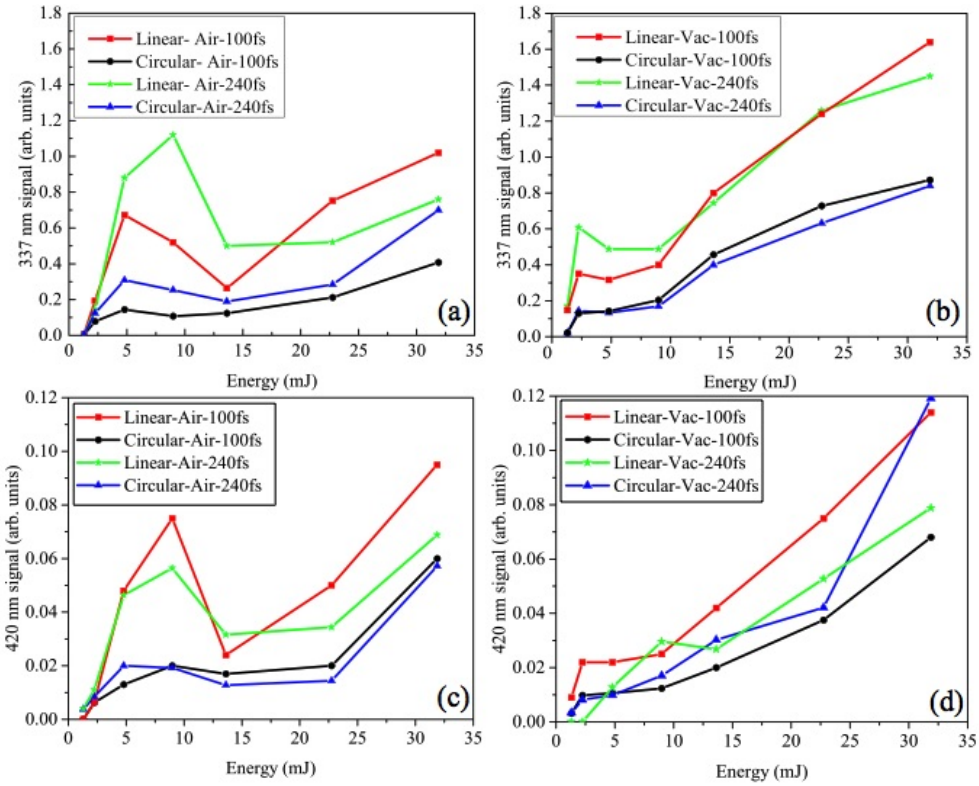

Figure 5.9: 337nm emission from a filament created by focusing 100fs and 240 fs negatively chirped beams with linear and circular polarizations in a) air and b) transition between vacuum and air for different input energies. 420nm emission from a filament created by focusing 100fs and 240fs negatively chirped beams with linear and circular polarizations in a) air and b) transition between vacuum and air for different energies. Zero shows the geometrical focus point

of the beam therefore the emission from the plasma follows the decrease in the intensity from linear through elliptical to circular. As discussed in Chapter 4.2, nonlinear medium (in this case, air) causes the polarization close to circular to change leading to an increase in the fluorescence signal (Fig. 5.10a&c).

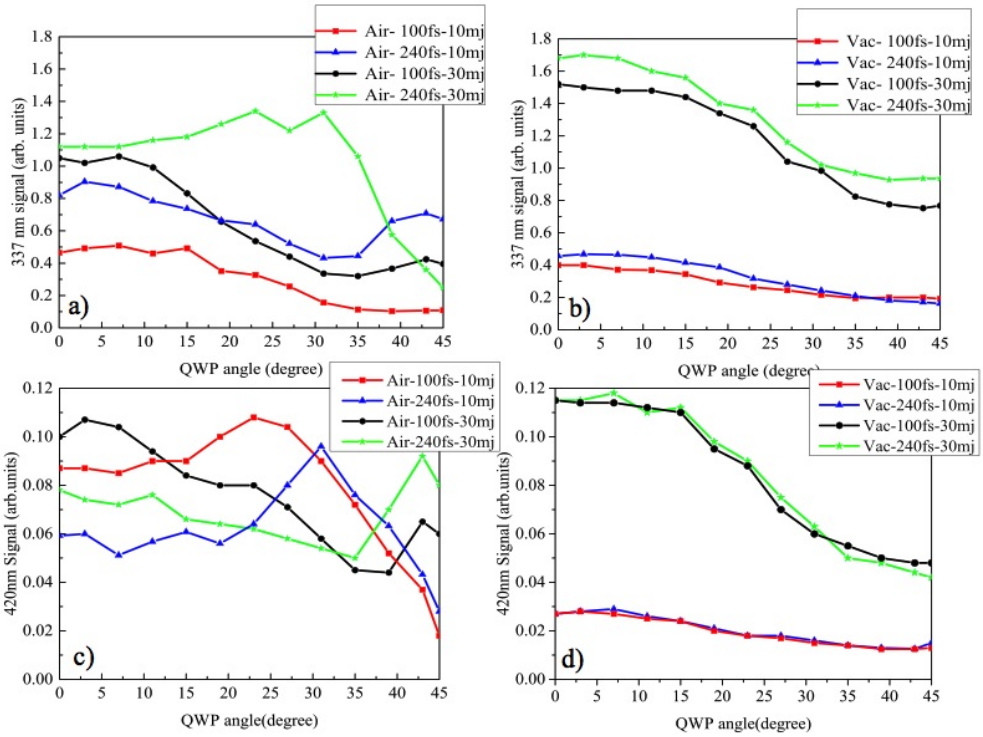

Figure 5.10: 337nm emission from a filament created by focusing 100fs and 240fs negatively chirped beams with 10 and 30 mJ input energies in a) air and b) transition between vacuum and air for different input polarizations. 420nm emission from a filament created by focusing 100fs and 240fs negatively chirped beams with 10 and 30 mJ input energies in a) air and b) transition between vacuum and air for different input polarizations. Zero shows the geometrical focus point

5.3 Supercontinuum generation

Supercontinuum generation (SCG) has been a subject of interest for many research groups. Despite the long history, there remains a need for more complete understanding of the mechanisms underlying filament-induced SCG. One of the important factors that play a significant role in filament induced

SCG is the focusing process before filamentation by propagating and focusing the light in a nonlinear medium. Linearly polarized beam, propagating in an isotropic medium such as air is not expected to be affected (see Section 4). Elliptical polarization on the other hand, is not stable during propagation and could change the dynamics of the interaction between the beam and the propagation medium affecting the polarization dependent properties of the filaments (Section 4.2).

The effects of different polarizations on filamentation have been studied by several groups. While it appears obvious that the weaker ionization efficiency and Kerr effect with circular polarization should lead to lower plasma densities [129] and less efficient supercontinuum generation [148–150], various groups have shown otherwise [147, 151, 152]. Varela et al. [153], showed that independent of the nature of the gas, increasing the ellipticity from linear to circular, induces a decrease in spectral bandwidth and suppression in the appearance of multiple filaments. Sandhu et al [150] explored the ellipticity dependent of supercontinuum generation in molecular medium with longer pulses and observed a dependence on the molecular structure with the same trend of enhanced broadening for linearly polarized light. As discussed in details in Section 4.2, polarization after the filament is created is not stable and could also vary across the beam profile and depends on the medium [8]. In this section the effect of the laser polarization on filamentation and the consequent SCG in different media is investigated in a combined experimental and theoretical study. The experiments in this section were done in collaboration with the Laser and Plasma Laboratory at University of Central Florida, college of optics and photonics [4, 12]. The theoretical simulations

were performed by John Palastro.

5.4 Experimental setup

In the experiments, femtosecond laser pulses (pulse duration τ_p = 50 fs, energy E = 2.8 mJ, wavelength λ= 800 nm) from the Multi-Terawatt Femtosecond Laser (MTFL) facility (see Section 2.1.2) [154] at the University of Central Florida were used to create the filament with a low NA ($\approx 10^{-3}$) focusing arrangement [155], into a transparent gas cell (length L = 4.5 m). The the gas tube was sealed with fused silica windows (800 nm AR coated for entry and uncoated for exit) and the central part was made of transparent PVC allowing the visualization of the plasma emission. The tube was pumped down to vacuum(<0.1 mTorr) and filled with different gases up to ≈1 atm (Fig. 5.11). Elliptically polarized laser pulses, created with a zero order QWP (CVI QWPO-800-10-4) placed just before the focusing lens, were used to produce single filaments (through pressure control) in air, nitrogen (N_2), oxygen (O_2), argon, and krypton. The spectrum of the white light supercontinuum after filamentation was measured after scattering by a diffuser, using spectrometers covering visible (λ= 300-740 nm, Ocean Optics HR2000) and near-infrared (λ= 660-930 nm, Ocean Optics USB2000) regions of the spectrum. Polarization of the beam after filamentation was determined by fitting the polarization ellipse obtained by measuring the transmitted energy (Gentec QE25LP) through a rotating polarizing cube, for each QWP angle. The beam was attenuated before sending to the polarizer cube, using a neutral density filter. For both the spectral and polarization measurements, the

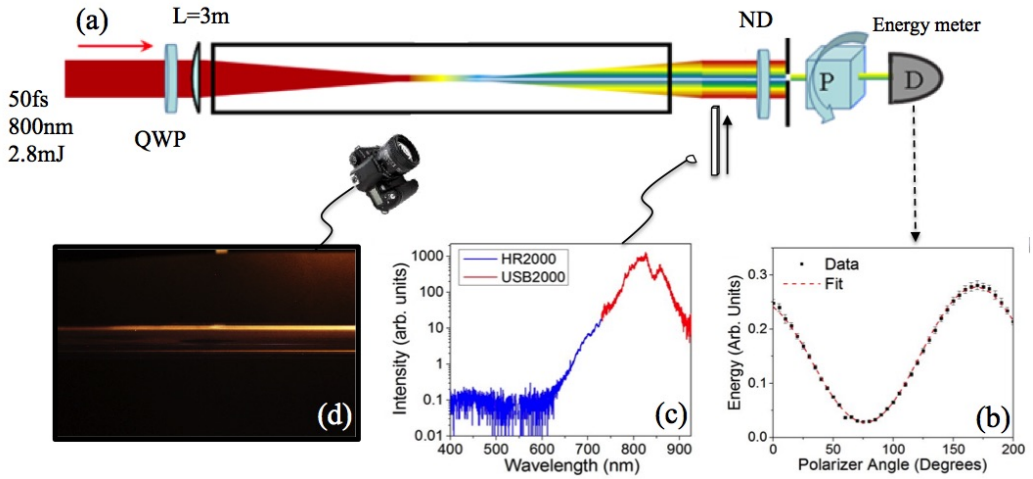

Figure 5.11: a) Experimental setup to measure the supercontinuum spectrum and polarization ellipticity. b) Data taken from the energy meter is fitted and polarization is extracted c) 2 fiber-coupled spectrometers record the scattering from a white screen diffuser covering the spectral range 300-930 nm d) A camera was used to take pictures of the filament and the conical emission created after the tube [4, 12].

detectors were placed approximately 2.2 meters after the geometric focus of the lens. To determine the position and length of the filaments and also to observe how the conical emission is changed with polarization, pictures of the filaments were taken using a DSLR (Canon 5D mk II).

For all gases, the pressure was kept low enough such that a single filament was formed (verified by the supercontinuum pattern) for each polarization. Nonlinear effects in the windows were minimal, if not completely eliminated, by keeping them far away enough from the filament. The conical emission in the spectral measurements was rejected by the acceptance angle of the collection fiber and removed by an iris in the ellipticity measurements.

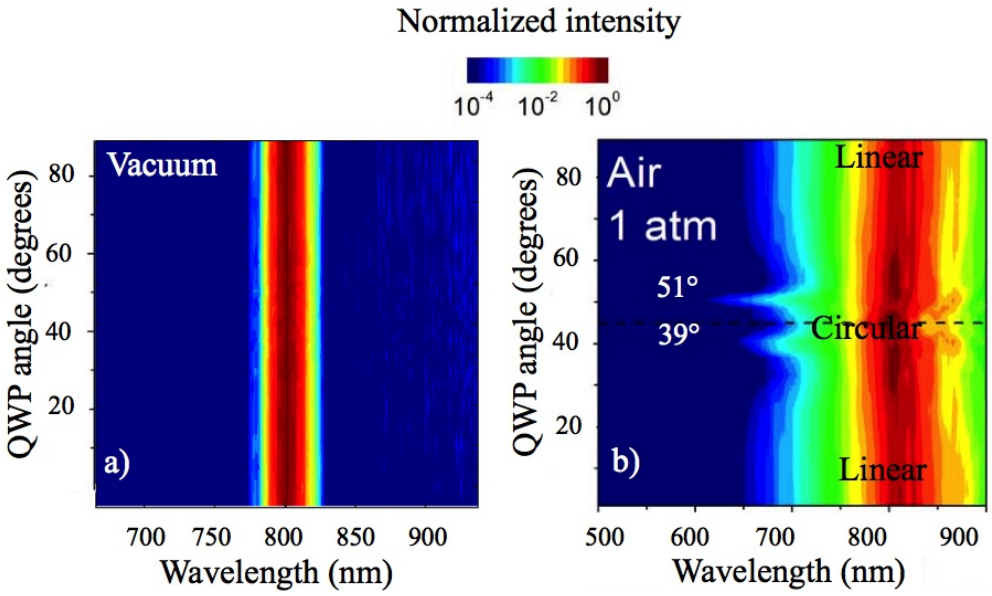

Figure 5.12: Spectral intensity of the supercontinuum spectrum as a function of wavelength and QWP angle (normalized to highest value in 2D map) measured in (a) vacuum [12] and (b) air [4, 12].

5.5 Measurements and results

5.5.1 Spectral measurements

In order to have a reference, the gas tube was pumped down to vacuum and the spectrum of the laser pulse with about 0.47 mJ input energy was recorded. The output spectrum wasn't affected by input polarization changing from linear to circular (Fig. 5.12a). When the tube was filled with air at atmospheric pressure, the supercontinuum bandwidth decreased by increasing the input ellipticity from linear to circular with the exception of QWP angles $\approx 39°$ and $\approx 51°$ where the spectrum broadened, acquiring an orange hue. The enhancement of the spectral broadening was symmetric around circular po-

larization (QWP angle 45°), showing no preference for left or right circular polarization (5.12b). In order to understand the origin of the anomalous

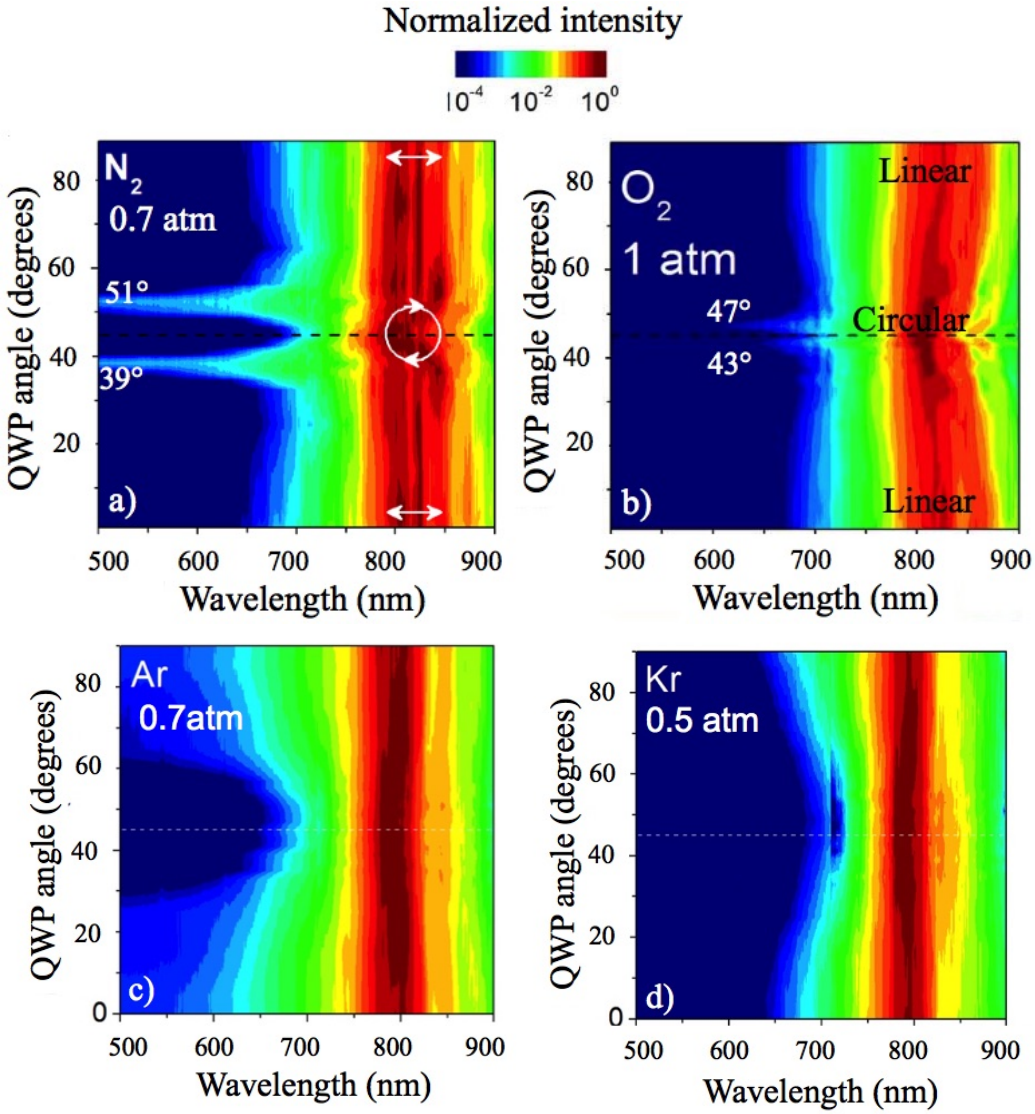

Figure 5.13: Experimental results of ellipticity-dependent supercontinuum spectrum produced from single filaments in (a) nitrogen, (b) oxygen, (c) argon and (d) krypton [4, 12].

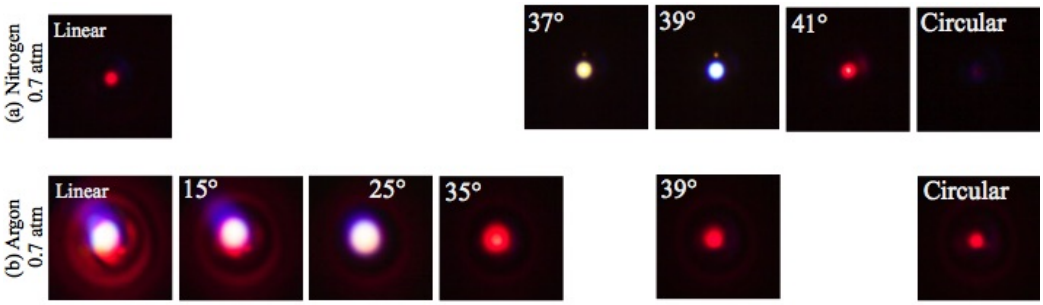

Figure 5.14: Pictures of the beam taken for different initial polarizations after exiting the gas tube filled with a) nitrogen and b) argon, at 0.7 atm [12].

broadening, spectral and ellipticity measurements were performed in different molecular and atomic gases. In nitrogen, more pronounced anomalous broadening of the supercontinuum spectrum was observed (Fig. 5.13a) for the same QWP angles of 39° and 51° (input ellipticity $\varepsilon_{in} \approx 0.7$), observed as a white core in the beam (Fig. 5.14a). This unusual broadening effect was observed in oxygen as well (Fig. 5.13b), but at different initial polarizations (QWP angles 43° and 47°- $\varepsilon_{in} \approx 0.8$) and weaker than in air. Same measurements done in argon which has a comparable ionization potential to nitrogen (15.76 eV and 15.58 eV, respectively), show no anomalous broadening (Fig. 5.13c) and were confirmed with the results from krypton with lower ionization potential (Fig. 5.13d). In atomic gases, the spectrum at linear polarization was significantly broader compare to the molecular gases, and as the polarization was changed to circular, the spectral bandwidth in the visible range reduced gradually and smoothly. This effect was also confirmed with the pictures taken of the beam after exiting the tube (Fig. 5.14b).

5.5.2 Polarization measurements

Polarization measurements of the beam after filamentation showed modifications around circular polarization for molecular gases (Fig. 5.15a&b) and no change for atomic gases (Fig. 5.15c&d). To show the change of polarization with propagation through the nonlinear media, they are compared to the linear case in vacuum (Fig. 5.15, gray). In the case of molecular

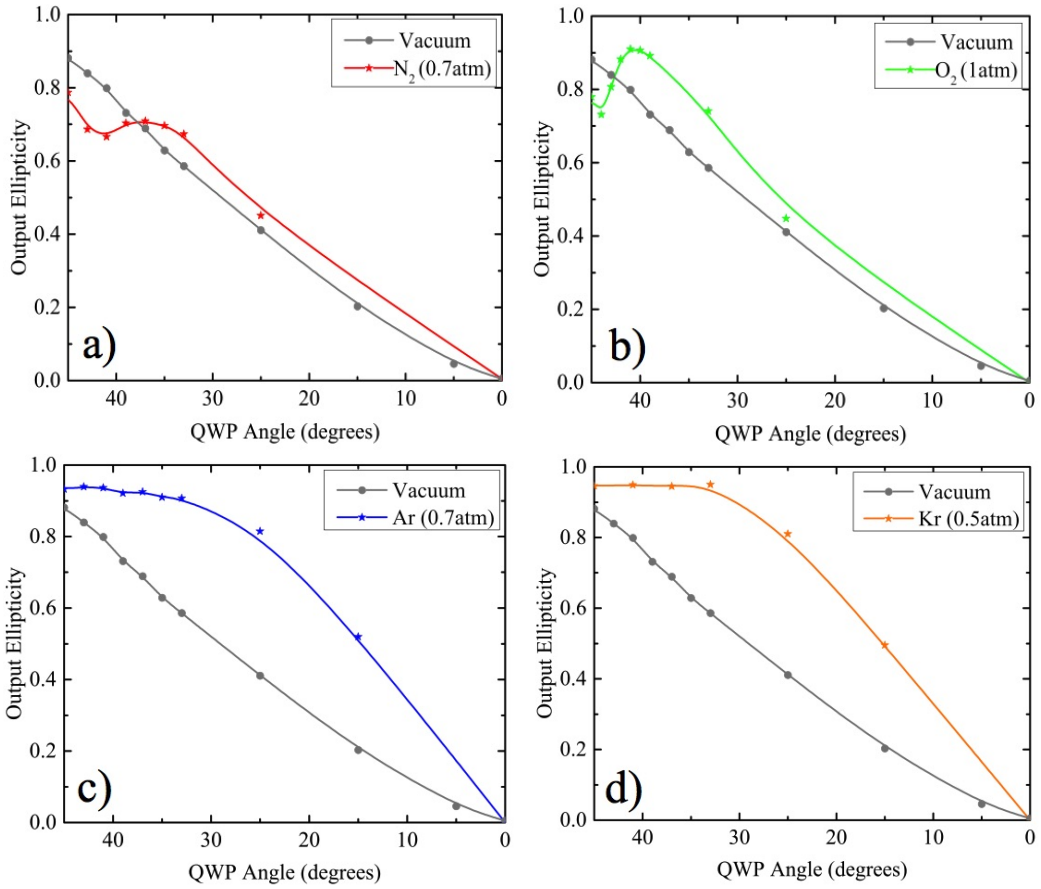

Figure 5.15: Ellipticity measurements of the beam after filamentation in (a) nitrogen, (b) oxygen, (c) argon and (d) krypton compare to vacuum (gray) [4, 12].

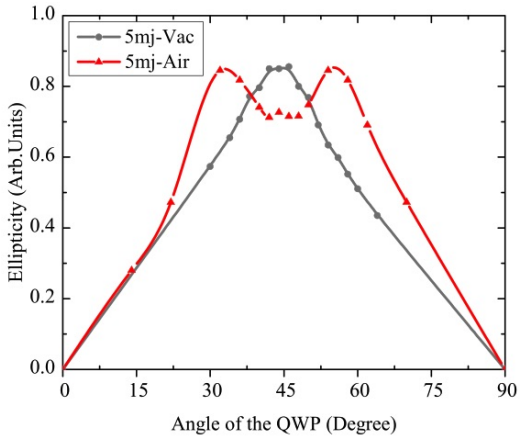

Figure 5.16: Output ellipticity for air filaments prepared by focusing in vacuum (gray/circles) and in air (red/triangles) [4].

gases(Fig. 5.15a&b) there is a decrease in the ellipticity of the beam at the same QWP angles where anomalous spectral broadening was observed. The ellipticity is increased closer to the circular polarization but to a different value comparing to the reference (vacuum case). In atomic gases (Fig. 5.15c&d) when the polarization was changed from linear to circular, the ellipticity increased more rapidly and reached a plateau around QWP $\approx 30°$. As it was discussed in Section 4.2, elliptically polarized pulses show anomalous behavior in the polarization of the beam after filamentation in air. Under comparable conditions to the experiments presented in this section, substantial modification of polarization was observed at similar input ellipticity close to circular polarization. However no unusual behavior was observed for filaments prepared under vacuum focusing conditions (Fig. 5.16) which shows that the nonlinear focusing (involving the Kerr response of the molecular medium) is necessary for the observation of anomalous behavior

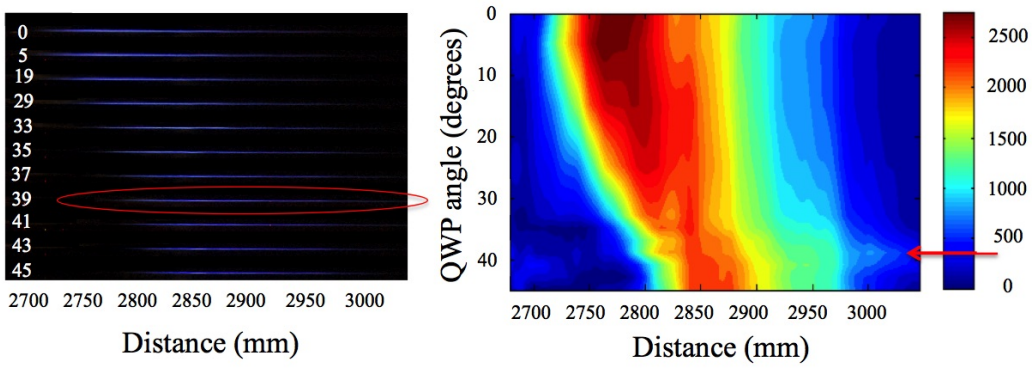

Figure 5.17: Images of the filament (integrated over 300 shots) in 0.7 atm N_2 for different QWP angles (left). Corresponding color coded graph is shown in the right [4, 12].

in filaments induced by elliptically polarized pulses.

5.5.3 Filament position and length

The unusual broadening described above must be the result of polarization-induced modifications to the filament properties. There was also an unexpected lengthening of the filament observed, at the same polarizations that resulted in spectral broadening and polarization modification in molecular gases. To measure the filament length, transverse plasma emission from N_2 was imaged with a camera as the angle of the quarter wave plate was changed [156]. The results shown in Fig. 5.17, indicate that the collapse position gradually moves away from the lens as the polarization changes from linear to circular. This is consistent with the reduced strength of χ^3 effects for circular as compared to linear polarization, delaying the onset of filamentation due to weaker self-focusing [147]. However, for the QWP angle of 39 degree, the filament is observed to extend further from the focusing lens, indicating that

the self-focusing and plasma defocusing are balanced over a longer distance.

5.5.4 Discussion

To explain this anomalous broadening and polarization change which is specific to molecular gases, molecular alignment and strong field ionization effects are the first factors that come to mind. The polarized pulse experiences a different effective nonlinear refractive index depending on the angle of the polarization with the aligned molecules. Ionization effects would only become significant once filamentation begins and the plasma is generated. Similar results were shown by Lim et al. [155] performing the similar measurements with 58fs, 4.5mJ pulses and different NA focusing in air. They defined two regimes of filamentation based on the NA used for focusing the beam: (i) linear-focusing when using high NA optics and (ii) non-linear focusing regime in the case of low NA focusing. In the linear-focusing regime, the trend in air is similar to what has already been observed in atomic gases. In our study, the effects of polarization are also barely noticeable. Compared to the spectrum at linear polarization, the spectrum at circular polarization was redistributed to the shorter than the longer wavelengths, with a comparable spectral width [155]. The transition between linear- and nonlinear-focusing regimes is characterized by a minimal spectral broadening. The spectral broadening observed at the gas-specific ellipticity could be comparable or even greater than at linear in the right conditions.

5.5.5 Effect of pressure: Multi-filamentation

Increasing the pressure resulted, as expected, in multiple filamentation. Two filaments were clearly observed in nitrogen at 1 atm (Fig. 5.18a). The spectral broadening enhancement was observed for two different ranges of QWP angles. This could be interpreted as either an interaction effect between both filaments or each filament exhibiting SCG enhancement at a different ellipticity (still symmetric around circular polarization). In argon at 1 atm, multi-filamentation also occurred for polarization closer to linear (Fig. 5.18b). The initial polarization showed a very small influence on the spectrum, compared to the results at 0.7 atm (Fig. 5.13c). The distribution of filaments was dependent on the QWP angle, but at least one filament was always present (Fig. 5.18 c and d).

5.5.6 Simulation and modeling

In this section, theoretical modeling (performed by John Palastro) of filamentation in molecular gases by including a self-consistent linear density matrix treatment of the rotational dielectric response of the molecules subjected to arbitrary light polarizations in a nonlinear propagation model, is presented. Previous simulations carried out using the same model [135], indicated that strong coupling of left- and right-handed circular polarization states arises from off-diagonal terms in the molecular susceptibility tensor, resulting in similar anomalous behavior to the observations in these experiments. The laser pulse evolution and supercontinuum generation are simulated using the modified paraxial wave equation in azimuthally symmetric, cylindrical coor-

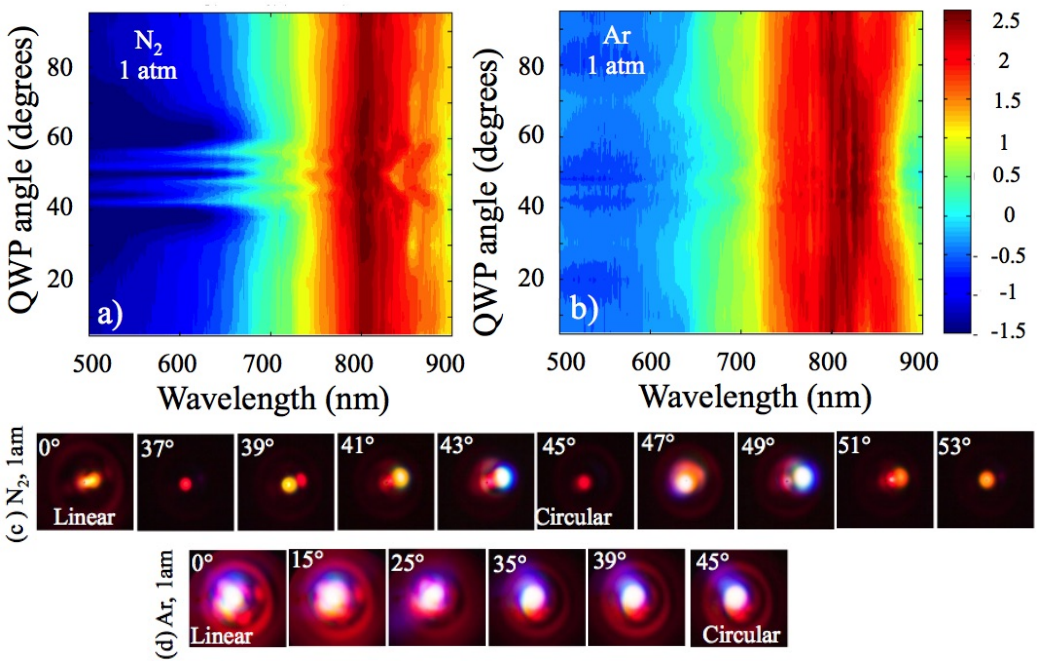

Figure 5.18: Spectral measurements of a) nitrogen and b)argon at 1 atmosphere. Pictures of the beam taken after the filament for c) nitrogen and d) argon in 1 atm [12].

dinates. The transverse vector electric field, $\mathbf{E}_F$, is expressed as an envelope $\mathbf{E}$, modulated by phase: $\mathbf{E}_F = \mathbf{E}(r,z,t)e^{-ik\xi} + c.c.$, where the pulse envelope evolves according to:

$$[\nabla_\perp^2 + 2\frac{\partial}{\partial z}(ik - \frac{\partial}{\partial \xi}) - \beta_2 \frac{\partial^2}{\partial \xi^2}]\mathbf{E} = 4\pi(ik - \frac{\partial}{\partial \xi})^2 \mathbf{P}_{NL}. \tag{5.1}$$

In Eq. 5.1 $k = \omega_0 c^{-1}[1 + \delta\varepsilon(\omega_0)/2]$, $\delta\varepsilon(\omega)$ is the shift in dielectric constant due to linear dispersion, $\xi = v_g t - z$ is the group velocity frame coordinate, $v_g = c[1 - \delta\varepsilon(\omega_0)/2]$ and $\beta_2/\omega_0 c = (\partial^2 k/\partial\omega^2)\ |_{\omega=\omega_0} = 20 fs^2/m$ accounts for group velocity dispersion. The nonlinear polarization density, $\mathbf{P}_{NL} = \mathbf{P}_{elec} + \mathbf{P}_{rot} + \mathbf{P}_{free} + \mathbf{P}_{ioniz}$, includes the instantaneous (Kerr) re-

sponse, the delayed molecular rotational response, the free electron response, and ionization energy losses respectively. The electronic and rotational polarization densities can be expressed as the product of an effective susceptibility matrix and the electric field envelope: $\mathbf{P}_{elec} = \chi_{elec}\mathbf{E}$ and $\mathbf{P}_{rot} = \chi_{rot}\mathbf{E}$. Using the circularly polarized basis, the effective susceptibility matrix elements are given by

$$(\chi_{el})_{LL} = \frac{1}{6\pi^2}(\frac{N_g}{N_{atm}})n_{2,g}(\mid E_L \mid^2 + 2 \mid E_R \mid^2) \tag{5.2a}$$

$$(\chi_{el})_{LR} = 0 \tag{5.2b}$$

$$(\chi_{rot})_{LL} = \frac{N_g(\Delta\alpha)^2}{15\hbar}\Sigma_j C_j \int_{-\infty}^{\xi} sin[\omega_{j+2,j}(\acute{\xi} - \xi)/c](\mid E_L \mid^2 + \mid E_R \mid^2)d\acute{\xi} \tag{5.2c}$$

$$(\chi_{rot})_{LR} = \frac{2N_g(\Delta\alpha)^2}{5\hbar}\Sigma_j C_j \int_{-\infty}^{\xi} sin[\omega_{j+2,j}(\acute{\xi} - \xi)/c]E_L E_R^* d\acute{\xi} \tag{5.2d}$$

where

$$C_j = \frac{(j+1)(j+2)}{2j+3}[\frac{\rho^0_{j+2,j+2}}{2j+5} - \frac{\rho^0_{j,j}}{2j+1}] \tag{5.3}$$

N_g is the gas density, N_{atm} is the gas density at 1 atm, n_2 is the instantaneous Kerr coefficient at 1 atm [157], $\Delta\alpha$ is the anisotropy of molecular polarizability [158], j is the total angular momentum quantum number, $\omega_{j+2,j} = \hbar(2j+1)/M$, M is the molecular moment of inertia, the $\rho^0_{j,j}$ are the thermal equilibrium density matrix elements and the remaining matrix elements can be obtained via L-R suffix interchange [135]. The values of n_2 and $\Delta\alpha$ are taken from Refs. [157] and [158] respectively, and are given in table 5.1. Rotational states up to $j = 25$ were included in the sums. The free electron and ionization damping polarization densities are determined

Gas species	$n_2(10^{-20}cm^2/W)$	$\Delta\alpha(10^{-25}cm^3)$
N_2	7.4	9.3
O_2	9.5	11.4

Table 5.1: Nonlinear coefficients used in the simulations [4].

by

$$(ik - \partial_\xi)^2 \mathbf{P}_{free} = (4\pi)^{-1} k_p^2 \mathbf{E} \tag{5.4}$$

and

$$(ik - \partial_\xi)\mathbf{P}_{damp} = -\kappa_{ion}\mathbf{E} \tag{5.5}$$

where

$$\kappa_{ion} = \frac{1}{2c} U_I \nu_I n_g \frac{1}{\mid E \mid^2} \tag{5.6}$$

is the damping rate, $k_p^2 = 4\pi e^2 n_e / m_e c^2$ is the plasma wavenumber, n_e is the free electron density, U_I is the ionization potential, ν_I the cycle averaged ionization rate [135, 159] and $\partial_\xi n_e = c^{-1}\nu_I n_g$. Additional details about the response model can be found in Ref. [135].

Simulated and experimentally measured supercontinuum spectra resulting from filamentation in molecular and atomic gases are compared in Fig. 5.19. The strong qualitative agreement between experiments (Fig. 5.19 left column) and simulations (Fig. 5.19 right column) carried out under identical conditions, along with the fact that there is no anomalous behavior in atomic gases, indicate that the necessary physics for describing the anomalous behavior is included in the rotational contribution to the molecular susceptibility. The main physical mechanism implied by our simulation is a polarization dependent pulse shaping, resulting in a second self-focusing event and pulse

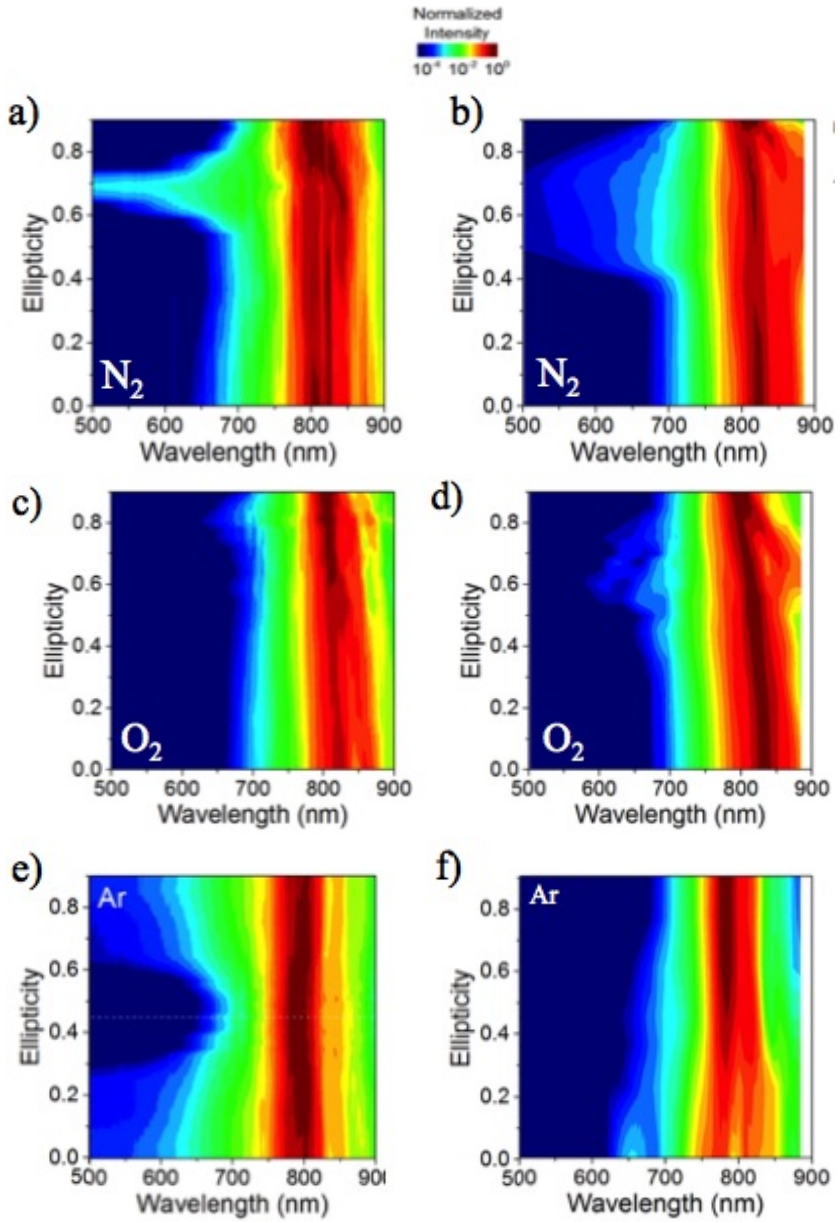

Figure 5.19: Experimental (a, c, e) and simulated (Courtesy of John Palastro) (b, d, f) results are compared for filamentation in nitrogen (a, b) and oxygen (c, d) and argon (e, f) [4].

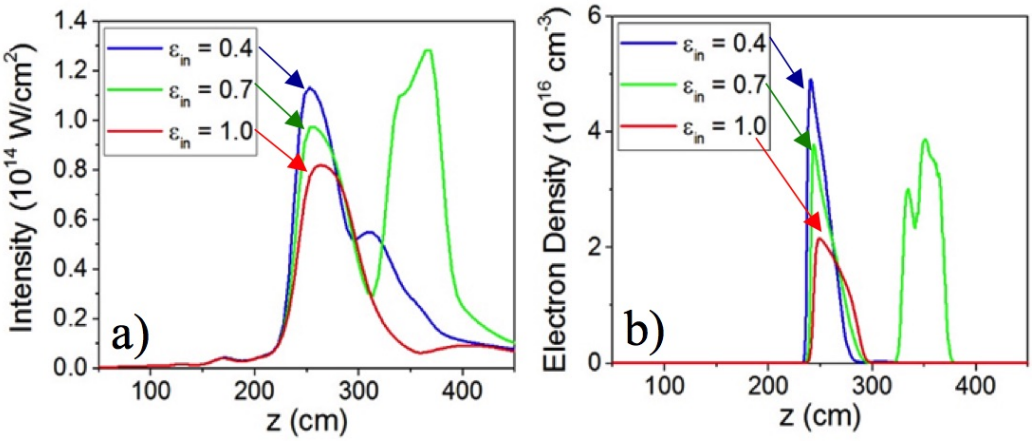

Figure 5.20: Dependence of the on axis intensity and electron density on propagation and initial ellipticity. a) Simulated peak intensity and b), on axis electron density for initial polarizations of $\epsilon_{in} = 0.4$(blue) $\epsilon_{in} = 0.7$(green) and $\epsilon_{in} = 1$(red), in Nitrogen. The distance z is measured from the focusing lens, with the geometrical focus located at z=300 cm (Courtesy of John Palastro).

self-steepening at particular elliptical polarizations. More theoretical work is required to match the range of ellipticities for which enhanced SCG is observed, and the particular value of ellipticity for which optimal enhancement is observed in each gas. Other mechanisms such as ellipticity dependencies in the ionization rates or population of excited states could also be involved in explanation of the ellipticity dependent filamentation process [160], and are not accurately taken into account in the simulations.

The simulated results allow us to investigate more carefully the spatio-temporal evolution of the filamenting pulse for different input ellipticities. Figure 5.20, shows the on-axis peak intensity and electron density for filaments created in N_2 from pulses with input ellipticities ϵ_{in} =0.4, 0.7 and 1. As mentioned above, the reduced strength of both $\chi^{(3)}$ effects and multi-

photon ionization for larger values of ellipticity results in a higher on-axis peak intensity at the filament collapse location (Fig. 5.20a, z≈ 250 cm after the focusing lens), and in turn a higher electron density (Fig. 5.20b), for smaller values of ellipticity. Interestingly, however, for the input ellipticity $\epsilon_{in} = 0.7$, a second self-focusing event occurs (z≈ $350cm$), reaching higher values of both on-axis intensity and electron density than at the initial collapse location. Only in the case of $\epsilon_{in} = 0.7$ a significant self-steepening of the pulse during this second self-focusing event is observed, resulting in the dramatic broadening of the supercontinuum spectrum (Fig. 5.21b) and the modification of the supercontinuum polarization state (Fig. 5.22) for this particular value of input ellipticity. Experimentally, this phenomenon was not observed as a secondary plasma event but nonetheless as an elongation of the initial plasma channel. The second self-focusing event can be explained by coupling between the left- and right-handed circular polarization states. The simulations indicate that energy exchange between the two states tend towards an equal energy sharing between left- and right-handed circular polarization, with the dominant polarization state transferring energy into the weaker polarization state during propagation (Fig. 5.23). The different self-focusing and ionization for different initial ellipticities result in conditions which are more or less favorable for a second self-focusing event: (1) For small input ellipticities, the initial nonlinear focus is strong, creating a large amount of plasma which in turn strongly refracts the pulse. The high intensity allows rapid energy equilibration between the two polarization states; however any further refocusing is diminished because of the large refraction. (2) For intermediate ellipticities, the initial nonlinear focus is more mild, al-

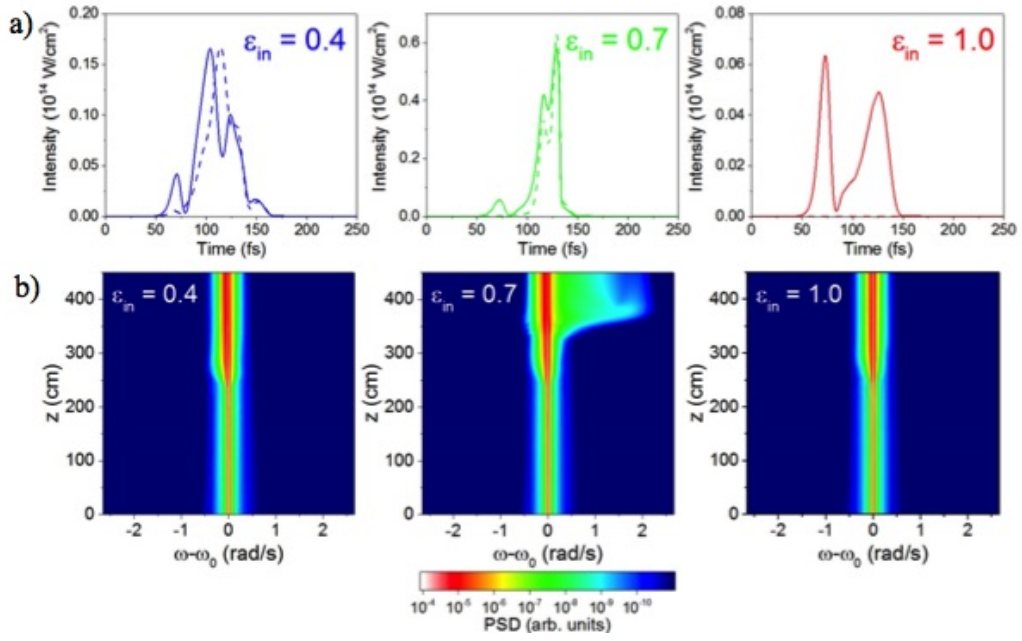

Figure 5.21: a) Time-dependent intensities of right- (solid lines) and left-handed (dashed lines) circular polarization components for input ellipticities of ϵ_{in} =0.4, 0.7, and 1 at z=350 cm. Strong self-steepening is observed for ϵ_{in}=0.7. b) Evolution of the supercontinuum spectrum with propagation distance. At the location of the second nonlinear focus (z≈350 cm), a large shift of the spectrum to higher frequencies is observed (Courtesy of John Palastro).

lowing the dominant polarization state to refocus and therefore to strengthen the coupling between the two polarization states. For ϵ_{in} =0.7, it is found that the energy of left- and right-handed circularly polarized states is nearly equal following this second self-focusing event, resulting in a reduction of the measured output ellipticity. (3) For large ellipticities, the initial nonlinear focus is significantly weaker, and the refocusing is prevented by the small nonlinear index for near-circularly polarized pulses.

The difference in the optimal input ellipticity for SCG in N_2 and O_2 gases can

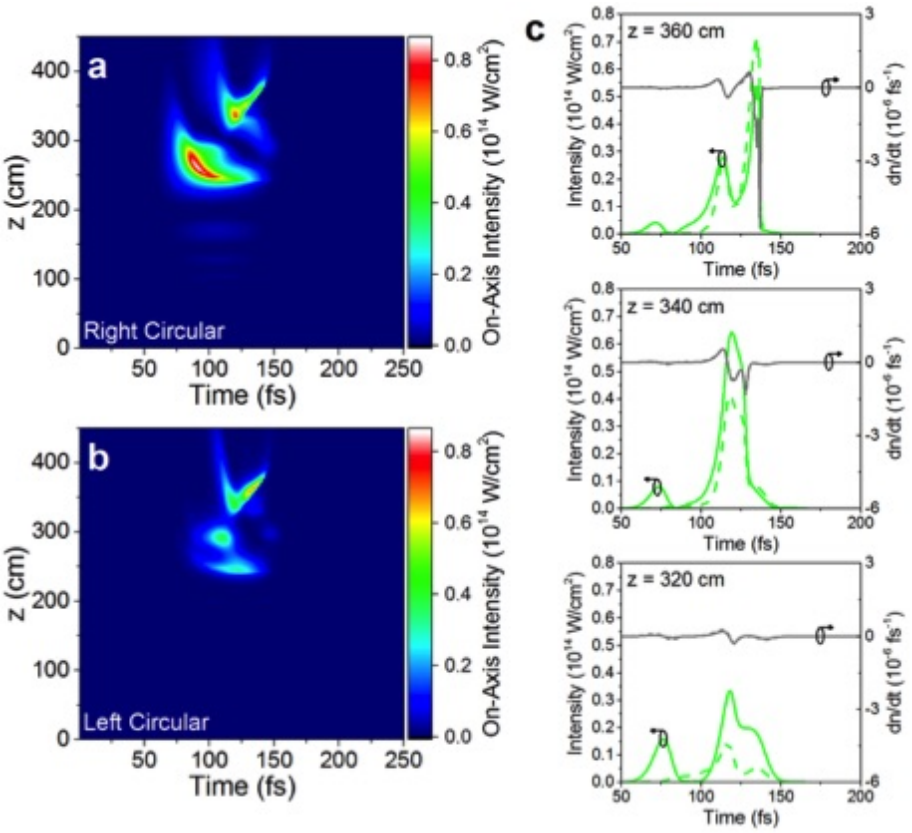

Figure 5.22: On-axis intensity profiles during propagation for (a) the right- and (b) left-handed circularly polarized components, with ϵ_{in} =0.7. Self-steepening of the pulse is apparent for z>300 cm. c) Variation of the intensity (green) and refractive index with time (dn/dt, gray) for z=320, 340, and 360 cm. Right- and left-handed circular polarization components are indicated by solid and dashed lines, respectively. The negative values of dn/dt at the trailing edge of the pulse at z=360 cm are responsible for the blueshift of the spectrum (Courtesy of John Palastro).

be explained by the coupling strength between left- and right-handed circular polarizations. This coupling is determined by the off-diagonal components of the susceptibility matrix $(\chi_{rot})_{LR}$, which are proportional to $\Delta\alpha^2$, where $\Delta\alpha$

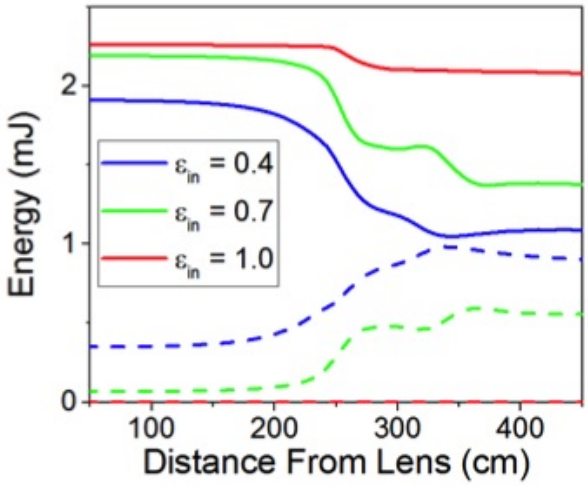

Figure 5.23: Evolution of the right- (solid lines) and left-handed (dashed lines) circular polarization states with propagation. Note that for ϵ_{in}=0.4 and ϵ_{in}=1.0, energy equilibration occurs at the location of the first initial nonlinear focus (z≈250 cm), while for ϵ_{in}=0.7 a second equilibration step occurs at the second focus later (z≈350 cm) (Courtesy of John Palastro).

is the difference in the molecular polarizability parallel and perpendicular to the molecular axis. Therefore, larger $\Delta\alpha$ results in more coupling between polarization states, and a larger disparity between left- and right-handed circular polarization states can be corrected during propagation. Thus, for larger $\Delta\alpha$ we expect that the optimal input ellipticity for SCG will be closer to circular polarization, where there is a larger imbalance between the left- and right-handed components. In the cases studied here, O_2 has a larger value of $\Delta\alpha$ than N_2, and we observe enhanced SCG in O_2 for a larger value of input ellipticity.

5.5.7 Conclusion

Measuring the fluorescence from the plasma in vacuum shows high ionization at the geometrical focus. The spatio-temporal shape of the pulse is very quickly modified, resulting in a rapid decay of the electron density, followed by a resurgence as the pulse takes a quasi steady state shape.

Dynamic spatial replenishment is clearly seen when the filaments are prepared in air. Measurements of the side emission of the plasma at a fixed position, showed an unexpected increase in the signal at 9mJ as the input energy was increased to 30mJ. Polarization dependence measurements at the fixed position in air, showed an increase in the signal close to circular as the polarization was changed from linear to circular that was not observed for filaments prepared in vacuum.

Polarization dependent spectral broadening enhancement near circular polarization was observed. This anomalous behavior is specific to molecular gases, and coincides with a decrease in the final ellipticity of the beam as well as an elongation of the plasma channel by the filament. Both experimental and simulated results clearly demonstrate the strong dependence of filamentation on the input laser ellipticity via the delayed rotational response of the molecular medium. This study introduces an additional tool, polarization ellipticity, to control SCG and enhance the white light spectrum. Polarization is therefore a new dimension to control, in applications of filamentation such as the generation of few-cycle pulses and white light LIDAR where the generation of supercontinuum is a key.

Chapter 6

Radiation from the filament

6.1 Light with orbital angular momentum

John Henry Poynting introduced the notion of angular momentum for circularly polarized light in 1909 [161]. This momentum could take the value $\pm\hbar$ for each photon. The more general concept of orbital angular momentum independent of the polarization was exposed in 1992 [162]. It is expressed as an azimuthal phase $\exp(im\phi)$ with m the "topological charge" (integer value) and ϕ the azimuthal coordinate in cylindrical symmetry to describe the beam cross section. As shown in the expression of the phase above, this orbital angular momentum (OAM), of value M $=m\hbar$ per photon, is signed, expressing the handedness. By definition, the axis of the beam (r=0) represents a singularity which is physically acceptable since the intensity is null at the vortex core (Fig. 6.1). Therefore, the cross-sectional intensity pattern of the beam has an annular character that persists, no matter how tightly is focused. Investigations of these waves and methods to generate them were

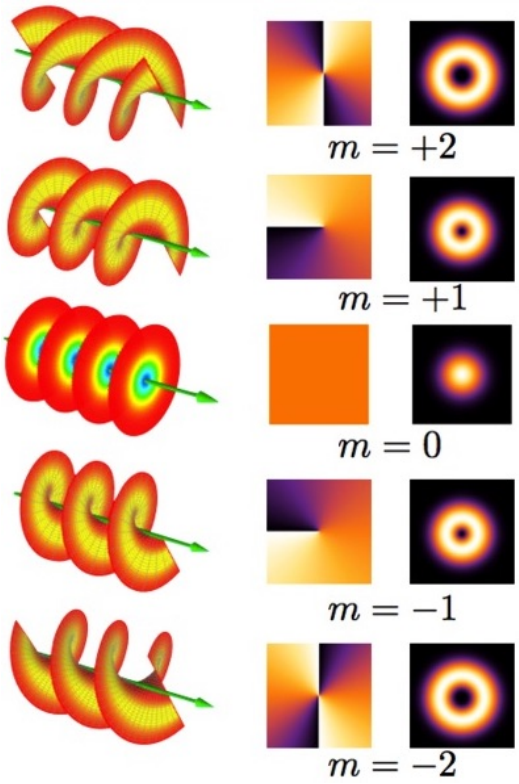

Figure 6.1: First column (left to right) shows the beam helical structure, second column the phase front and the last column the intensity distribution [13].

reported as early as 1973 by Bryngdahl [163]. Nye and Berry [164, 165] developed the theory of waves carrying phase singularities leading to introduction of the term "optical vortex" by Coullet et al. [166].

Assuming the path of the vortex lies on the optical axis, z, adding a phase factor $-kz$ to describe light propagating along z axis the phase $\Phi(r, \phi, z_c) = m\phi - kz$ is obtained, where k is the wavenumber. At a given ϕ, this phase increases linearly with ϕ and does not depend on r.

6.1.1 Generating optical vortices

The spin angular momentum is not dependent of the phase, but on the beam polarization [14]. Beams carrying spin angular momentum are easily generated by converting linearly polarized to circularly polarized light using a quarter wave plate. Cylindrical lenses were used by the Leiden group to transform an Hermite -Gaussian (HG) beam with no angular momentum into a Laguerre -Gaussian (LG) beam that carries orbital angular momentum (see Fig. 6.2) [167]. In this highly efficient conversion process, each LG mode requires a specific initial HG mode which limits the range of producible LG modes. Numerically computed holograms with the ability of generating any desired value of orbital angular momentum from the same initial beam are the most common method to create helical beams. The hologram can be made by recording the computed interference pattern between a plane wave and the beam one seeks to produce, onto photographic film. Nanolithography may be used to create diffractive optical elements with sub-micrometer features. Contact lithography may also be used, which is based on using many well-aligned master masks to achieve adequate phase resolution, making it a labor intensive approach. Fortunately, the advent of computer-generated holography (CGH) and the availability of high quality laser printers allows a fast, inexpensive means of producing vortex holograms [168, 169].

6.1.2 Filaments with orbital angular momentum

Beam shaping has been extensively investigated as an effective control tool over femtosecond laser filamentation in gases . The doughnut-shaped in-

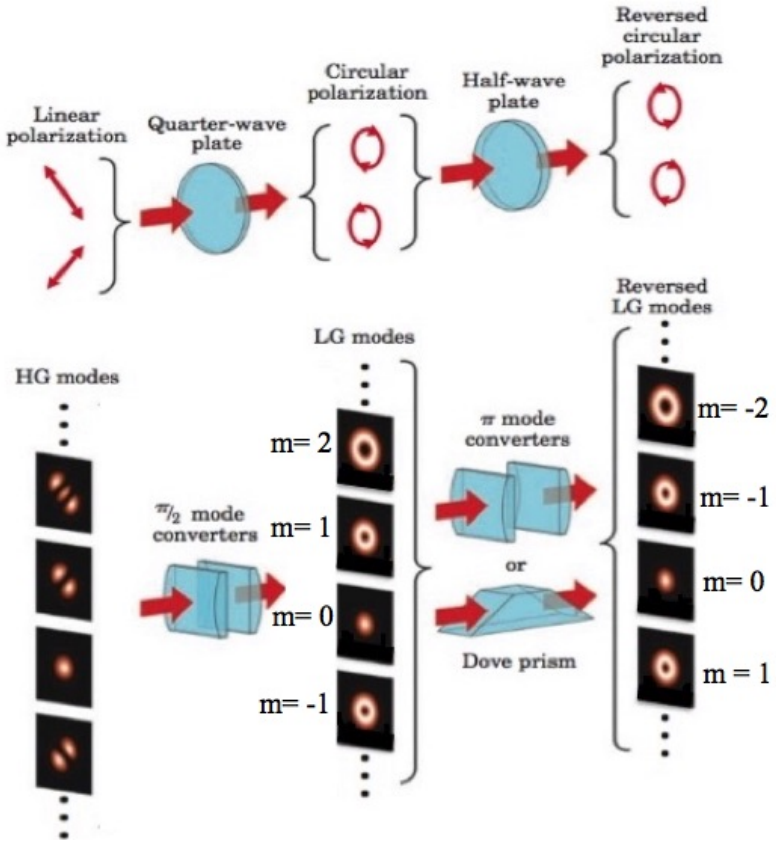

Figure 6.2: Transformation of a Hermite-Gaussian (HG) mode into a Laguerre-Gaussian (LG) mode carrying orbital angular momentum with a pair of cylindrical lenses. The handedness of the LG mode can be reversed by increasing the space between the cylindrical lenses or with an image inverter such as a Dove prism [14].

tensity distribution of optical vortices, makes them particularly interesting in this context. Optical vortices have been used to increase the fidelity of optical testing and improve optical measurements [170, 171], for investigations in high-resolution fluorescence microscopy [172], optical lithography [173, 174] and quantum entanglement [175–177]. Also optical vortices can be potentially used in channeling microwave radiation by generating an ex-

tended "bottle-like" distributions of plasma filaments in air [83, 178–180]. Their greater power carrying ability and increased information content [181] is of great interest as well. Thus it is of considerable importance to determine the stability of ring beams propagating in nonlinear optical medium and the characteristics of the filaments that are originated from these beams.

The dynamics of optical vortex beams propagating in a nonlinear medium has been a subject of interest in many studies. It was shown by Vincotte et al. [182] that for vortices with input power $P \approx P_{cr}(m)$, the vortex ring breaks into $(2m+1)$ filaments due to symmetry breaking noise. This conclusion was generalized by Vuong et al. for vortices with power above critical power (Eq. 6.1) [183].

On the other hand it was also experimentally observed that In a saturable nonlinear material (such as sodium vapor), beams with an orbital momentum (m) split into non-rotating filaments $(2m)$ [184] as also was predicted by Firth and Skryabin [185].

There has been discrepancies over the critical power for self-focusing of vortex beams, as a function of its order. Critical power presented in Eq. 6.1 was reported by Vuong et al. [183].

$$P_{cr}^{(m)} = \frac{2^{2m+1}\Gamma(m+1)\Gamma(m+2)}{2\Gamma(2m+1)} P_{cr} \tag{6.1}$$

with $\Gamma(m) = (m-1)!$. This was simplified further by Fibich et al. to $P_{cr}(m) \approx 4\sqrt{3}mP_{cr}(0)$, where $P_{cr}(0)$ is the critical power for a Gaussian beam in the same medium [186]. They also reported the critical power for circularly polarized vortex as [186].

$$P_{cr}^{CP}(m) = \frac{3}{2} P_{cr}(m) \approx 6\sqrt{3}m \tag{6.2}$$

Any deviation from the radial symmetry leads to the collapse into non-vortex filament instead of increasing the critical power [186]. It was shown by Polynkin et al.[187] that with slight modulations of the transverse intensity (below 10%) "the dominant mode of self-focusing collapse is found to be the azimuthal breakup of vortex rings into individual filaments". The number of filaments, for a specific vortex order, increases with input power and the pattern rotates accordingly to the initial sign of the topological charge.

6.1.3 Emission from vortex plasma filaments

The first coherent Laguerre-Gaussian white-light beam generated from a femtosecond supercontinuum light source was reported by Sztul et al. [188] and showed a similar spectral broadening to a Gaussian beam. The supercontinuum induced in solids by femtosecond pulses carrying an orbital angular momentum was shown to be caused by the OV undergoing filamentation where each filament creates independently its own continuum. As a consequence, the phase information is not transferred from the vortex to the supercontinuum. This is observed as a background signal around the fundamental OV. There was no clear difference between the supercontinuum generated with linear compare to circular polarization [189].

Comparative numerical analysis of the propagation dynamics of conventional and vortex pulses in air have revealed some significant differences inherent in the self-focusing of the latter [190]. The frequency and angular spectra are significantly broadened during the self-focusing of vortex beams in comparison with the vortex-free regimes. This difference is due to the higher

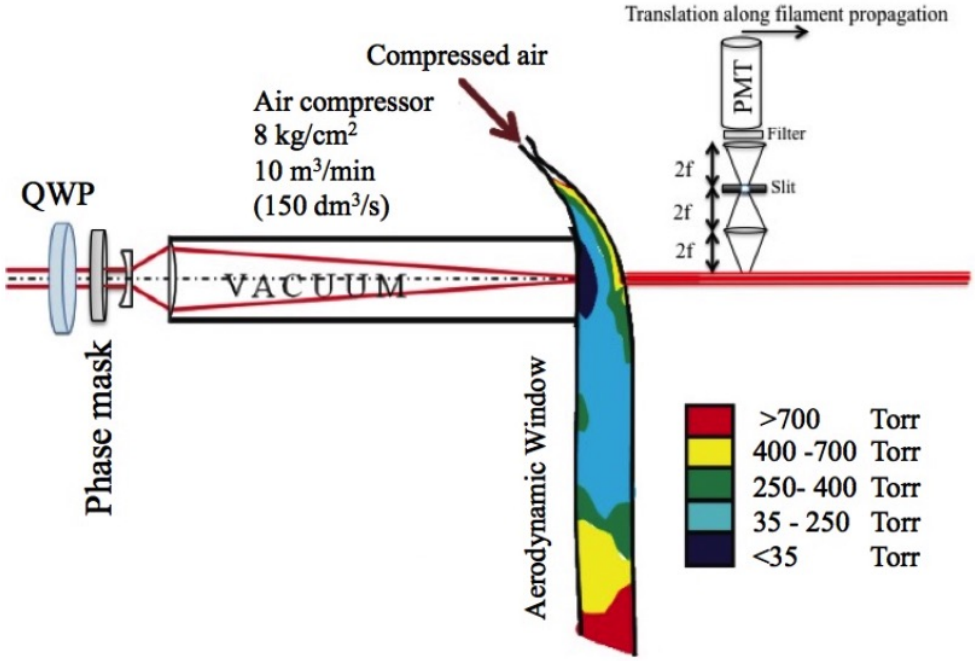

Figure 6.3: Experimental setup used to measure the emission from the vortex filament prepared in air and vacuum. zero order QWP was used to control the polarization before the focus. 2f imaging configuration was used to collect all the light from the side and focus on the PMT.

peak intensity and localization of the vortex pulse of a higher power in the focal spot. The azimuthal instability of vortex pulsed beams in media with normal dispersion limits the distance of their stable propagation in air. However, at sufficiently small initial amplitude and phase perturbations of the wave front of the initial pulse the distance of stable propagation of optical vortices with topological charge m = 1 can exceed the length of the nonlinear self-focusing. The differences demonstrated point to the fact that the use of the vortex pulses in the problems of remote sensing of the atmosphere is quite promising.

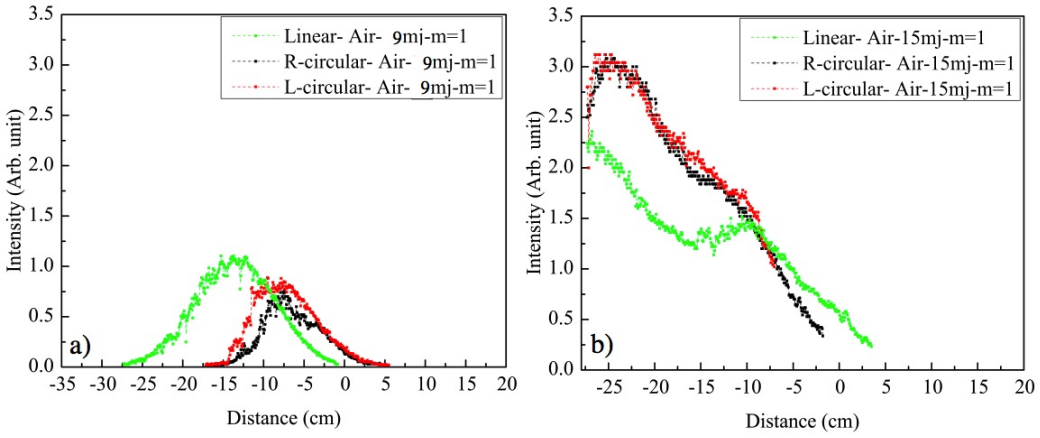

Figure 6.4: Side emission of the plasma filament with angular momentum focused in air, at 337nm for 100fs pulses at a) 9mJ and b)15mJ. In both figures $z = 0$ is the geometrical focus.

6.1.4 Experimental details and discussion

Experimental setup was similar to Fig. 5.4 that was used to measure the side plasma emission, with the difference of using an appropriate phase mask (provided by Dr. Eric G. Johnson's group, at Clemson university [191]) after the wave plate to create filaments with orbital angular momentum (Fig. 6.3). Side emission of the vortex (m=1) filaments at 337nm, with initial linear, left- and right- handed circular polarization, prepared in air and vacuum is measured. Figure 6.4a, shows the side emission from excited nitrogen molecules (337nm) for filaments with orbital angular momentum and 9mJ energy, prepared in air. The fluorescence maximum shows an earlier starting point for linear polarization compared to circular polarized vortex filaments. The intensity of the fluorescence also shows a slightly stronger peak in the case of linear polarization and no relation to helicity of the circular polarized fila-

ments (red and black). Increasing the energy to 15 mJ also confirms the same results (Fig. 6.4b).

At first glance, our observations don't agree with supercontinuum generation in solid state materials which showed no difference between linear and circular polarized filaments with angular momentum [189]. In an attempt in our group (by Amin Rasoulof), looking at the effect of optical vortices on forward emission from filament at 428nm, there was also no difference between the emission peak with linear and circular polarization.

In a closer comparison between results presented in Fig. 6.4 and the side emission measurements done with no mask (Fig. 5.7), there is less difference between the peak intensities of linear and circular polarizations in the case of vortex filaments. Higher critical power to self focus filaments with orbital angular momentum, leads to less energy reservoir which could explain hav-

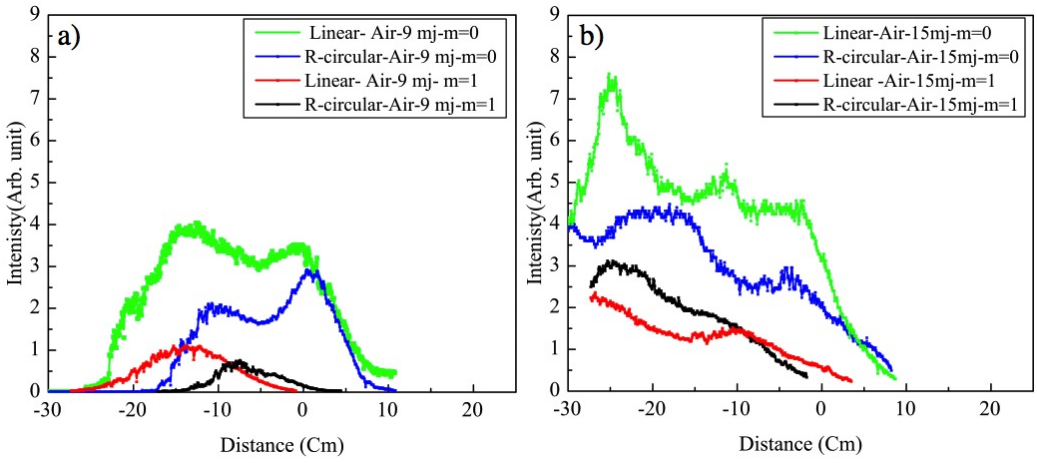

Figure 6.5: Comparison of the side emission of the plasma filament with (m=1) and without (m=0) angular momentum focused in air, at 337nm for 100fs pulses at a) 9mJ and b)15mJ.

ing less emission, shorter plasma with no dynamic replenishment, compare to (m=0) measurements. Also, the azimuthal instability of vortex pulsed beams in media with normal dispersion limits the distance of their stable propagation in air, which is shown in Fig. 6.5. Higher peak intensity during the self-focusing compared to conventional pulses have been reported in the case filaments with angular momentum [190]. Taking into account the fact that the radiation power in the focal spot of the vortex beam is many times higher than the power of the focused conventional beam, one should expect more significant manifestations of plasma nonlinearity due to multi-photon absorption and ionization of air. The excess over the ionization threshold during the self-focusing leads to dissipative processes that result in energy loss. Higher energy loss explains less plasma emission (detectable over a shorter distance) from filaments with orbital angular momentum.

To study the effect of the nonlinear medium before the filaments are created, the beams with embedded angular momentum was focused in transition between vacuum and air. There was no radiation detected within the sensitivity of our detection system from the vortex filament prepared with initially circular polarization at 9mJ (Fig. 6.6-red). This observation could be explained with the combination of higher critical power, and reduced $\chi^{(3)}$ effects for circularly polarized beams. Effect of polarization could be seen with reduction in detected side emission as the polarization is changed from linear to circular (green,blue, red). In order to be able to reach the critical power with circular polarized vortex, the input energy was increased to 15mJ (Fig. 6.6-black).

Figure 6.6 shows that the maximum fluorescence occurs further in the propa-

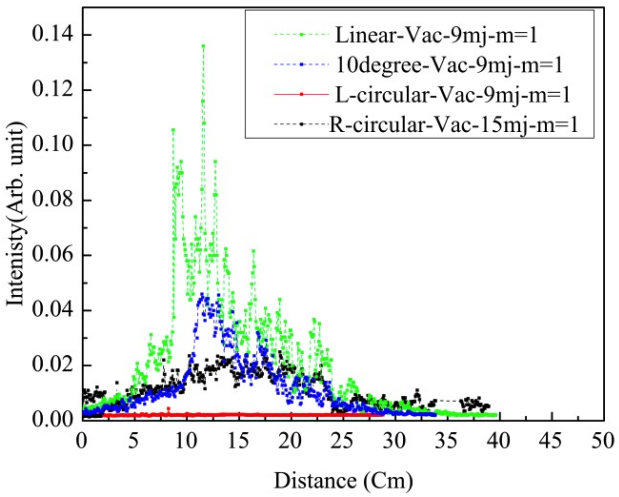

Figure 6.6: Side emission of the plasma filament with angular momentum focused in vacuum, at 337nm for 100fs pulses with different initial polarizations and 9 and 15mJ input energies.

gation with much less intensity when the beam is focused in vacuum which is in contrast with observing high emission at the exit of the window followed by a fast decay for the filaments with no angular momentum (Fig. 5.6a). Plasma emission from a vortex filament created with no nonlinear preparation is observed for a shorter distance and the recorded signal shows a lot more modulations compared to when it is prepared in air (Fig. 6.4). These observations point to the fact that propagation in the nonlinear medium before vortex filaments start, is needed to counteract their azimuthal instability.

6.1.5 Spectral characterization

In order to study the effect of the phase mask on the generated supercontinuum, 2 prisms and a set of razor blades (0.5 mm separation) were used

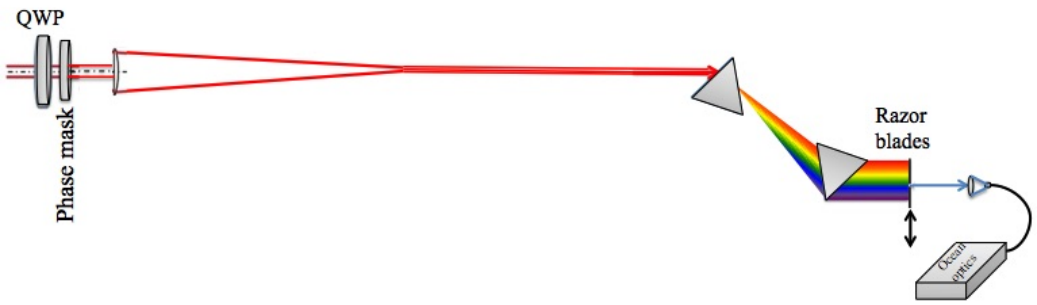

Figure 6.7: Experimental setup to measure the spectrum of the vortex filament.

to measure the separated spectrum after propagating the filament for about 1.5 meter. The schematic of the setup is shown in Fig. 6.7. 800 nm, 100 fs pulses with input energy of 9 mJ with initial linear or circular polarization are focused in air, at 3meters. After about 1.5 meter of propagation, the filament is attenuated enough that it could be sent through the prisms. The transmitted part of the spectrum through the blades that are setup on a translation stage, is sent to a lens (f=1.5cm) and coupled to a fiber spectrometer (OC:HR2000). The measured spectrum of a 1mJ focused beam with initial circular polarization is shown in Fig. 6.8, as a reference. This spectrum is not expected to change with polarization as long as the power stays below critical power for the nonlinear effects to kick in. As the energy is increased and the filament is created from a focus in air, the generation of shorter wavelengths are expected.

Fig. 6.9a shows the normalized measured spectrum for linear polarized filament after 1.5m propagation with the clear extension of the spectrum to below 450nm, with the inset (Fig. 6.9a-2) showing the 2-D progression of the spectrum for different positions of the slit, moved perpendicular to the beam

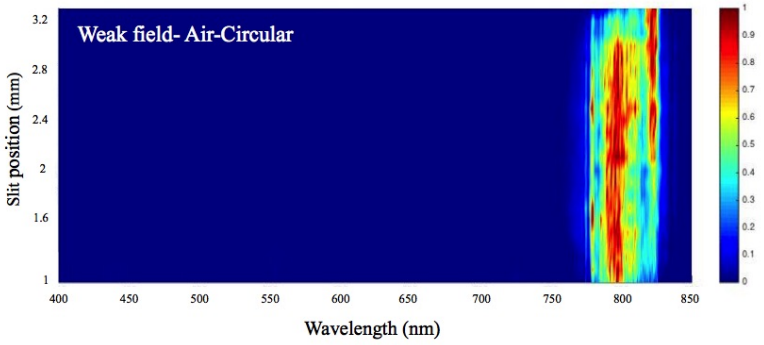

Figure 6.8: Normalized spectrum of a 100 fs, 1mJ circularly polarized beam focused at 3 meters in air, measured at 1.5 meters after the focus. Vertical axis shows the position of the blades (slit).

propagation. As the polarization is changed to circular, due to reduction of the $\chi^{(3)}$ effects, less spectral broadening is observed (Fig. 6.9b) which is in agreement with the data presented by Diels et al. [2].

The spectrum of linear and circular polarized vortices (m=1) are shown in Fig. 6.10 which indicates less difference between the two polarizations. These observations agree with supercontinuum generation in solid states which also showed no difference between linear and circular polarized filaments with angular momentum [189]. The other interesting point is that the phase mask, eliminated wavelengths generated in the mid region ($\approx$ 550-750nm), comparing to Fig. 6.9a-1 with (m=0).

6.1.6 Breakup of ring beams with orbital angular momentum

As mentioned earlier, one of the significant differences of the propagation dynamics of pulsed optical vortex beams is their inherent azimuthal insta-

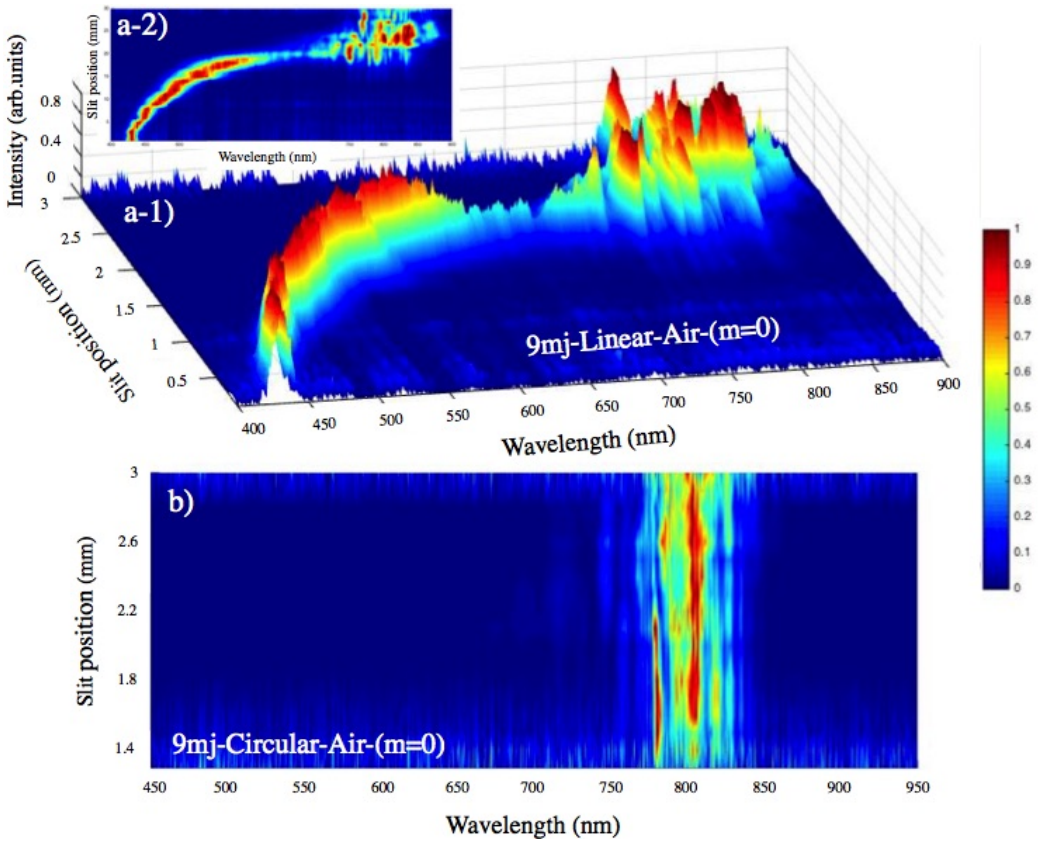

Figure 6.9: Normalized spectrum of a 100 fs, 9mJ beam focused at 3 meters in air, measured at 1.5 meters after the focus, with initial a-1) linear and b) circular polarizations. Figure a-2) shows a 2-D progression of the spectrum for different slit positions.

bility that leads to the destruction of the vortex structure and filamentation of radiation into several channels diverging from the axis of the initial beam [182–184, 187, 192].

Spectral content of the vortex components

Similar setup as in Section 4.4.1 was used with 100fs, 800 nm pulses at 5mJ going through a zero order QWP to control the polarization, followed by a

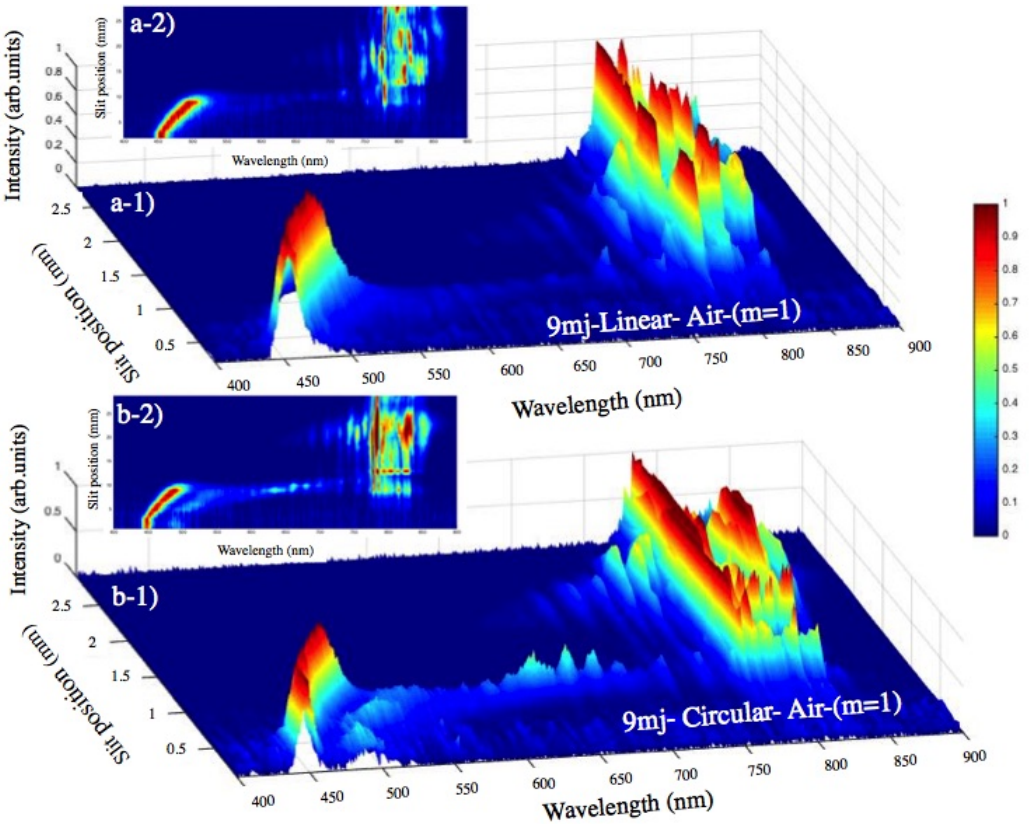

Figure 6.10: Normalized spectrum of a 100 fs, 9mJ beam with angular momentum (m=1) focused at 3 meters in air, measured at 1.5 meters after the focus, with initial a-1) linear and b-1) circular polarizations. a-2) and b-2) show a 2-D progression of the spectrum for different slit positions.

phase mask to create the optical vortex (Fig. 6.11a). The phase mask used in these experiments (provided by Dr. Eric G. Johnson's group at Clemson university), was optimized to create a donut shape beam (m=1) which broke into 2 filaments (as in reference [186]) after propagation (Fig. 6.11b) and provided the opportunity to study each filament. separately with scanning an aperture to analyze the spectrum and polarization of the desired part of

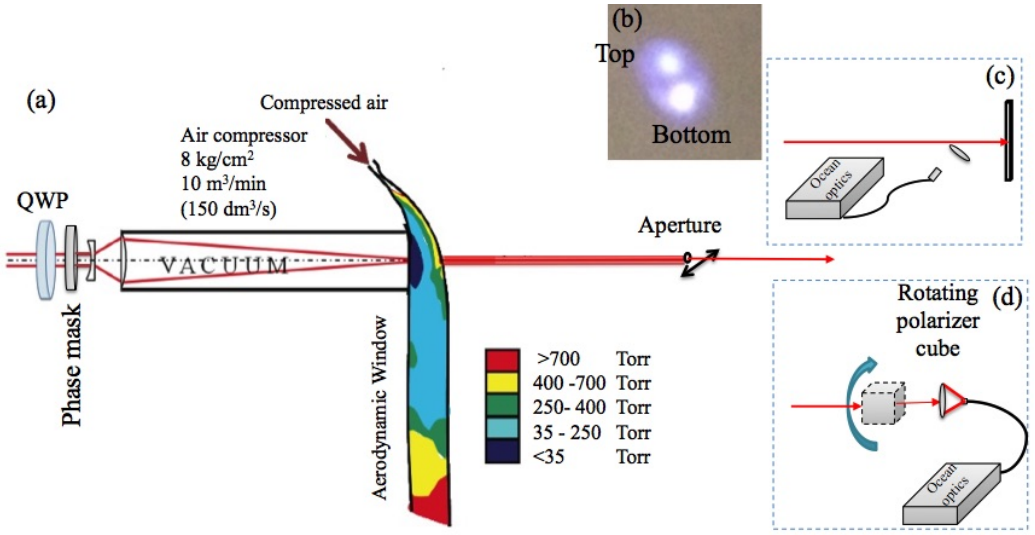

Figure 6.11: a) Setup of spectrum and polarization measurement of the filaments created with 100fs beam with angular momentum at 5 mJ, using a 3m lens. b) The ring beam breaks up into 2 filaments 120cm propagation. Selected part of the profile after the aperture is sent to either setup for (c) spectrum and (d) polarization measurments.

the profile (Fig. 6.11). Spectrum of each filament (shown as top and bottom in Fig. 6.11b) was measured for different sections across the profile, by translating the aperture horizontally to provide spatial information of the spectrum and polarization (Fig. 6.11 (a) in combination with (c)).

Figure 6.12 shows the results of the normalized spectrum for each filament. Even though they appear to be 2 separate and identical filaments to the naked eye, their spectral measurements seem to be complimentary to each other since the original spectrum created by the ring filament, is split between the two. Spectral measurements of the filaments created with no nonlinear preparation (focused in the transition between vacuum and air), show the same complimentary behavior for the top and bottom filaments with the dif-

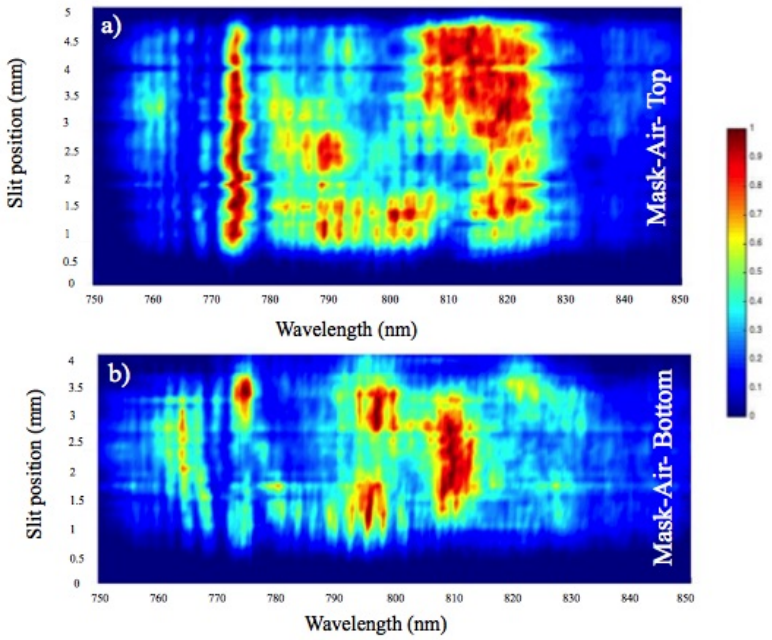

Figure 6.12: Normalized spectrum measured for the a) Top and b) bottom linear vortex filaments prepared in air, across the beam profile.

ference of having cleaner spectra (Fig. 6.13). Vortex filaments with initial linear polarization created from focusing in aerodynamic window, show minimal change in the spectrum across the profile.

Polarization of the vortex components

The other important parameter to study is the polarization after propagation and break up of the donut shaped vortex. One section of each filament (approximately the core) was sent through the polarization analyzation system (Fig. 6.11d) and the transmitted spectrum was measured for different

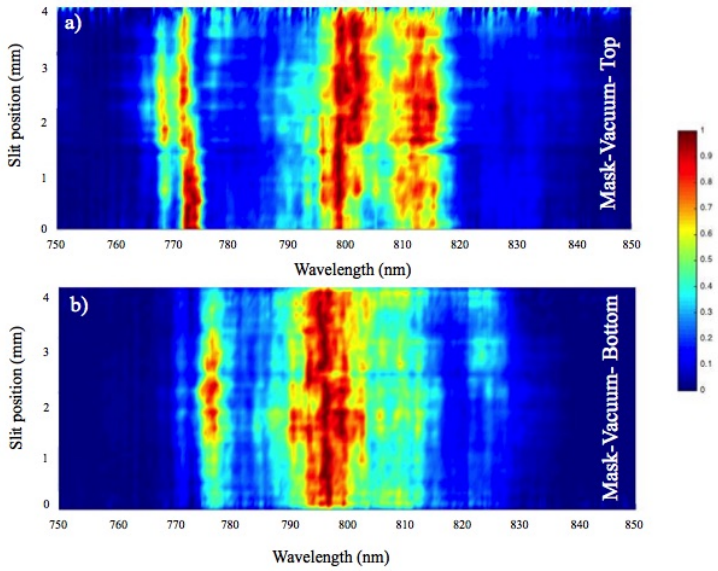

Figure 6.13: Normalized spectrum measured for the a) Top and b) bottom linear vortex filaments prepared in vacuum, across the beam profile.

initial polarizations while the polarizer cube was rotated over 180°. Figure 6.14 shows the normalized spectrum for different angles of the polarizer cube for QWP angles 38° (example of where we previously observed polarization modifications and enhanced spectral broadening (Section 5.5)) and 45° (cir-

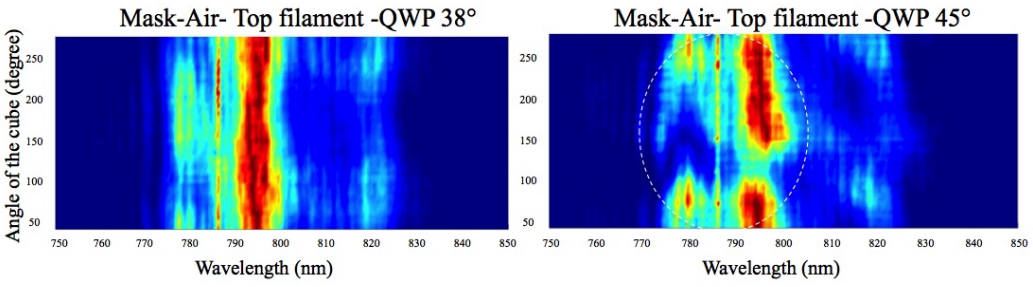

Figure 6.14: Normalized spectrum measured for the top filament with a) QWP at 38° and b) QWP at 45° (circular).

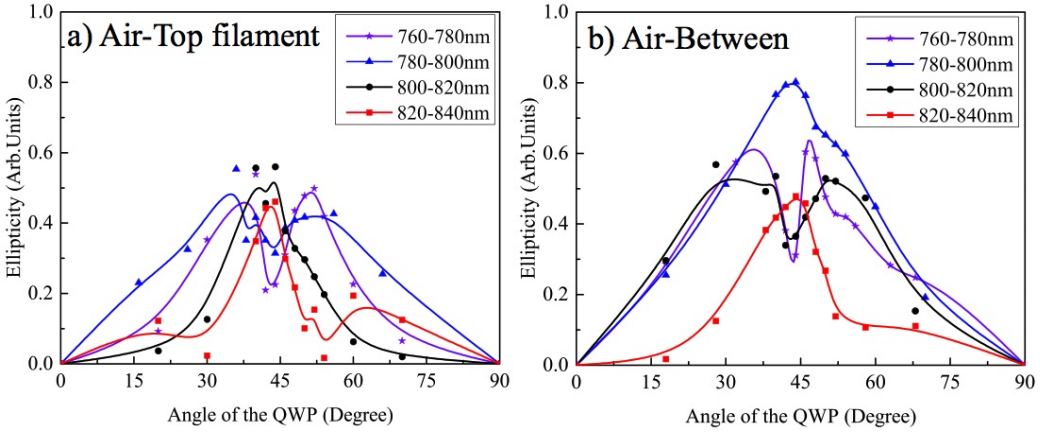

Figure 6.15: Ellipticity measured for different regions of the spectrum of a) top filament created from vortex beams focused in air and b) between the broken up filaments.

cular). Having almost constant transmitted amplitude across the rotation of the cube, is the indication of circularly polarized wavelengths. When the QWP is at 38° polarization of the transmitted wavelengths seems to be circular (Fig. 6.14a) while with initial circular polarization, blue shifted part of the transmitted spectrum has became linearly polarized (Fig. 6.14b).

In order to get a clearer picture of how the polarization for different regions of the spectrum change, the same method as described in Section 4.4.1 was used to analyze the polarization for 4 different regions of 20nm. Figure 6.15 shows the ellipticity change for different parts of the spectrum of the top (Fig. 6.15a) and the area between the separated filaments (Fig. 6.15b). As discussed in Section 4.4.1, there is more modification of the ellipticity for the blue shifted side of the spectrum (760-780nm). The main original components of the beam (780- 800nm) in the area between the two filaments have almost maintained their initial polarization (Fig. 6.15b- blue).

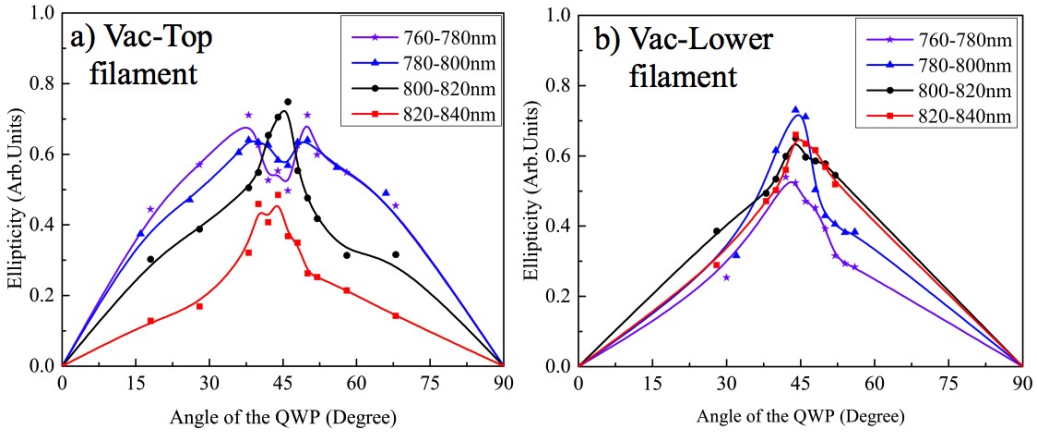

Figure 6.16: Ellipticity measured for different regions of the spectrum for a)top filament and b) lower filament created from focusing a beam with angular momentum, in vacuum and propagated in air.

Ellipticity measurements for the vortices prepared in vacuum also confirm having more modifications for the shorter wavelengths (Fig. 6.16). Changes in the ellipticity are not as dramatic as when the filaments go through the

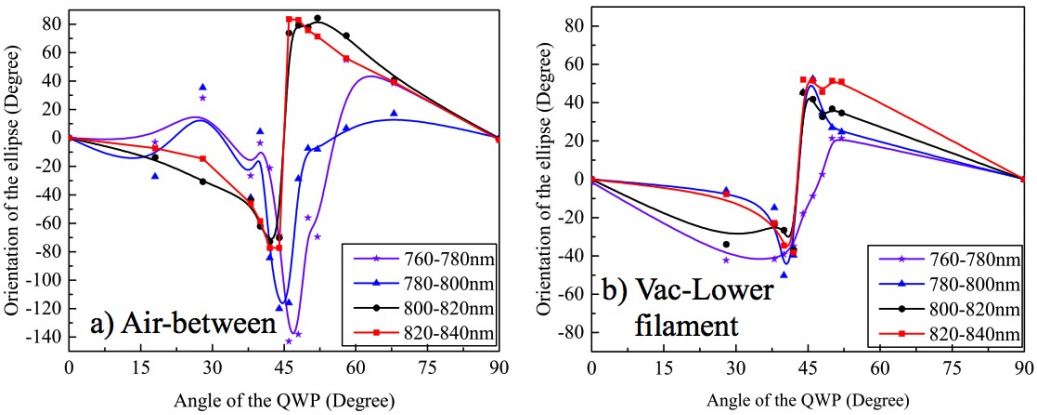

Figure 6.17: Orientation of the ellipse for different wavelengths in a) area between the two filaments when they are prepared in air and b) lower filament, prepared in vacuum.

nonlinear preparation before the focus which is clearly seen for the lower filament (Fig. 6.16 b).

The orientation of the ellipse (Fig. 6.17) for both filaments prepared in air and vacuum also agrees with our results from Section 4.5, that shorter wavelengths show more rotation.

The polarization of the blue shifted side of the spectrum that is created in the preparation and propagation phase, is very different than that of the wavelengths in the initial spectrum (780-820nm). It is not clear if these shorter wavelengths are originally created with a different polarization than the prepared one (since the polarization of the original beam is already changed before the point of continuum generation) or they go through more ellipticity modifications and rotations in the propagation phase of the filament .

6.2 Field-free molecular alignment and plasma emission

Different terms contribute in Kerr nonlinearity; instantaneous electronic part as well as the contribution from molecular degrees of freedom (orbital and vibrational). During the excitation with nanosecond pulses, thermodynamic equilibrium is maintained due to the collision time (order of ten to a few hundred picoseconds [193]) being much shorter than the pulse duration. In contrast, the effects from sub-picosecond pulses are considered non-adiabatic. For femtosecond pulses a large number of rotational and vibrational modes are populated due to the inherent large energy bandwidth of the ultrashort

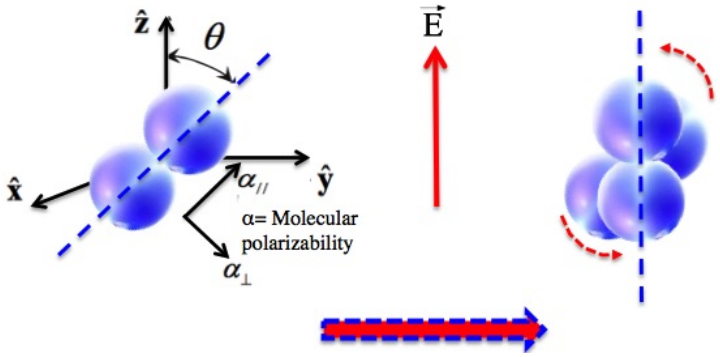

Figure 6.18: Schematic of molecular alignment induced by an intense laser field (Inspired by ref. [15]).

pulses [68].

In off resonant excitation of molecules with femtosecond pulses, both electronic and rotational degrees of freedom contribute to the nonlinearity as [68]:

$$\Delta n_{total}(t) = \Delta n_{instantaneous}(t) + \Delta n_{delayed}(t) \tag{6.3}$$

The instantaneous term is proportional to the intensity and includes both electronic and rotational Rayleigh contributions [68]:

$$\Delta n_{instantanous}(t) = n_{2,instant} I(t) \tag{6.4}$$

Where $n_{2,instant}$ is the electronic nonlinear index of refraction linked to the electronic levels of the molecules and $I(t)$ is the temporal profile of the pulse intensity at $z = 0$. The pure rotational Raman contribution is non-instantaneous:

$$\Delta n_{delayed}(t) = \int_{-\infty}^{\infty} R(t-\tau) I(t) d\tau \tag{6.5}$$

$R(t)$ is a function that accounts for the delayed response of the medium and is specific to molecular media (see Section 1.2.5).

6.2.1 Delayed rotational contribution to the nonlinear refractive index

The following is a background Section based on the thesis of Michael Spanner [15] Sections 2.1.1 - 2.1.4. In the presence of an electric field any non-spherical polarizable molecule will experience a torque due to the vectorial interaction between the electric field ($\vec{E}$) and the induced dipole moment ($\vec{p} = \vec{\alpha}.\vec{E}$). The potential energy assuming $\alpha_{\parallel} > \alpha_{\perp}$ (Fig. 6.18) can be written as

$$\begin{aligned} U(\theta) &= -\tfrac{1}{2}[\alpha_{\parallel} E^2 \cos^2\theta + \alpha_{\perp} E^2 \sin^2\theta] \\ &= -\tfrac{1}{2}\alpha_{\perp} E^2 - \tfrac{1}{2}\Delta\alpha E^2 \cos^2\theta] \end{aligned} \tag{6.6}$$

where $\alpha_{\parallel}$ and $\alpha_{\perp}$ are the parallel and perpendicular polarizability with respect to the dominant axis of the particle, θ is the angle between the the electric field $\vec{E}$ and the dominant axis of the molecule (Fig. 6.18) and $\Delta\alpha = \alpha_{\parallel} - \alpha_{\perp}$ is the polarizability anisotropy.

Interaction between polarized infrared laser pulses with molecular gases is the specific case of our interest. In the quantum picture, various molecules in the gas find themselves in a distribution of angular momentum states, $\mid J, M >$, following the Boltzmann distribution

$$P_J \sim (2J+1)\exp(-E_J/kT) \tag{6.7}$$

with J being the orbital momentum (J=0, 1, 2, ...), M the projection of the angular momentum onto the z-axis (M=-J, -(J-1),.....,J-1, J, and E_J the rotational energy of the state. In the case of diatomics, the nuclear spin statistics induces an alternation of population of the J levels with a $2:1$ (for

N_2) ratio as [194]

$$g_J = \begin{cases} 2, & \text{for even J} \\ 1, & \text{for even J} \end{cases} \tag{6.8}$$

The interaction of a linearly polarized laser pulse with a molecule is described by the Schrödinger equation [195]:

$$i\dot{\Psi}(\theta,\phi,t) = [B\mathbf{J}^2 - U_0(\cos^2\theta)]\Psi(\theta,\phi,t) \tag{6.9}$$

with θ being the angle between the laser polarization and the molecular axis, $B\mathbf{J^2}$ is the rotational energy operator, and $U_0(t)$ is the potential defined by Eq.6.6. Rovibrational (rotational- vibrational) coupling can be included by defining the $B\mathbf{J^2}$ operator as $B_0J(J+1) - D_0[J(J+1)]^2$ in the angular momentum basis [194]. The D_0 term accounts for bond deformation and only applies to high angular momentum cases. The field-free evolution of the wave packet, under the approximation that M levels don't couple and considering that all transitions (Raman transitions) occur between $J \longleftrightarrow J+2$ and $J \longleftrightarrow J-2$, becomes

$$\Psi(t) = \sum_J A_{J,M} e^{-iE_J t} \mid J, M > \tag{6.10}$$

where E_J is the eigen-energy $E_J = B_0J(J+1) - D_0[J(J+1)]^2$ [194].

Contribution of the degree of alignment

As it was shown earlier in Eq. 3.15, index of refraction change due to molecular alignment with interaction of a laser pulse is shown by

$$\Delta n_{delayed}(t) = \frac{N}{2n_0}\Delta\alpha[< \cos^2\theta(r,t) >_t - \frac{1}{3}] \tag{6.11}$$

with $\cos^2\theta$ being the standard measure of the degree of alignment of a rotational wave packet and given by

$$< \cos^2\theta >=< \Psi \mid \cos^2\theta \mid \Psi > \tag{6.12}$$

The $< \cos^2\theta > (t)_{J,M}$ value from each initial state $\mid J, M >$ weighed by the Boltzmann population can be incoherently averaged to obtain the alignment signal

$$P_J \sim g_J(2J+1)\exp(-E_J/kT) \tag{6.13}$$

to give

$$< \cos^2\theta > (t) = \frac{\sum_{J,M} g_J e^{-E_J/kT} < \cos^2\theta > (t)_{J,M}}{\sum_J P_J} \tag{6.14}$$

Short pulse alignment

Molecular alignment has been studied extensively for over two decades with a focus on non-adiabatic alignment, allowing field free alignment after the laser pulse is turned off [196, 197]. As explained earlier, the interaction of a short laser pulse (compared to the molecular rotational period) with the permanent or induced molecular dipole moment can excite a coherent rotationally broad wavepacket. Using Eq. 6.10 and neglecting the rotational-vibrational coupling (i.e $D_0 = 0$), the field-free evolution becomes

$$\Psi(t) = \sum_J A_J e^{-iB_0 J(J+1)t} \mid J, M > \tag{6.15}$$

substituting $t = \pi/B_0$ gives [15]:

$$\begin{aligned} \Psi(t = \pi/B_0) &= \textstyle\sum_J A_J e^{-iB_0 J(J+1)(\pi/B_0)} \mid J, M > \\ &= \textstyle\sum_J A_J e^{-iJ(J+1)\pi} \mid J, M > \\ &= \textstyle\sum_J A_J \mid J, M >= \Psi(t = 0) \end{aligned} \tag{6.16}$$

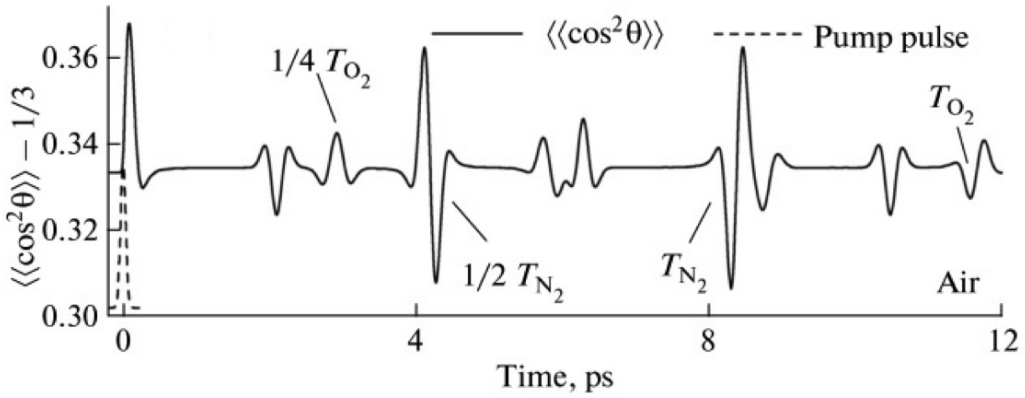

Figure 6.19: "The simulated degree of molecular alignment $<< \cos^2\theta >>$ of the N_2 and O_2 molecules in air as a function of time delay. The black dashed curve stands for the envelope of the pump pulse" [16].

Meaning, after a period $T_{rev} = \pi/B_0$, the wave function will exactly reproduce the wave function at $t = 0$ [198, 199], when the alignment is maximum.

The revival periods for molecular N_2 and O_2 are shown in Fig. 6.19 [16] showing strong alignment at points of fractional revival times of $t = T_{rev}/4, T_{rev}/2$, and $3T_{rev}/4$.

The different population of the even and odd states in the initial distribution lead to the difference in amplitudes of the full and fractional revivals. It was shown that the odd distribution has maxima with $T_{rev}/4$, $3T_{rev}/4$, $5T_{rev}/4$,... revivals, when the even distribution has minima, and vice-versa. The minima and maxima of the even and odd distributions coincide for the $T_{rev}/2$, T_{rev}, $3T_{rev}/2$,... revivals. As a consequence when the average of these two signals (considering the weight factor g_J) is calculated, half the alignment peaks partially cancel out and the other half add constructively [15].

The beat frequencies for two levels J and $J \pm 2$, (for Raman population of the

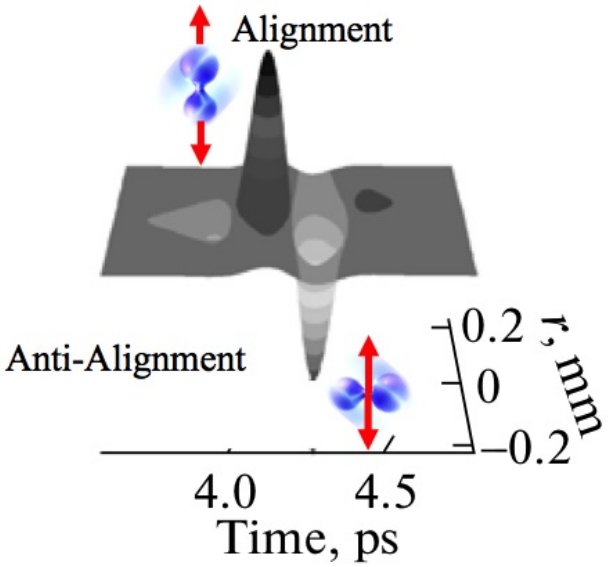

Figure 6.20: Spatiotemporal profile of the index of refraction change induced by field free molecular alignment at the half revival time of N_2 (from ref. [16]).

rotational levels (ΔJ=2)), $\omega_J = E_{J+2} - E_J$, with energies of $E_J = B_0 J(J+1)$, contained in the alignment signal become

$$\omega_J = B_0(4J + 6) \tag{6.17}$$

which would be seen in the Fourier transform of the temporal alignment signal.

6.2.2 Using a probe pulse to measure the effect of molecular alignment

Fig. 6.20 shows a numerical simulation of the alignment-induced refractive index change by a Gaussian shaped femtosecond pulse for room temperature air at the half-revival time of molecular N_2 [16]. The refractive index

change on the beam axis is larger than that at its periphery due to the larger molecular alignment degree. The parallel and perpendicular molecular alignments with increased and decreased refractive index change then account for additional effects of cross-focusing (positive lens) and cross-defocusing (negative lens), respectively. Such a cross-defocusing effect has been used to analyze the field-free molecular alignment [200] by measuring the molecular alignment induced diffraction of a probe pulse. Time dependent revival of the molecular alignment adds a nonlinear phase shift, ϕ_{mol}, to a properly matched ultrashort probe pulse corresponding to a spectral phase modulation given by $\delta\omega_{mol}(t) = -\partial\phi_{mol}/\partial t \sim -\delta n_{mol}(t)/t$ [16]. Hence, the increase and decrease of the molecular alignment revival account for red and blue shifts of the properly matched ultrashort laser pulse, respectively. This controllable spectral modulation of a time delayed femtosecond laser pulse propagating in pre-aligned molecules was demonstrated in [201], where additional red and blue shifted frequencies were generated when its time delay was tuned to match the rising and falling edges of the molecular alignment revival.

The importance of the laser-molecule interaction that take place in the filament, in addition to the laser-induced emission of neutral and ionic nitrogen molecules (see Section 5.1.2) lead to using the filament for probing the laser-molecule interaction. In this section the effect of field free molecular alignment on the plasma emission in N_2 excited by a short Ti-Sapphire laser pulse is studied. The fluorescence of the first negative band system ($B^2\Sigma_u^+ \rightarrow X^2\Sigma_g^+$) ($\nu = 0$ - $\nu = 1$) at 427.5 nm) transition is measured using the pump-probe technique, versus the delay between the pump (800 nm) and the second harmonic probe pulses (400nm). This work is a continuation of

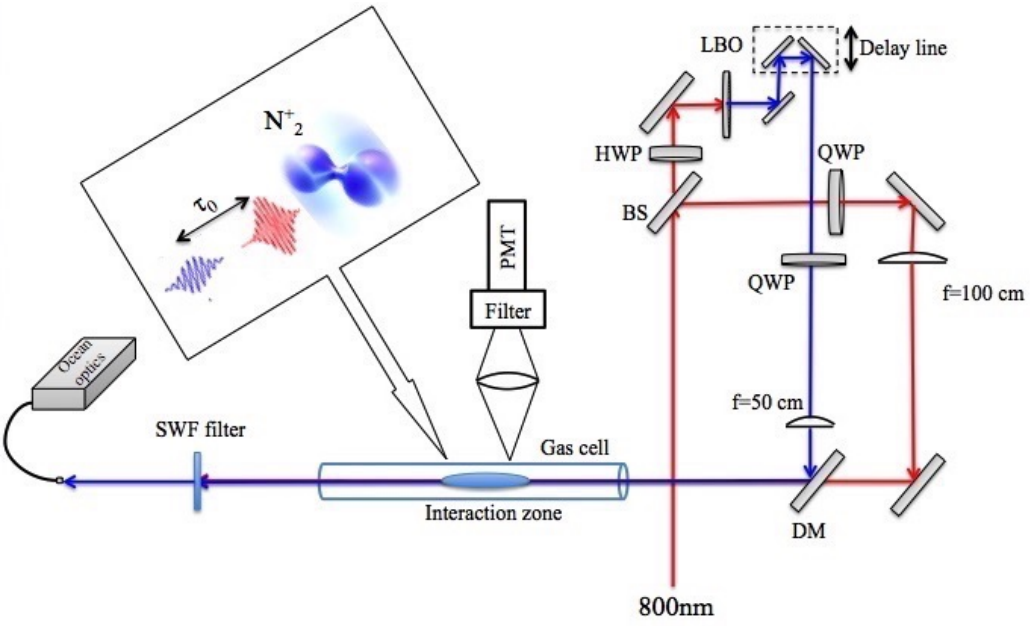

Figure 6.21: Schematic of the experimental setup (see the text for details).

the work started by Amin Rasoulof in Dr. Diels's research group.

6.3 Experiment and discussion

In these experiments, an intense femtosecond (65fs) laser pulse at 800 nm and 1kHz repetition rate, serves as the pump for excitation of the molecular system. The laser beam is divided into two arms using a beam splitter (BS-70% reflection). Reflection is used as the pump beam and transmission goes through a 0.1 mm-thickness LBO (lithium triborate) crystal to create the second harmonic probe pulse at 400 nm which can be delayed (τ_0) after the 800 nm pump pulse (Fig. 6.21). The delay between pump and probe is controlled using a translation stage (M-014.D01 linear slide in combination

with C-86 MercuryTM servo motor controller) in the 400nm arm, that could be moved systematically with 0.1μm resolution, using Lab-view interface. Polarization of the pump and probe could be controlled independently with zero order quarter wave plates in each arm. Since in the type I LBO crystal, the maximum generated second harmonic has a polarization perpendicular to the polarization of the pump pulse, a half wave plate (HWP) is used to rotate the pump polarization by 90° before the SHG crystal to get parallel polarizations for the pump and probe. The pump and probe pulses have energy of $\approx 780\mu J$ and $\approx 4\mu J$, respectively. It was confirmed that the probe pulses alone cannot generate the emissions at 428 nm. A dichroic mirror (DM) with high reflectivity at 400nm and high transmission at 800nm is used to combine the pump and probe pulses. The pump and probe pulses are co-linearly focused with a 100 cm (800nm) and 50cm (400nm) focal length lenses into a gas cell filled with 17 psi of nitrogen gas to generate a filament.

After propagation in the gas cell, the 400 nm probe is sent to a fiber spectrometer (Ocean Optics HR 2000 CG-UV-NIR) to monitor the spectral change and the 800 nm is blocked using a short pass filter (SWF). Temporal overlap of 800nm and 400nm pulses (zero delay) was done through measuring their sum frequency generation signal at 266nm, using a KDP (monopotassium phosphate) crystal.

The fluorescence signal was collected sideways, using a lens (f= 3.5cm) and PMT, for different pump-probe delays (τ_0). An interference filter at 420 nm with 10 nm bandwidth was used for measuring the emission from N_2^+ ($B^2\Sigma_u^+ \rightarrow X^2\Sigma_g^+$ transition) at 428nm. The output signal of the PMT was connected to an oscilloscope (Tektronix, TDS1012B- 100MHz) and averaged

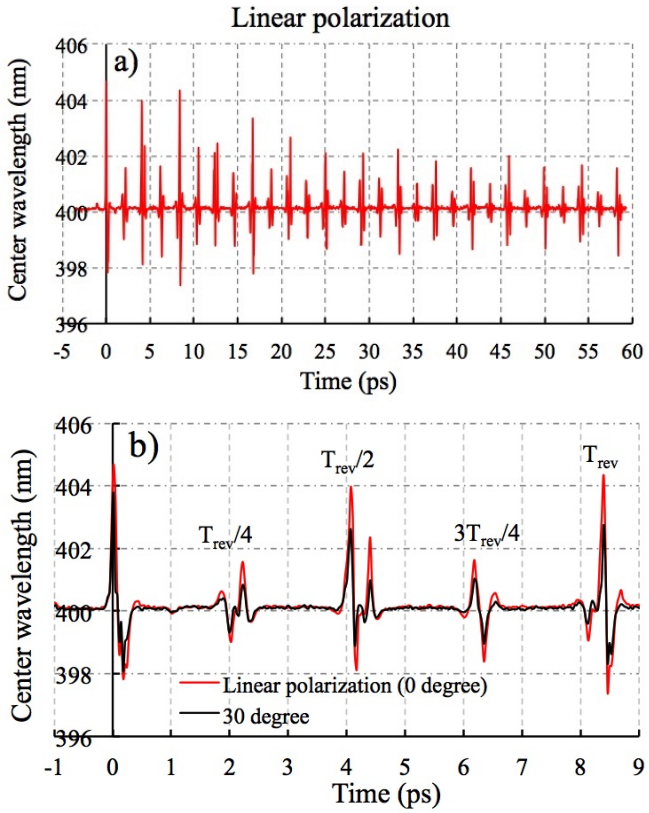

Figure 6.22: Spectral broadening of the 400 pump, observed at fraction revivals of N_2 for a) linearly polarized pump and probe b) (zoomed in) for linear pump and probe (red) and pump and probe when the angles of both quarter wave plates are at 30 degree (black).

over 200 shots.

As explained in Section 3.1 the index of refraction change due to the molecular alignment induced by the pump causes the probe to be spatially confined in the center of the wake.

Equation 6.11 implies that a probe pulse (same polarization as the pump) propagating in the wake of the filament at suitable time delays, will spectrally broaden at a maximum or a minimum of a fractional revival [202].

This spectral modulation is monitored to insure the perfect alignment in the experiments. Fig. 6.22a shows the change in the central wavelength of the probe spectrum (polarization parallel to the pump) for different delays after the pump. The positive delay indicates that the probe pulses are behind the pump pulses in time.

Fig. 6.22b indicates that the polarization changing from linear to elliptical, decreases the spectral broadening of the probe which is directly related to experiencing less change in the refractive index due to alignment of N_2 molecules induced by the pump.

The delay time dependance of the fluorescence signal for linearly polarized pump and probe, is shown in Fig. 6.23a. The large signal at zero time delay, could partially be related to two-color ionization [203].

At least 11 photons are required to ionize nitrogen molecules with 800nm photons. There is an enhancement of the fluorescence signal at 428nm (emission from excited ions), since two pump photons could be replaced with one probe photon. In some cases two peaks have been detected at zero delay with 100fs delay with respect to each other [204]. The first peak being from instantaneous two color ionization and the second peak from the interaction of the probe pulses's with aligned molecules. A delay in the order of 100 fs between the excitation time and the instance of maximum alignment was observed by Azarm et al. [204]. It was also found that N_2 molecules aligned parallel to the laser polarization are approximately four times more likely to be ionized than when perpendicularly aligned in the intensity range of $1.5 \times 10^{14} W cm^{-2}$ [205].

Periodic enhancement is observed in the 428nm signal as the probe is delayed

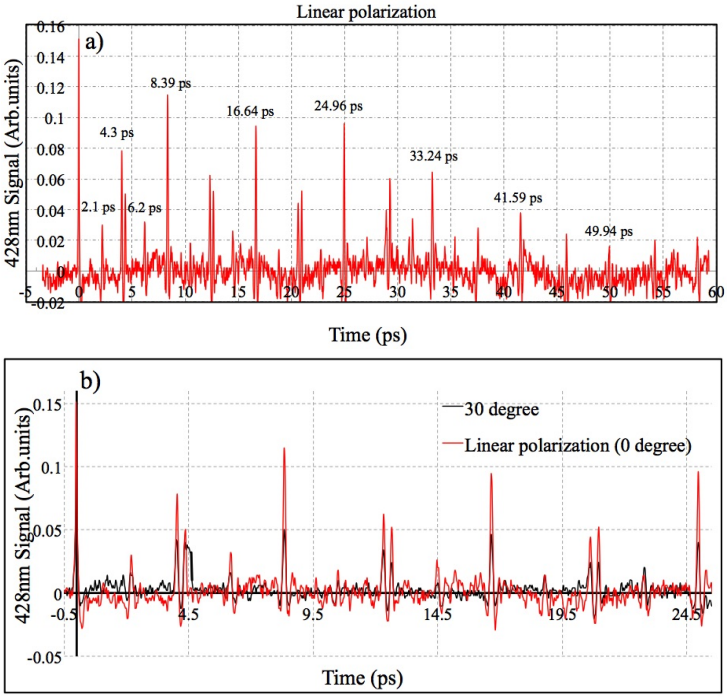

Figure 6.23: Fluorescence signal of a) linearly polarized pump/probe for different time delays of the probe with respect to the pump b) with QWP angle for both pump and probe at 30 degrees compare to the linear case. Ionization enhancement is clearly seen at fraction of revivals (T_{rev}=8.38 ps) for N_2.

with respect to the pump. The first peak is at a delay of about 2.1 picoseconds which corresponds to $T_{rev}/4$ for nitrogen (T_{rev}=8.38 ps). Azarm et al., found the origin of this periodic enhancement to be the population trapping of nitrogen molecules in highly excited states [204].

To reduce the noise in 428nm side measurements, a polarizer was put in front of the PMT, perpendicular to the polarization of the probe, to block the scattered polarized 400nm. The result shows a much cleaner signal up to 60 picosecond delay between the probe and pump (Fig. 6.24). The polarizer

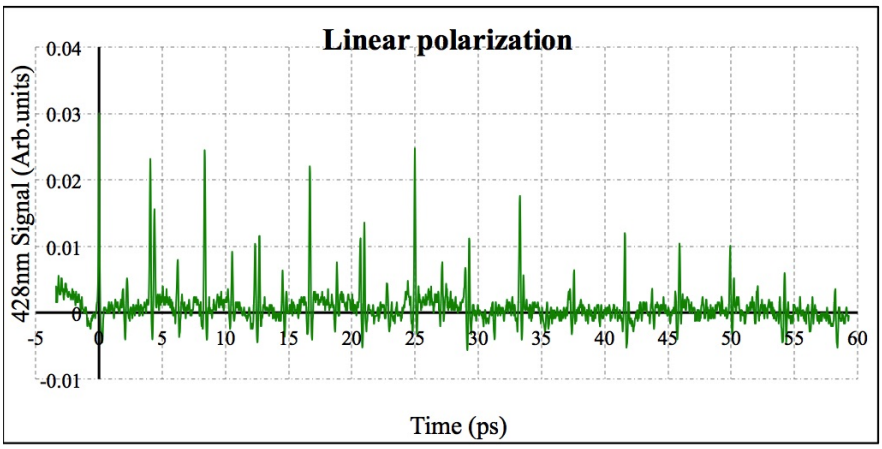

Figure 6.24: Fluorescence signal of linearly polarized pump/probe for different time delays of the probe with respect to the pump. A polarizer was used in front of the PMT to block the scattered 400nm.

also reduces the amplitude of the 428nm which could be due to having a large polarization component in the same direction as the pump and probe. Linearly polarized pump pulse (800nm) aligns the neutral molecules at full and fractional revivals. The trapped molecules in the highly excited electronic states will ionize by the probe pulse through one or two photon absorption which is more probable by aligned molecules. Ionization is also enhanced when the molecules are aligned parallel to the polarization of the laser pulses. This enhancement falls on the periodic revival times leading to fluorescence enhancement of the first negative band at 428 nm.

The Fourier transform of the measured 428nm signal (Fig. 6.25), reveals set of discrete frequencies. Furthermore, the alternate intensity of the peaks between the beat frequencies arising from even states ($\omega_{even}/B_0 = 6, 14, 22, 30, ...$) and odd states ($\omega_{odd}/B_0 = 10, 18, 26, 34, ...$) can be seen due to the nuclear

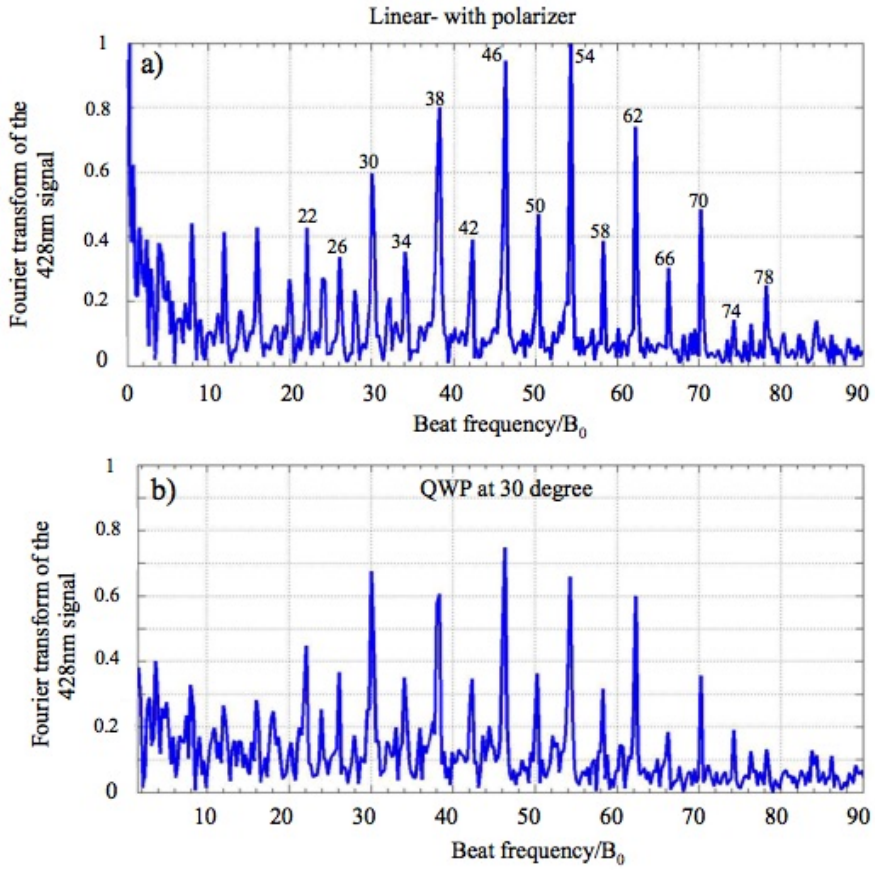

Figure 6.25: Frequency spectrum of the time dependent 428nm signal shown in a) Fig. 6.24 (linear polarization) and b) 6.22b (QWP angle at 30°. The peaks are numbered with the frequency (4J+6) in the unit of B_0.

spin statistics term (See Eq. 6.8). The strong peak near $\omega = 0$ is due to the DC part of the alignment signal.

In order to investigate the effect of "magic angle", initial polarization that changes to more linear and create spectral broadening enhancement (see Section 5.5), in Raman transitions, the same measurements were repeated at QWP angle 39°. Figure 6.26 presents the Fourier transform of the 428nm

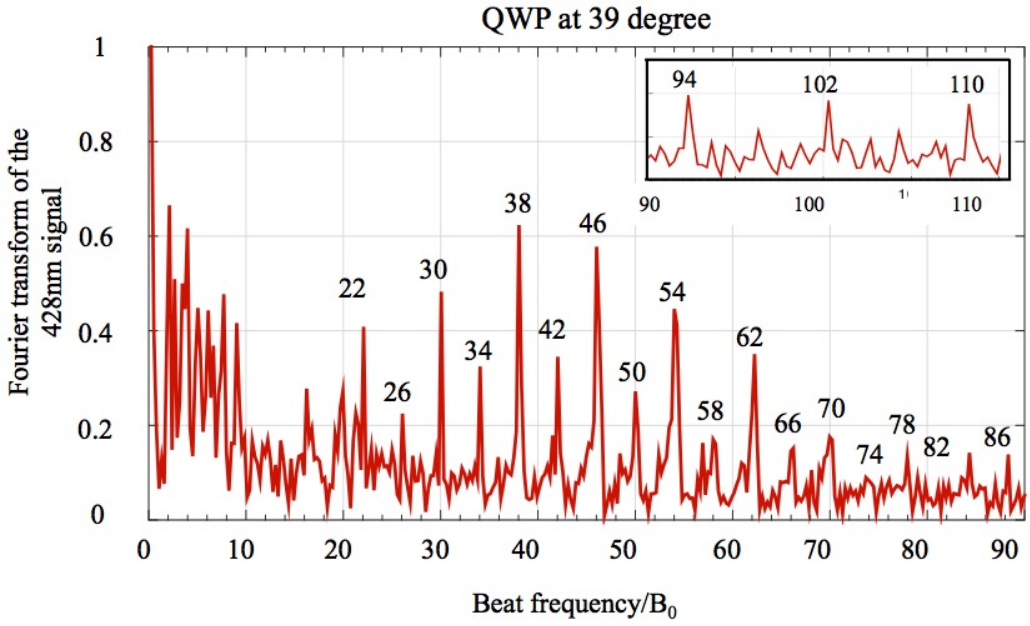

Figure 6.26: Fourier-transform of the time dependent 428nm signal with QWP angle at 39°. The peaks are numbered with the frequency (4J+6) in the unit of B_0. The inset is zoomed in on the higher frequency region.

signal when the QWP for both pump and probe are at 39° and indicates excitation of higher rotational states.

6.4 Ultrafast characterization of the plasma emission

In these measurements a Streak camera that provides one spatial dimension and one temporal scan with picosecond resolution simultaneously, was used. Since several nonlinear process play a role along the filament propagation, tight focusing plasma imaging will not be able to capture the real picture of

the process. On the other hand measurement of attenuated light after the filament presents only an integrated effect. Therefore performing a measurement which would provide real time information of the propagating radiation intensity versus space, time and wavelength is of great interest. The technique to visualize the propagation of filaments and the induced plasma in time and space presented here was derived in an earlier work, where videos of repetitive events at megapixel spatial resolution and picosecond time resolution have been recorded using a combination of a streak camera detector and a scanning technique [206]. In this section, consecutive frames of the propagation of filaments and their accompanied radiation at different wavelengths in air, are presented. Data processing was done by Andreas Velten and experiments were performed in collaboration with the Air Force Research Laboratory [17].

6.4.1 Experimental setup

Laser pulses from a commercial Coherent HIDRA laser were used to create the filament (see Section 2.1.1). Laser beams with initial diameter of 20mm, pulse energy of 10 mJ, 60fs pulse width (close to bandwidth limited), repetition rate of 10 Hz were used for these experiments.

In Fig. 6.27, the slit of the streak camera (Optronis SC-10), is located at the image plane of the filament and parallel to its propagation axis z. Fig. 6.28 shows an example of one image of the streak camera displaying the light intensity (collected along the slit) versus space and time. The field of view is continuously scanned by rotating one of the UV enhanced mirrors along y at a small enough rate to keep continuity of the images. The individual im-

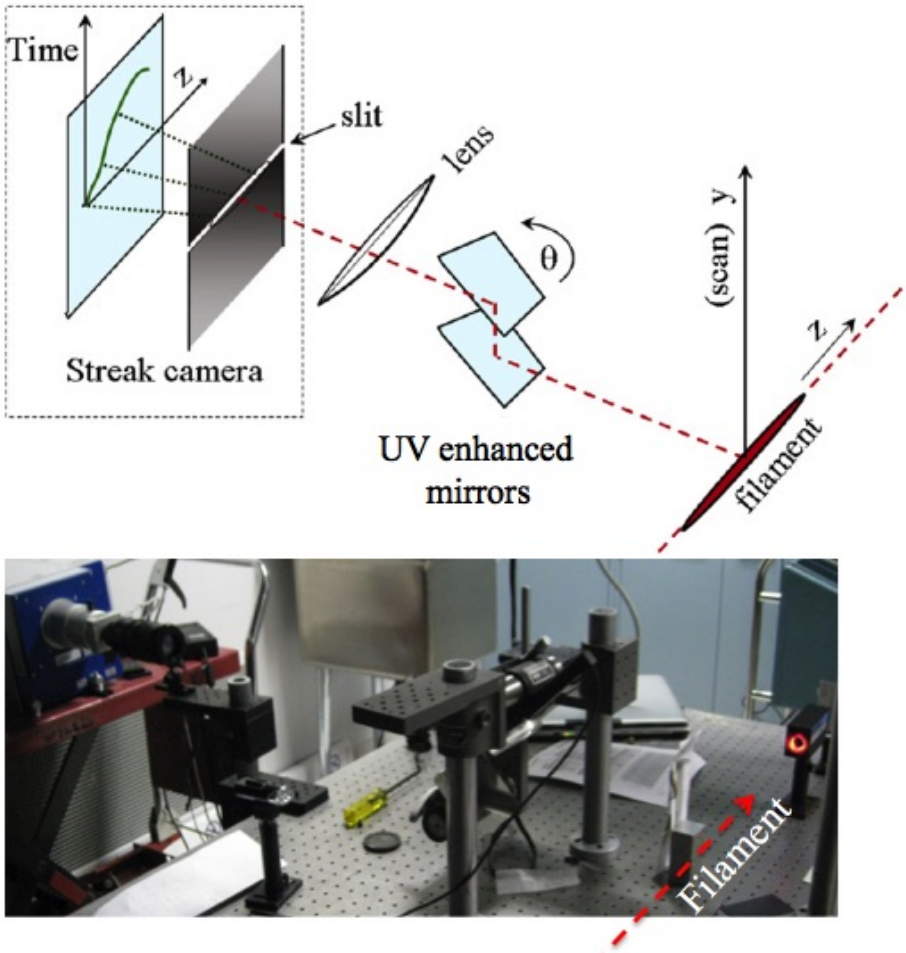

Figure 6.27: Experimental setup for time and space visualization of the filament through plasma emission. One of the UV enhanced mirrors in the periscope, is scanned over 6 mrad (θ) and 200 or 1000 images are recorded in 200 s or 1000 s time frame.

ages are then computationally organized in successive time steps to provide a video.

One image of the filament as a horizontal line is taken per second and the vertical field of view is scanned over 200s. These images then can be stitched together to generate a video of the filament. To calibrate the resolution of the

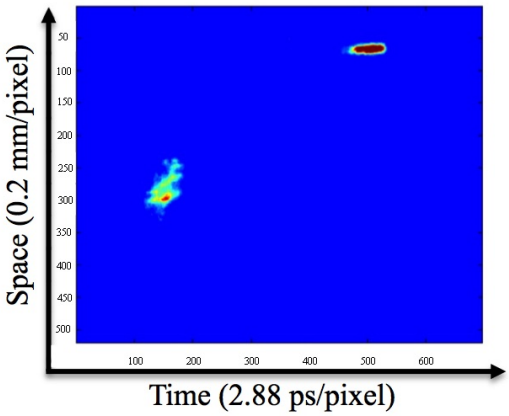

Figure 6.28: The calibration spot on the top right, used for jitter correction, and a portion of the filament on the lower left can be seen in an example of a streak camera image [17].

reconstructed images and verify image quality, images of a ruler illuminated by continuous white light are captured and reconstructed (Fig. 6.29).

In the case of a low numerical aperture focusing (loose focusing with a 3m focal length lens) the signal can be improved by increasing the gain of the camera in addition to lowering the scanning speed and averaging over

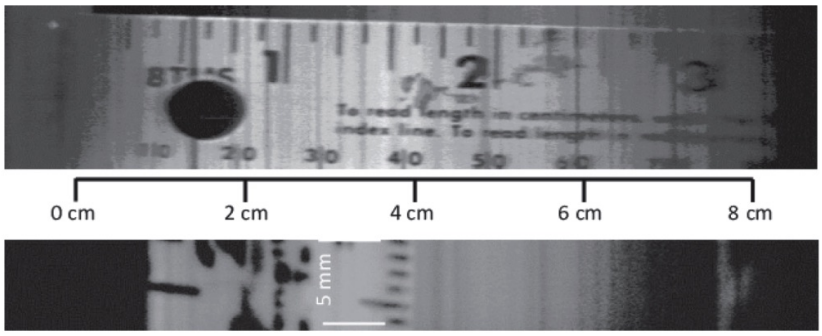

Figure 6.29: Top image shows a horizontally placed ruler along the slit of the camera. Bottom image shows one frame of the ruler placed vertically [17].

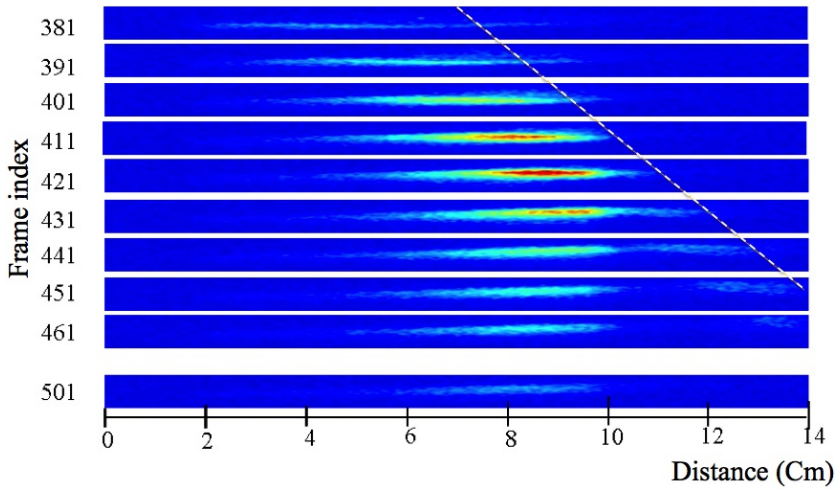

Figure 6.30: Unfiltered detection of a 800 nm filament created with tight focusing in air. Each frame with the index shown on the left, has a height of 5mm and is separated by 3 ps. The white line indicates the speed of light [17].

consecutive images.

All the captured frames need to be accurately synchronized in order to be able to take advantage of the picosecond resolution of the camera. The master clock of the laser system (SDG (See section2.1.1)) is used to trigger the streak camera. For each pulse creating the filament, a reference beam is selected from the same pulse and sent directly to the camera providing a temporal reference for each image. This reference can be used to correct the jitter caused by the laser electronics (2 ns) in the trigging process as well as providing the timing of the event.

6.5 Experimental results and discussion

6.5.1 Focusing in air

First experiment was performed by focusing the beam in air with a short focal length lens (60 cm). Tight focusing helps to create a filament with a bright induced plasma defining its onset. Selected frames (10 frames interval $\approx$ 30 ps) of an unfiltered detection are shown in Fig. 6.30, with the white line indicating the speed of light.

The bright plasma that is created in the first frames seems to divide into two entities (frame 431 in Fig. 6.30). The portion with the strong radiation stays in place and the other one follows the speed of light. This fixed plasma radiation created at the focal spot is from N_2^+ ion, since it seems to be equally bright with a 391 nm interference filter. The emission moving at the speed of light is greatly attenuated with 391nm and 800 nm filters indicating that it's most likely due to the scattered radiation of the supercontinuum. The presence of the plasma emission in the last frame taken 360 ps after the first one refers to its long lifetime which is consistent with previous results reported by various groups. These studies range from fluorescence measurements (10 ns FWHM of the integrated fluorescence intensity [91]) to measurements of the resistivity (3 ns rise and fall time [31], or 5.5 ns from [207]) to measurements of microwave absorption (fall time <3ns from [208]).

Fig. 6.31(b) shows a rise time of 90 ps and a fall time of 200 ps for the plasma which is consistent with measurements of the plasma emission from a bunch of ten filaments reported by Schmitt-Sody et al. [209]. To extract these informations, a plot of radiated intensity versus time was generated by

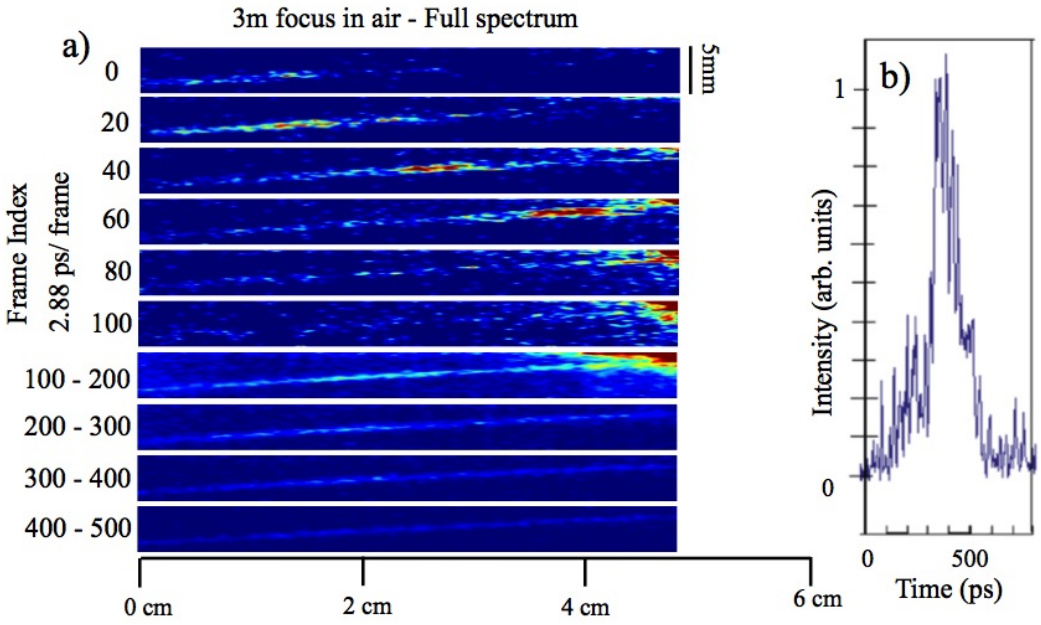

Figure 6.31: (a) Unfiltered detection of a 800 nm filament, created from a 3m focus in air. Selected frames (separated by 2.88 ps) are shown between frame 1 and 100. An average over 100 frames is shown to reduce noise in the rest of the frames. (b) The averaged Intensity over 50×50 pixels around the position z = 2 cm, versus time [17].

averaging the intensity over a 50 pixel by 50 pixel region around the middle of the filamentation region. The selected region corresponds to the position $z = 2$ cm in Fig. 6.31(a) which presents the selected frames taken of a 800 nm filament created from a 3m focus in air.

6.5.2 Focusing in vacuum

The jitter along z in the experiments makes it hard to define the onset of the filament accurately, in addition the observed emission may not be representative of the true length of the plasma. To ensure the reproducibility

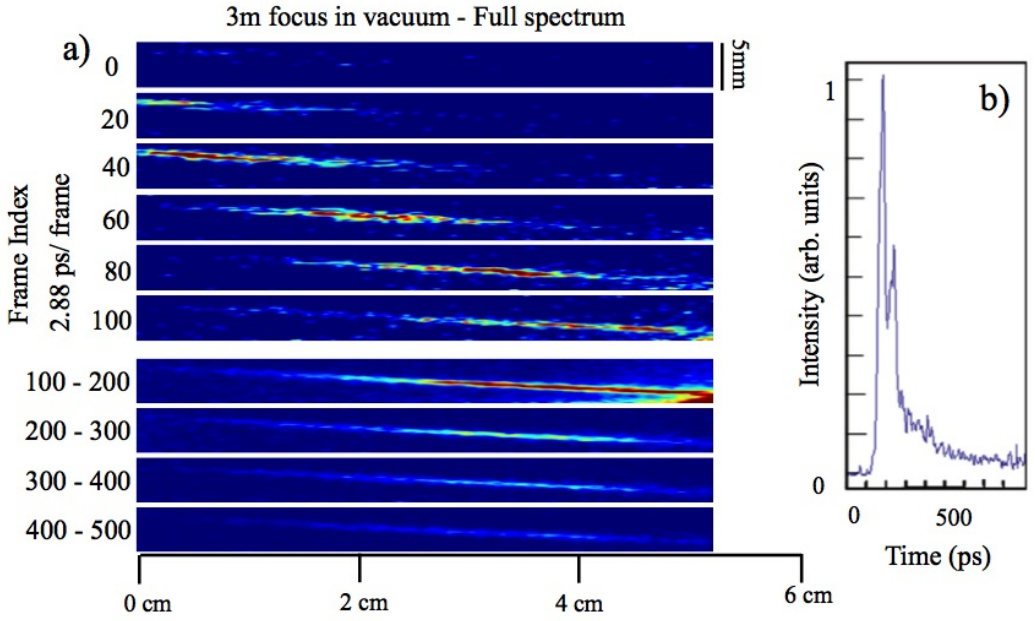

Figure 6.32: a) Unfiltered detection of a 800 nm filament, created from a 3m focus in vacuum through an aerodynamic window. Selected frames are presented from frame 1 to 100. An average over 100 frames is shown to reduce noise in the rest of the frames. (b) The averaged Intensity over 50×50 pixels around the position z = 2 cm, versus time [17].

of the starting point of the filaments in air, the laser pulses are prepared in vacuum and focused into the 2 mm vacuum-atmosphere transition region of an aerodynamic window (See section 2.1.3). In this configuration the filament starts at the same point, exit of the aerodynamic window, from shot to shot. Fig. 6.32(a) presents the selected frames of a filament created from a focus in vacuum showing a shorter (along z) and brighter emission. The reduced jitter enables a much better resolution of the 40 ps rise time and 230 ps fall time (both being measured from 10% to 90%) as seen in Fig. 6.32(b).

"The transverse dimension of the plasma appears to be smaller, that could

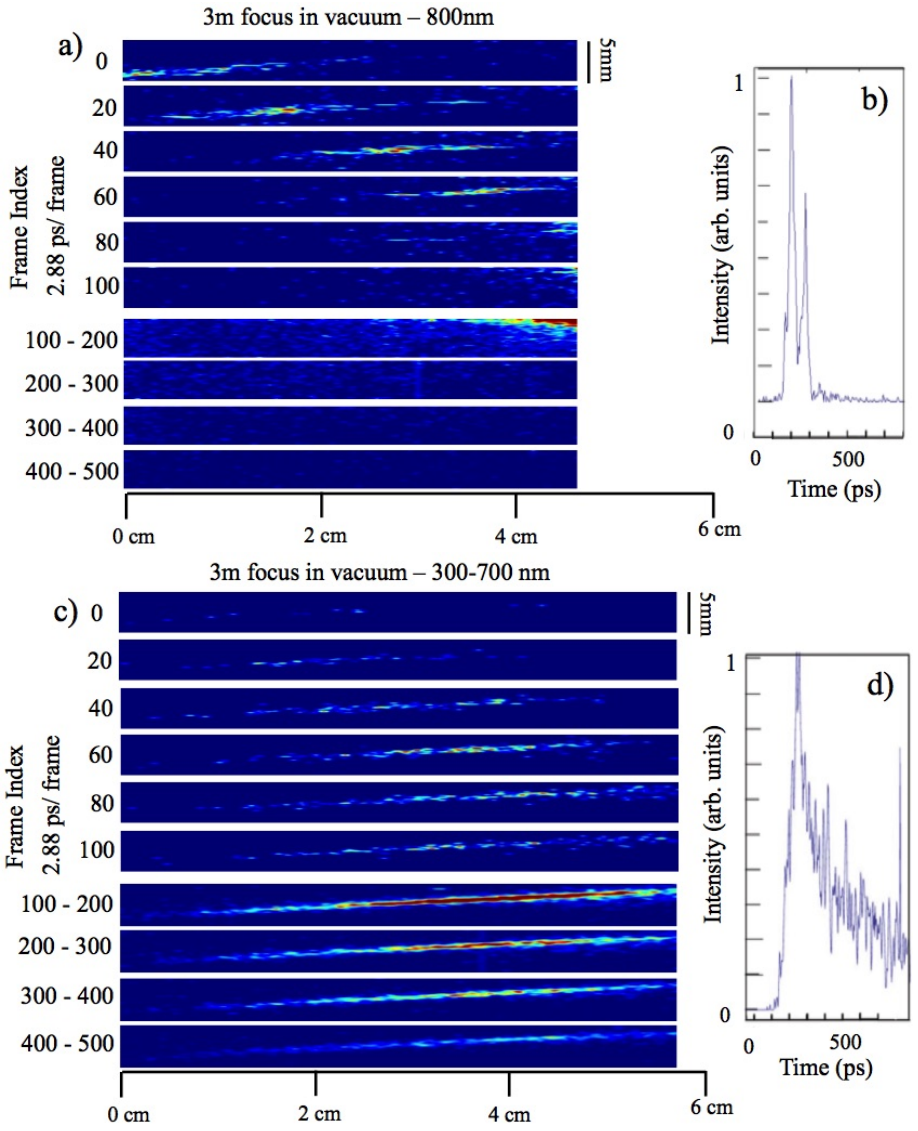

Figure 6.33: Fitered detection of a 800 nm filament, created from a 3m focus in vacuum through an aerodynamic window. (a), (b) detection at 800 nm, (c), (d) 300-700 nm detection. Selected frames are presented from frame 1 to 100. An average over 100 frames is shown to reduce noise in the rest of the frames. The Rayleigh scattering peak, followed by fluorescence radiation is seen in (b) [17].

also be due to the spacial stability of shot to shot images when the light is prepared in vacuum" [17].

By placing interference filters in front of the streak camera we can acquire a fourth dimension, wavelength. Filtered detection of the emission from the filament can separate the Rayleigh scattering at 800 nm from the broadband plasma emission at shorter wavelengths (Fig. 6.33(a)). The delay between 800 nm Rayleigh scattering of the pulse and some plasma radiation (wavelength not identified) can be clearly seen in the time scan in Fig. 6.33(b). Figure 6.33 c&d present the radiation from the filament in the region between 300 nm and 700 nm (using a bandpass filter).

As presented in [17], from Fig. 6.33 it can be interpreted that, "following ionization by the filamented pulse, collision between nitrogen molecules and ions lead to the formation of $N_4^+(N_2^+ + N_2)$. The N_4^+ upon collision with electrons produces neutral nitrogen in the $C^3\Pi_u$ state fluorescing at 337.1, 357.7 and 380.5 nm ($N_4^+ + e \rightarrow N_2(C^3\Pi_u) + N^2$[210]. Measured decay time of approximately 70 ps, is in agreement with the decay time measured by Xu et al. [142]. The delay between the two peaks of Fig. 6.32 and 6.33 is only at most 80 ps, less than the 130 ps cited for the collision time of nitrogen in [142]". The brightness of the images can be enhanced, using water droplets to increase scattering. The droplets of 1-5 μm diameter (small enough to not create any local illumination) produced with a nebulizer (based on Bernoulli principle) were blown through the field of view in the opposite direction of the filament propagation. Fig. 6.34(a) shows the selected frames of these measurements where a short lived pulse propagating from left to right, interpreted as Rayleigh scattering from the laser pulse.

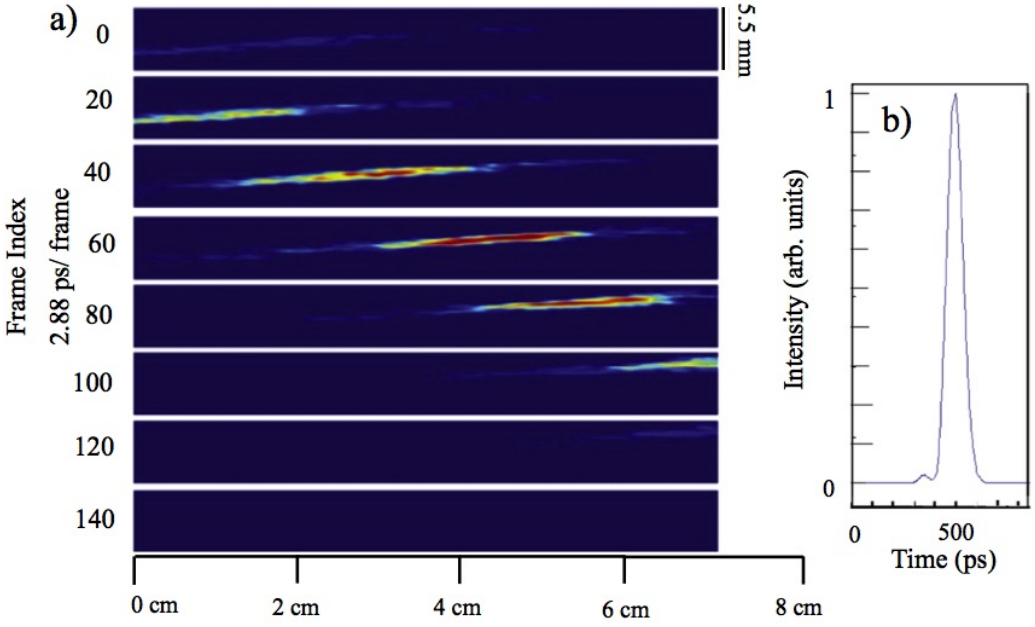

Figure 6.34: Portion of the filament created at the transition between vacuum and air, propagating through micron sized water droplets [17].

6.5.3 Conclusion

This chapter was focused on plasma radiation from filaments, prepared with different initial conditions and different techniques to investigate and characterize it. Measurement from nitrogen molecule at 337nm for filaments with angular momentum, is observed for a shorter distance with less difference between linear and circular polarizations, comparing to conventional (m=0) filaments. Introducing the angular momentum lead to elimination of the mid region wavelengths (≈550-750nm) for air filaments. Studying vortex filaments prepared in vacuum, showed that propagation in nonlinear medium before the filament starts, is necessary to counteract their azimuthal instability.

Donut shaped filaments break into 2 individual ones (depending on the initial energy) with complimentary spectral components. It was shown that the blue shifted wavelengths go through different (more) polarization modifications (both ellipticity and angle) compare to the original spectral components of the beam.

Significant spectral broadening of time-delayed probe pulses in the filament wake at maxima of rotational revivals, induced by the delayed Raman response of nitrogen, was demonstrated. Periodic enhancement of the fluorescence from the excited nitrogen in the plasma channel induced by a 800nm filament in nitrogen is observed. The period corresponds to the full and fractional revivals of the aligned nitrogen molecular wavepacket. It was also shown that the polarization of the pump affects the alignment of nitrogen molecules, through measuring the 428nm side emission of the plasma, with lower degree of alignment when the polarization is more elliptical. Higher rotational states could be excited at a specific polarization (same polarization that creates super continuum enhancement) of the pump.

A novel technique to visualize the filament through plasma radiation in time and space using a streak camera was presented. In this method a large field of view (10 cm by 1 cm in our study, but dependent on the imaging system) can be captured. Each frame is an integrated 2D image but 3D information can be recovered using Abel inversion, assuming cylindrical symmetry.

Another dimension to the image is spectral selectivity. Narrow band-filters centered at different emission lines of the ions of interest would enable the dynamic study of processes such as multi-photon ionization, dissociation, excitation decay, fluorescence, as well as the plasma evolution in a secondary

electric field.

The dynamics of the plasma properties (length, speed and lifetime) for various focusing geometries were visualized. These encouraging first results confirm that the use of the aerodynamic window, to avoid nonlinear effects during the preparation phase of the filament, provides very stable filaments. This new approach to ultrafast imaging of filaments can be considered a very valuable tool in the study of nonlinear laser propagation.

Chapter 7

Conclusion

This thesis has focused on a new dimension in laser filamentation: POLARIZATION. While the large majority of the studies on filamentation have used linear polarization, there is a growing interest in exploring the polarization dimension. This interest is linked to the growing understanding of the molecular aspect of the propagation medium during laser filamentation in the last decade.

This thesis has revealed new understandings in the laser filamentation science with respect to the effect of polarization. In parallel, new characterization tools and protocols have been developed for measuring the filament ellipticity and the medium response to such general elliptical polarization.

It was shown that the nonlinear ellipse rotation could be used as an accurate way to measure the nonlinear index of refraction in different materials as well as the filament intensity. Experimental results and theoretical calculations were presented for different samples. Using this method to measure the intensity in the filament lead to a higher value $4 \times 10^{14}\mathrm{W/cm^2}$ than the

reported intensity clamping, 5×10^{13}W/cm^2. In addition, the plasma radiation from filaments was also used as a tool for characterizing their dynamics, comparing both the neutral and singly ionized molecular nitrogen emission (337 nm and 420 nm, respectively).

The physics of polarization evolution of nonlinear laser propagation, involving electronic Kerr nonlinearity, molecular orientation and electron plasma was studied. This study showed that changes in ellipticity involve energy exchanges related to conical emission and molecular alignment while the polarization angle rotation with propagation, can be a measure of the intensity. An important aspect of the polarization physics of filamentation was to determine the influence of the nonlinear focusing by either preparing the filaments in air (Kerr self-focusing) or in vacuum (linear focusing). It was shown that the polarization change seen after preparation in the nonlinear medium (air) and propagation of the filament, is associated to the periphery of the beam since most of the energy is contained in the reservoir. Ellipticity measurements didn't show any noticeable changes when the beam was focused in vacuum.

Measurements of different spectral regions of the center and side of the beam, showed that blue shifted wavelengths generated during the filament propagation, have different ellipticity than the initial spectral components. Measuring the orientation of the ellipse also confirmed that the blue shifted light goes through more rotation.

Anomalous spectral broadening behavior for filamenting pulses with specific initial polarization ellipticity near circular polarization was studied. This anomalous behavior is only observed in molecular gases, and leads to a de-

crease in the final ellipticity of the beam as well as an increase in the length of the filament. Both experimental and simulated results clearly demonstrate the strong dependence of filamentation on the input laser ellipticity via the delayed rotational response of the molecular medium. This study introduces an additional tool, polarization ellipticity, to control SCG and enhance the white light spectrum. Polarization control may therefore be an important addition to applications of filamentation where the generation of supercontinuum is a key consideration, such as white light LIDAR and the generation of few-cycle pulses.

In addition to the effect of polarization, the effect of the orbital angular momentum of the beam undergoing filamentation was studied. Side emission from the plasma of vortex filaments was observed for a shorter distance with less difference between linear and circular polarizations, compared to conventional (m=0) filaments. Introducing the angular momentum lead to the suppression of the spectral range between 550 and 750nm for air filaments. Studying vortex filaments prepared in vacuum, showed that propagation in nonlinear medium before the filament starts, is necessary to counteract their azimuthal instability.

Donut shaped filaments broke into 2 individual ones (depending on the initial energy) with complimentary spectral components. It was shown that the blue shifted wavelengths go through different (more) polarization modifications (both ellipticity and angle) compare to the original spectral components of the beam.

The revival of the Raman response of nitrogen in the wake of a light filament was studied as well and showed it can create significant spectral broadening

of time delayed probe pulses in the filament wake at maxima of rotational revivals. The period corresponds to the periodic revival of the aligned nitrogen molecular wavepacket. It was also shown that the polarization of the pump affects the alignment of nitrogen molecules, through measuring the 428nm side emission of the plasma, with lower degree of alignment when the polarization is more elliptical. Higher rotational states could be excited at a specific polarization (same polarization that creates supercontinuum enhancement) of the pump.

A novel technique to visualize the filament through plasma radiation in time and space using a streak camera was presented. In this method a large field of view (10 cm by 1 cm in our study, but dependent on the imaging system) can be captured. Each frame is an integrated 2D image but 3D information can be recovered using Abel inversion, assuming cylindrical symmetry.

Another dimension to the image is spectral selectivity. Narrow band-filters centered at different emission lines of the ions of interest would enable the dynamic study of processes such as multi-photon ionization, dissociation, excitation decay, fluorescence, as well as the plasma evolution in a secondary electric field.

The dynamics of the plasma properties (length, speed and lifetime) for various focusing geometries were visualized. These encouraging first results confirm that the use of the aerodynamic window, to avoid nonlinear effects during the preparation phase of the filament, provides very stable filaments. This new approach to ultrafast imaging of filaments can be considered a very valuable tool in the study of nonlinear laser propagation.

As just demonstrated, this thesis has explored many aspects of the polar-

ization physics of the laser filament by measuring its intrinsic parameters (intensity, spectrum, spatial extension) as well as its dynamics followed by the plasma emission. Most importantly, this work is believed to be the basis for a new field in filamentation physics. Unconventional dimensions were explored: the ELLIPTICITY and the ORBITAL ANGULAR MOMENTUM of the laser pulse. Many findings should be applied to these more general pulses. For instance, the determination of the nonlinear index of materials using the ellipse rotation should be extended to more complex polarization conditions such as vortices, radially polarized and azimuthal polarized beams.

Even if largely studied, another dimension of interest is the spectrum of the filament, motivated by spectroscopic applications. The spectral complementarity of two filaments induced from a donut beam raises questions about the phase properties of the generated spectrum during filamentation. The introduction of fast imaging via streak camera should be enhanced by the spectral analysis of the filament plasma. The study of the neutral and ionized molecules would provide an understanding of the dynamics of the multi-photon ionization, excitation decay, dissociation and fluorescence, and the evolution of the plasma in an applied electric field. The temporal measurement of the polarization is another important factor to be investigated and considered in potential applications which are impacted by polarization, such as THz generation.

Filamentation in molecular gases, celebrating its 20th anniversary at the time of this thesis, has shown what interdisciplinary collaboration can bring to such a complex phenomenon: laser engineering for its development of laser sources, atomic, molecular and optical (AMO) science for the understanding

of the nonlinear processes leading to filamentation, plasma physics for the determination of the ionization processes as well as the plasma chemistry for the analysis of the molecular emission from the ionized channel. For instance, new models for the molecular response to an elliptical beam need to be implemented to the common nonlinear Schrödinger equation. A detailed study of the ionization paths should be studied for a better understanding of the ionization losses. And the phase relation between co-induced filaments should be targeted. These examples bring a lot of excitement in the field of filamentation, opening new dimensions for the control of the phenomenon and in a near future engineered applications for defense, sensing and communication.

References

[1] A. Couairon and A. Mysyrowicz. Femtosecond filamentation in transparent media. *Physics Reports*, 441:49–189, 2007.

[2] J.-C. Diels, J. Yeak, D. Mirell, R. Fuentes, S. Rostami, D. Faccio, and P. di Trapani. Air filaments and vacuum. *Laser Physics*, 20:1101–1106, 2010.

[3] Pierre Béjot. *Theoretical and experimental investigations of ultrashort laser filamentation in gases*. PhD thesis, University of Geneva, 2008.

[4] Shermineh Rostami, Michael Chini, Khan Lim, John P. Palastro, Magali Durand, Jean-Claude Diels, Ladan Arissian, Matthieu Baudelet, and Martin Richardson. Dramatic enhancement of supercontinuum generation in elliptically-polarized laser filaments. arXiv:1505.01199, 2015.

[5] J. Kasparian, R. Sauerbrey, D.. Mndelain, S. niedermeier, J. Yu, J. P. Wolf, Y.-B.André, M. Franco, B. Prade, S. Tzortzakis, A. Mysyrowicz, M. Rodriguez, H. Wille, and L. Wöste. Infrared extension of the super-

continuum generated by femtosecond terawatt laser pulses propagating in the atmosphere. *Opt. Lett.*, 25:1397–1399, 2000.

[6] A. Becker, N. Aközbek, K. Vijayalakshmi, E. Oral, C. M. Bowden, and S. L. Chin. Intensity clamping and re-focusing of intense femtosecond laser pulses in nitrogen molecular gas. *Appl. Phys. B*, 73:287–290, 2001.

[7] J.-F. Daigle, A. Jacon-Becker, S. Hosseiniand T.-J. Wang, Y. Kamali, G. Roy, A. Becker, and S. L. Chin. Intensity clamping measurement of laser filaments in air at 400 and 800 nm. *Physical Review A*, 82: 023405, 2010.

[8] Shermineh Rostami, J.-C. Diels, and L. Arissian. Polarization evolution of ultrashort pulses in air. *Optics Express*, 23:3299–3307, 2015.

[9] H. L. Xu and S. L. Chin. Femtosecond laser filamentation for atmospheric sensing. *Sensors*, 11(1):32–53, 2011.

[10] R. B. Miles, J. B. Michael, C. M. Limbach, S. D. McGuire, T. L. Chng, M. R. Edwards, N. J. DeLuca, M. N. Shneider, and A. Dogariu. New diagnostic methods for laser plasma and microwave-enhanced combustion. *Phil. Trans. R. Soc. A.*, 373:20140338, 2015.

[11] A. Talebpour, M. Abdel-Fattah, A. D. Bandrauk, and S. L. Chin. Spectroscopy of the gases interacting with intense femtosecond laser pulses. *Laser Physics*, 11(1):68–76, 2001.

[12] Khan Lim. *Laser filamentation- beyond self-focusing and plasma defocusing*. PhD thesis, Univeristy Of Central Florida, 2014.

[13] URL `https://en.wikipedia.org/wiki/Orbital_angular_momentum_of_light`.

[14] M. Padgett, J. Courtial, and L. Allen. Light's orbital angular momentum. *Physics today*, 57(5):35–40, May 2004.

[15] M. Spanner. *Field-Free Alignment and Strong Field Control of Molecular Rotors*. PhD thesis, University of Waterloo, 2004.

[16] S. L. Chin, T.J. Wang, C. Marceau, J. Wu, J. S. Liu, O. Kosareva, N. Panov, Y. P. Chen, J.F. Daigle, S. Yuan, A. Azarma, W. W. Liu, T. Seideman, H. P. Zeng, M. Richardson, R. Li, and Z. Z. Xu. Advances in intense femtosecond laser filamentation in air. *Laser Physics*, pages 1– 53, 2011.

[17] Andreas Velten, Andreas Schmitt-Sody, Jean-Claude Diels, Shermineh Rostami, Amin Rasoulof, Chengyong Feng, and Ladan Arissian. Videos of light filamentation in air. *Journal of Physics B: Atomic, Molecular and Optical Physics*, 48:094020, 2015.

[18] Robert W. Boyd. *Nonlinear optics*. Academic Press, third edition, 2008.

[19] P. L. Kelley. Self-focusing of optical beams. *Phys. Rev. Lett.*, 15:1005–1008, 1965.

[20] G. A. Askar'yan. The self-focusing effect. *Sov. Phys. J.*, 16:680, 1974.

[21] A. Braun, G. Korn, X. Liu, D. Du, J. Squier, and G. Mourou. Self-channeling of high-peak-power femtosecond laser pulses in air. *Optics Lett.*, 20:73–75, 1995.

References

[22] R. R. Alfano and S. L. Shapiro. Emission in the region 4000 to 7000 å. *Phys. Rev. Lett.*, 24:584–587, 1970.

[23] R. R. Alfano and S. L. Shapiro. Observation of self-phase modulation and small-scale filaments in crystals and glasses. *Phys. Rev. Lett.*, 24: 592–594, 1970.

[24] R. R. Alfano and S. L. Shapiro. Direct distortion of electric clouds of rare-gas atoms in intense electric fields. *Phys. Rev. Lett*, 24:1217–1220, 1970.

[25] A. Brodeur and S. L. Chin. Ultrafast white-light continuum generation and self-focusing in transparent condensed media. *J. Opt. Soc. Am. B*, 16:637–650, 1999.

[26] Y. R. Shen. *The Principles of Nonlinear Optics*. John Wiley & Sons, New York, 1984.

[27] G. Yang and Y. Shen. Spectral broadening of ultrashort pulses in a nonlinear medium. *Opt. Lett.*, 9:510–512, 1984.

[28] A. L. Gaeta. Catastrophic collapse of ultrashort pulses. *Phys. Rev. Lett.*, 84:3582–3585, 2000.

[29] J. K. Ranka, R. W. Schirmer, and A. L. Gaeta. Observation of pulse splitting in nonlinear dispersive media. *Phys. Rev. Lett.*, 77:3783–3786, 1996.

[30] A. Proulx, A. Talebpour, S. Petit, and S. L. Chin. Fast pulsed elec-

tric field created from the self-generated filament of a femtosecond Ti:sapphire laser pulse in air. *Optics Comm.*, 174:305–309, 2000.

[31] S. Tzortzakis, M. A. Franco, Y. B. André, A. Chiron, B. Lamouroux, B. S. Prade, and A. Mysyrowicz. Formation of a conducting channel in air by self-guided femtosecond laser pulses. *Phys. Rev. E*, 60:R3505–R3507, 1999.

[32] S. Tzortzakis, B. S. Prade, M. A. Franco, and A. Mysyrowicz. Time-evolution of the plasma channel at the trail of a self-guided ir femtosecond laser pulse in air. *Optics Comm*, 181:123–127, 2000.

[33] H. Schillinger and R. Sauerbrey. Electrical conductivity of long plasma channels in air generated by self-guided femtosecond laser pulses. *Applied Physics B*, 68:753–756, 1999.

[34] D. Close, C. Giuliano, R. Hellwarth, L. Hess andF. McClung, and W. Wagner. Evolution of circularly polarized light in a kerr medium. *IEEE J. of Quantum Electronics*, QE-2:553–557, 1966.

[35] D. Strickland and G. Mourou. Compression of amplified chirped optical pulses. *Optics Comm.*, 56:219–221, 1985.

[36] P. Maine and G. Mourou. Amplification of 1 ns pulses in Nd:glass followed by compression to 1 ps. *Opt. Lett.*, 13:467, 1988.

[37] M. C. Richardson and A. J. Alcock. Interferometric observation of plasma filaments in a laser-produced spark. *Applied Phys. Lett.*, 18(8): 357–360, April 1971.

[38] J.-C. Diels and W. Rudolph. *Ultrashort Laser Pulse Phenomena*. Academic Press - Elsevier, second edition, 2006.

[39] R. Y. Chiao, P. L. Kelley, and E. Garmire. Stimulated four-photon interaction and its influence on stimulated Raleight-wing scattering. *Physics Review Letter*, 17:1158, 1966.

[40] J. H. Marburger. Self-focusing. In J. H. Sanders and S. Stendholm, editors, *Progr. Quantum Electron.*, volume 4, pages 35–110. Pergamon, Oxford, 1975.

[41] S. A. Akhmanov, A. P. Sukhorukov, and R. V. Khokhlov. Development of an optical waveguide in the propagation of light in a nonlinear medium. *Sov. Phys JETP*, 24:198–201, 1967.

[42] G. Fibich and A. L. Gaeta. Critical power for self-focusing in bulk media and in a hollow waveguides. *Optics Lett.*, 29:1772–1774, 2004.

[43] P. Sprangle, J. R. Penano, and B. Hafizi. Propagation of intense short laser pulses in the atmosphere. *Physical Review E*, 66:046418, 2002.

[44] Aaron Bernstein, T. S. Luk, T. R. Nelson, J.-C. Diels, and S. Cameron. Observation of multiple pulse-splitting of ultrashort pulses in air. In *QELS 2001, QFC6*, pages 262–263, Baltimore, MY, 2001. Optical Society of America.

[45] A.C. Bernstein, T.S. Luk, T.R. Nelson, A. McPherson, J.-C. Diels, and S.M. Cameron. Asymmetric ultra-short pulse splitting measured in air using frog. *Applied Physics B (Lasers and Optics)*, B75(1):119 – 122, July 2002.

[46] G. G. Luther, J. V. Moloney, A. C. Newell, and E. M. Wright. Self-focusing threshold in normally dispersive media. *Opt. Lett.*, 19:862–864, 1994.

[47] G. Fibich, S. Eisenmann, B. Ilan, and A. Zigler. Control of multiple filamentation in air. *Optics Lett.*, 25:335–337, 2000.

[48] Pavel Polynkin and Miroslav Kolesik. Critical power for self-focusing in the case of ultrashort laser pulses. *Physical Review A*, 87:053829, 2013.

[49] V. Talanov. Focusing of light in cubic media. *JETP Lett.*, 11:199–201, 1970.

[50] A. Couairon and L. Bergé. Light filaments in air for ultraviolet and infrared wavelengths. *Phys. Rev. Lett*, 88:13503–1—13503–4, 2002.

[51] A. Mysyrowicz, A. Couairon, and U. Keller. Self-compression of optical laser pulses by filamentation. *New J. Phys.*, 10(2):025023, 2008.

[52] L. Arissian, C. Smeenk, F. Turner, A. Staudte, A. Sokolov, D. Villeneuve, and P B Corkum. The structure of the electron wavepacket in optical tunnel ionization. *Physical Review Letters*, 105:133002, 2010.

[53] M. D. Feit and J. A. Fleck. Effect of refraction on spot-size dependence of laser-induced breakdown. *Appl. Phys. Lett.*, 24:169–171, 1974.

[54] Q. Feng, J. V. Moloney, A. C. Newell, E. M. Wright, K. Cook, P. K. Kennedy, D. X. Hammer, B. A. Rockwell, and C. R. Thompson. Theory and simulation on the threshold of water breakdown induced by focused

ultrashort laser pulses. *IEEE Journal of Quantum Electron.*, 33:127–137, 1997.

[55] V. N. Lugovoi and A. M. Prokhorov. A possible explanation of the small-scale self-focusing filament. *JETP Lett.*, 7:117–119, 1968.

[56] A. Brodeur, C. Y. Chien, F. A. Ilkov, S. L. Chin, O. G. Kosareva, and V. P. Kandidov. Moving focus in the propagation of ultrashort laser pulses in air. *Optics Lett.*, 22:304–306, 1997.

[57] H.R. Lange, G. Grillon, M. A. Franco J. F. Ripoche, J.-F., B. Lamouroux, B. S. Prade, A. Mysyrowicz, E. T. J. Nibbering, and A. Chiron. Anomalous long-range propagation of femtosecond laser pulses through air: moving focus or pulse self-guiding. *Opt. Lett.*, 23(2):120–122, 1998.

[58] V. Loriot, E. Hertz, O. Fauchet, and B. Lavorel. Measurement of high order kerr refractive index of major air components. *Optics Express*, 17:13439–13434, 2009.

[59] M. Mlejnek, E. M. Wright, and J. V. Moloney. Dynamic spatial replenishment of femtosecond pulse propagating in air. *Opt. Lett.*, 23: 382–384, 1998.

[60] J. V. Moloney M. Mlejnek, M. Kolesik and E. M. Wright. Optically turbulent femtosecond light guide in air. *Phys. Rev. Lett.*, 83:2938–2941, 1999.

[61] A. Dubietis, E. Gaisauskas, G. Tamosauskas, and P. Di Trapani. Light filaments without self-channeling. *Phys. Rev. Lett.*, 92:253903–1—253903–5, 2004.

[62] S. A. Akhmanov, A. P. Sukhorukov, and R. V. Khokhlov. Self focusing and self trapping of intense light beams in a nonlinear medium. *Sov. Phys JETP*, 23:1025–1033, 1966.

[63] S. A. Akhmanov, V A Vysloukh, and A. S. Chirkin. *Optics of femtosecond laser pulses*. AIP Press, 1991.

[64] D. Faccio, A. Porras, A. Dubietis, F. Bragheri, A. Couairon, and P. Di Trapani. Conical emission, pulse splitting, and X-wave parametric amplification in nonlinear dynamics of ultrashort light pulses. *Phys. Rev. Lett.*, 96:193901, 2006.

[65] D. Faccio, A. Averchi, A. Lotti1, P. Di Trapani, A. Couairon, D. Papazoglou, and S. Tzortzakis. Ultrashort laser pulse filamentation from spontaneous X-Wave formation in air. *Optics Express*, 16:1565–1570, 2008.

[66] E. Gaizauskas, A. Dubietis, V. Kudriasov, V. Sirutkaitis, A. Couairon, D. Faccio, and Paolo Di Trapani. On the role of conical waves in self-focusing and filamentation of femtosecond pulses with nonlinear losses. In M. Bass, editor, *Self-Focusing, past and present*, pages 457–479. Springer, Berlin, Heidelberg, 2009.

[67] M. Mlejnek, E.M. Wright, and J.V. Moloney. Power dependence of dynamic spatial replenishment of femtosecond pulses propagating in air. *OPTICS EXPRESS*, 4(7):223–228, 1999.

[68] E. T. J. Nibbering, G. Grillon, M. A. Franco, B. S. Prade, and A. Mysyrowicz. Determination of the inertial contribution to the nonlinear re-

fractive index of air, N_2, and O_2 by use of unfocused high-intensity femtosecond laser pulses. *J. Opt. Soc. Am.*, B14:650–660, 1997.

[69] W. Liu, S. Petit, A. Becker, N. Aközbek, C. M. Bowden, and S. L. Chin. Intensity clamping of a femtosecond laser pulse in condensed matter. *Opt. Commun.*, 202:189–197, 2002.

[70] F. DeMartini, C. H. Townes, T. K. Gustafson, and P. L. Kelley. Self-steepening of light pulses. *Phys. Rev.*, 164:312–323, 1967.

[71] J. E. Rothenberg. Space - time focusing: breakdown of the slowly varying envelope approximation in the self-focusing of femtosecond pulses. *Opt. Lett.*, 17(19):1340, October 1992.

[72] T. Brabec and F. Krausz. Nonlinear optical pulse propagation in the single-cycle regime. *Phys. Rev. Lett.*, 78:3282–3284, 1997.

[73] A. Couairon, J. Biegert, C. P. Hauri, U. Keller, and A. Mysyrowicz. Self-generation of near-single-cycle pulses through filamentation. *Journal of Modern Optics*, 53:75–85, 2005.

[74] C. P. Hauri, W. Kornelis, F. W. Helbing, A. Heinrich, A. Couairon, A. Mysyrowicz, J. Biegert, and U. Keller. Generation of intense, carrier-envelope phase-locked few-cycle laser pulses through filamentation. *Applied Physics B*, 79:673–677, 2004.

[75] H. S. Chakraborty, M. B. Gaarde, and A. Couairon. Single attosecond pulses from high harmonics driven by self-compressed filament. *Opt. Lett.*, 31:3662, 2006.

[76] S. L. Chin. Femtosecond laser filamentation. In *Atomic, Optical, and Plasma Physics*, Springer Series. Springer, 2009.

[77] V. P. Kandidov, O. G. Kosareva, and A. A. Koltun. Nonlinear-optical transformation of a high-power femtosecond laser pulse in air. *Quantum Electronics*, 33(1):69, 2003.

[78] P. B. Corkum, C. Rolland, and T. Srinivasan-Rao. Supercontinuum generation in gases. *Phys. Rev. Lett.*, 57(18):2268, 1986.

[79] X. L. Liu, X. Lu, X. Liu, L. B. Feng, J. L. Ma, Y. T. Li, L. M. Chen, Q. L. Dong, W. M. Wang, Z. H. Wang, Z. Y. Wei, Z. M. Sheng, and J. Zhang. Broadband supercontinuum generation in air using tightly focused femtosecond laser pulses. *Opt. Lett.*, 36(19):3900, 2011.

[80] M. Durand, A. Houard, B. Prade, A. Mysyrowicz, A. Durécu, D. Fleury, B. Moreau, O. Vasseur, H. Borchert, K. Diener, R. Schmitt, F. Théberge, M. Chateauneuf, and J. Dubois. Kilometer range filamentation. *Optics Express*, 21:26836–26845, 2013.

[81] S. Driever, D. Bigourd, N. Fedorov, M. Cornet M. Arnold, F. Burgy, S. Montant, S. Petit, D. Descamps, E. Cormier, E. Constant, and A. Zaïr. Tunable 1.6–2μm near infrared few-cycle pulse generation by filamentation. *Appl. Phys. Lett.*, 102(19):191119, 2013.

[82] J. Kasparian, M. Rodriguez, J. Méjean, J. Yu, E. Salmon, H. Wille, R. Bourayou, S. Frey, Y.-B.André, A. Mysyrowicz, R. Sauerbrey, J. P. Wolf, and L. Wöste. White-light filaments for atmospheric analysis. *Science*, 301:61–64, 2003.

[83] M. Chateauneuf, S. Payeur, J. Dubois, and J.-C. Kieffer. Microwave guiding in air by a cylindrical filament array waveguide. *Applied Physics Letters*, 92:091104, 2008.

[84] V. V. Valuev, A. E. Dormidonov, V. P. Kandidov, S. A. Shlenov, V. N. Kornienko, and V. A. Cherepenin. Plasma channels formed by a set of filaments as a guiding system for microwave radiation. *Journal of communications technology and electronics*, 55(2):208–214, 2010.

[85] Z. A. Kudyshev, M. C. Richardson, and N. M. Litchinitser. Virtual hyperbolic metamaterials for manipulating radar signals in air. *Nat. Commun.*, 4:2557, 2013.

[86] L. Arantchouk, A. Houard, Y. Brelet, J. Carbonnel, J. Larour, Y. B. Andre, and A. Mysyrowicz. A simple high-voltage high current spark gap with subnanosecond jitter triggered by femtosecond laser filamentation. *Appl. Phys. Lett.*, 102(16):163502, 2013.

[87] B. Forestier, A. Houard, I. Revel, M. Durand, Y. B. Andre, B. Prade, A. Jarnac, J. Carbonnel, M. Le Nevé, J. C. de Miscault, B. Esmiller, D. Chapuis, and A. Mysyrowicz. Triggering, guiding and deviation of long air spark discharges with femtosecond laser filament. *AIP Adv.*, 2 (1):012151, 2012.

[88] Y. Brelet, A. Houard, G. Point, B. Prade, L. Arantchouk, J. Carbonnel, Y.-B. Andre, M. Pellet, and A. Mysyrowicz. Radiofrequency plasma antenna generated by femtosecond laser filaments in air. *Appl. Phys. Lett.*, 101:264106, 2012.

[89] K. Guo, J. Lin, Z. Hao, X. Gao, Z. Zhao, C. Sun, and B. Li. Triggering and guiding high-voltage discharge in air by single and multiple femtosecond filaments. *Opt. Lett.*, 37(2):259–261, 2012.

[90] P. Rohwetter, J. Kasparian, K. Stelmaszczyk, Z. Hao, Stefano Henin, N. Lascoux, W. M. Nakaema, Y. Petit, M. Queißer, R. Salame, E. Salmon, L. Wöste, and J. P. Wolf. Laser-induced water condensation in air. *Nature Photonics*, 4:451–456, 2010.

[91] Xiao-Long Liu, Xin Liu, Jing-Long Ma, Liu-Bin Feng, Xu lei Ge, Yi Zheng, Yu-Tong Li, Li-Ming Chen, Quan-Li Dong, Wei-MinWang, Zhao-HuaWang, Hao Teng, Zhi-Yi Wei, and Jie Zhang. Long lifetime air plasma channel generated by femtosecond laser pulse sequence. *Optics Express*, 20:5968–5973, 2012.

[92] P. Joly, M. Petrarca, A. Vogel, T. Pohl, T. Nagy, Q. Jusforgues, P. Simon, J. Kasparian, K. Weber, and J.-P. Wolf. Laser-induced condensation by ultrashort laser pulses at 248nm. *Appl. Phys. Lett.*, 102:091112, 2013.

[93] F. Théberge, W. Liu, P. Tr. Simard, A. Becker, and S. L. Chin. Plasma density inside a femtosecond laser filament in air: Strong dependence on external focusing. *Phys. Rev. E.*, 74:036406, 2006.

[94] A. Talebpour, S. Petit, and S. L. Chin. Re-focusing during the propagation of a focused femtosecond Ti:sapphire laser pulse in air. *Optics Comm.*, 171:285–290, 1999.

[95] S. Tzortzakis, G. Méchain, G. Patalano, Y.-B. André, B. Prade, M. Franco, A. Mysyrowicz, J.-M. Munier, M. Gheudin, G. Beaudin, and P. Encrenaz. Coherent subterahertz radiation from femtosecond infrared filaments in air. *Opt. Lett.*, 27(21):1944–1946, Nov 2002.

[96] S. L. Chin, F. Théberge, and W. Liu. Filamentation nonlinear optics. *Appl. Phys. B.*, 86:477–483, 2007.

[97] Xin Miao Zhao, C. Y. Yeh, J. C. Diels, and Cai Yi Wang. Ultrashort pulse propagation for triggering of lightning. In R. C. Sze and F. J. Duarte, editors, *Proceedings of the int. conf. on Laser's 91*, San Diego, CA, December 1991. SOQE, SPS press, McLean, Virginia.

[98] Xin Miao Zhao, Jean-Claude Diels, A. Braun, X. Liu, D. Du, G. Korn, G. Mourou, and Juan Elizondo. Use of self-trapped filaments in air to trigger lightning. In P. F. Barbara, W. H. Knox, G. A. Mourou, and A. H. Zewail, editors, *Ultrafast Phenomena IX*, pages 233–235, Dana Point, CA, 1994. Springer Verlag, Berlin.

[99] P. K. Rambo, J. Biegert, V. Kubecek, J. Schwarz, A. Bernstein, J. C. Diels, R. Bernstein, and K. Stahlkopf. Laboratory tests of laser induced lightning discharge. *Journal of Optical Technology*, 66:194–198, 1999.

[100] P. Rambo, J. Schwarz, and J.-C. Diels. Femtosecond pulse interferometry of a laser plasma. In *CLEO 2000, technical digest*, volume CWT7, page 378, San Francisco, Ca, 2000. Optical Society of America.

[101] P. K. Rambo, J. Schwarz, and J. C. Diels. High voltage electrical

discharges induced by an ultrashort pulse UV laser system. *Journal of Optics A*, 3:146–158, 2001.

[102] S. Tzortzakis, L. Bergé, A. Couairon, M. A. Franco, B. S. Prade, and A. Mysyrowicz. Breakup and fusion of self-guided femtosecond light pulses in air. *Phys. Rev. Lett*, 86:5470–5473, 2001.

[103] N. Barbieri. *Engineering and Application of Ultrafast Laser Pulses and Filamentation in Air*. PhD thesis, Univeristy of Central Florida, 2013.

[104] Y. Ren, M. Alshershby, Z. Hao, Z. Zhao, and Jingquan Lin. Microwave guiding along double femtosecond filaments in air. *Phys. Rev. E.*, 88: 013104, July 2013.

[105] Y. Ren, M. Alshershby, J. Qin, Z. Hao, and J. Lin. Microwave guiding in air along single femtosecond laser filament. *Journal of Applied Physics*, 113:094904, 2013.

[106] J. Odhner and R. Levis. Optical spectroscopy using gas-phase femtosecond laser filamentation. *Annu. Rev. Phys. Chem.*, 65:605–628, Jan. 2014.

[107] P. Rairoux, H. Schillinger, S. Niedermeier, M. Rodriguez, F. Ronneberger, R. Sauerbrey, B. Stein, D. Waite, C. Wedeking, H. Wille, L. Woeste, and C. Ziener. Remote sensing of the atmosphere using ultrashort laser pulses. *Appl. Phys. B*, 71:573–580, 2000.

[108] T. Somekawa, M. Fujita, and Y. Izawa. Direct absorption spectroscopy of CO_2 using a coherent white light continuum. *Appl. Phys. Express.*, 3(8):082401, 2010.

[109] A. W. Miziolek, V. Palleschi, and I. Schechter. *Laser Induced Breakdown Spectroscopy*. Cambridge University Press, 2006.

[110] S. Tzortzakis, D. Anglos, and D. Gray. Ultraviolet laser filaments for remote laser-induced breakdown (libs) spectroscopy: Application in cultural heritage monitoring. *Optics Letters*, 31:1139–1141, 2006.

[111] M. Weidman, M. Baudelet, M. Fisher, C. Bridge, C. Brown, M. Sigman, P. J. Dagdigian, and M. Richardson. Molecular signal as a signature for detection of energetic materials in filament-induced breakdown spectroscopy. In *Proc. SPIE*, volume 7304, pages 73041G–73041G–7, 2009.

[112] M. Baudelet, M. Richardson, and M. Sigman. Self-channeling of femtosecond laser pulses for rapid and efficient standoff detection of energetic materials. In *IEEE Conference on Technologies for Homeland Security*, pages 472–476, 2009.

[113] K. Stelmaszczyk, P. Rohwetter, G. Méjean, J. Yu, E. Salmon, J. Kasparian, R. Ackermann, J. P. Wolf, and L. Wöste. Long-distance remote laser-induced breakdown spectroscopy using filamentation in air. *Appl. Phys. Lett.*, 85:3977–3979, 2004.

[114] J.-F. Daigle, G. Méjean, W. Liu, F. Théberge, H.L. Xu, Y. Kamali, J. Bernhardt, A. Azarm, Q. Sun, P. Mathieu, G. Roy, J.-R. Simard, and S.L. Chin. Long range trace detection in aqueous aerosol using remote filament-induced breakdown spectroscopy. *Applied Phsics B*, 87(4):749–754, May 2007.

[115] Daniel Mirell. *Experimental study of infrared filaments under different initial conditions*. PhD thesis, University of New Mexico, April 2009.

[116] Olivier J. Chalus, A. Sukhinin, A. Aceves, and J.-C. Diels. Propagation of non-diffracting intense ultraviolet beams. *Optics Communication*, 281:3356–3360, 2008.

[117] P. D. Maker, R. W. Terhune, and C. M. Savage. *Quantum Electronics*, Proc. 3rd Int. Congr., Paris:1559–1576, 1964.

[118] R. W. Boyd and E. L. Buckland. Nonlinear optical interactions in optical fibers. *J. Nonlinear optical physics and materials*, 7(1):105–112, 1998.

[119] M. L. Miguez, E. C. Barbano, S. C. Zilio, and L. Misoguti. Accurate measurement of nonlinear ellipse rotation using a phase-sensitive method. *Optics Express*, 22(21):25530, 2014.

[120] URL `http://www.iiviinfrared.com/Optical-Materials/zns.html`.

[121] O. Madelung, U. Rössler, and M. Schulz, editors. *Landolt-Börnstein - Group III Condensed Matter*, volume 41B. Springer Berlin Heidelberg, 1999.

[122] Y.H. Chen, S. Varma, T. M. Antonsen, and H. M. Milchberg. Direct measurement of the electron density of extended femtosecond laser pulse-induced filaments. *Phys Rev Lett*, 105:215005, 2010.

[123] Jianming Dai, Nicholas Karpowicz, and X-C. Zhang. Coherent Polarization Control of Terahertz Waves Generated from Two-Color Laser-

Induced Gas Plasma. *Physical Review Letters*, 103(2):023001, JUL 10 2009.

[124] Bing Zhou, Aurélien Houard, Yi Liu, Bernard Prade, André Mysyrowicz, Arnaud Couairon, Patrick Mora, Christopher Smeenk, Ladan Arissian, and Paul Corkum. Measurement and control of plasma oscillations in femtosecond filaments. *Physical Review Letters*, 106(15): 255002, 1 August 2011.

[125] V. S. Popov. Tunnel and multiphoton ionization of atoms and ions in a strong laser field (kelysh theory). *Phys.-Usp*, 47:855, 2004.

[126] L. Arissian and J.-C. Diels. Ultrafast electron plasma index; an ionization perspective. *Journal of Lasers, Optics & Photonics*, 1:107–111, 2014.

[127] M. Artamanov and T. Seideman. Theory of three-dimensional alignment by intense laser pulses. *J. Chem. Phys.*, 128:154313, 2008.

[128] J. Schj-Eriksen, J. V. Moloney, E. M. Wright, Q. Feng, and P. L. Christiansen. Polarization instability of femtosecond pulse splitting in normally dispersive self-focusing media. *Opt. Lett.*, 26(2):78–80, 2001.

[129] M. Kolesik, J. V. Moloney, and E. M. Wright. Polarization dynamics of femtosecond pulses propagating in air. *Physical Review E*, 64:046607, 2001.

[130] G. Fibich and B. Ilan. Multiple filamentation of circularly polarized beams. *Phys. Rev. Lett.*, 89(1):013901, 2002.

[131] G. Fibich and B. Ilan. Self-focusing of circularly polarized beams. *Physical Review E*, 67:036622, 2003.

[132] D. Faccio, A. Porras, A. Dubietis, G. Tamosauskas, E. Kucinskas, A. Couairon, and P. Di Trapani. Angular and chromatic dispersion in kerr-driven conical emission. *Optics Communications*, 265:672–677, 2006.

[133] F. Théberge, M. Châteauneuf, V. Ross, P. Mathieu, and J. Dubois. Ultrabroadband conical emission generated from the ultraviolet up to the far-infrared during the optical filamentation in air. *Optics Letters*, 33(21):2515–2517, 2008.

[134] Ladan Arissian, Daniel Mirell, Shermineh Rostami, Aaron Bernstein, Daniele Faccio, and Jean-Claude Diels. The effect of propagation in air on the filament spectrum. *Optics Express*, 20:8337–8343, 2012.

[135] J. P. Palastro. Time-dependent polarization states of high-power, ultrashort laser pulses during atmospheric propagation. *Phys. Rev. A*, 89:013804, 2014.

[136] H.D. Ladouceura, A.P. Baronavski, D. Lohrmann, P.W. Grounds, and P.G. Girardic. Electrical conductivity of a femtosecond laser generated plasma channel in air. *Opt. Commun.*, 189(1-3):107–111, March 2001.

[137] B. La Fontaine, F. Vidal, Z. Jiang, C. Y. Chien, D. Comtois, A. Desparois, T. W. Johnston, J.-C. Kieffer, and H. Pepin. Filamentation of ultrashort pulse laser beams resulting from their propagation over long distances in air. *Physics of Plasmas*, 6:1615–1621, 1999.

[138] S. Eisenmann, A. Pukhov, and A. Zigler. Fine structure of a laser-plasma filament in air. *Phys. Rev. Lett.*, 98:155002, 2007.

[139] J. Yu, D. Mondelain, J. Kasparian, E. Salmon, S. Geffroy, C. Favre, V. Boutou, and J.-P. Wolf. Sonographic probing of laser filaments in air. *Applied Optics*, 42(36):7117–7120, 2003.

[140] H. Zuo-Qiang, Y. Jin, Z. Jie, L. Yu-Tong, Y. Xiao-Hui, Z. Zhi-Yuan, W. Peng, W. Zhao-Hua, L. Wei-Jun, and W. Zhi-Yi. Acoustic diagnostics of plasma channels induced by intense femtosecond laser pulses in air. *Chin. Phys. Lett*, 22(3):636–639, 2005.

[141] Q. Luo, S.A. Hosseini, B. Ferland, and S.L. Chin. Backward time-resolved spectroscopy from filament induced by ultrafast intense laser pulses. *Opt. Commun.*, 233(4-6):411–416, April 2004.

[142] H.L. Xu, A. Azarm, J. Bernhardt, Y. Kamali, and S.L. Chin. The mechanism of nitrogen fluorescence inside a femtosecond laser filament in air. *Chemical Physics*, 360:171–175, 2009.

[143] J. Bernhardt, P.T. Simard, W. Liu, H.L. Xu, F. Théberge, A. Azarm, J.F. Daigle, and S.L. Chin. Critical power for self-focussing of a femtosecond laser pulse in helium. *Optics Commun.*, 281(8):2248–2251, April 2008.

[144] P. Paris, M. Aints, F. Valk, T. Plank, A. Haljaste, K. V. Kozlov, and H. E. Wagner. Intensity ratio of spectral bands of nitrogen as a measure of electric field strength in plasmas. *J. of Physics D: Applied Physics*, 38(21):3894, 2005.

[145] S. L. Chin, A. Talebpour, J. Yang, S. Petit, V. P. Kandidov, O. G. Kosareva, and M. P. Tamarov. Filamentation of femtosecond laser pulses in turbulent air. *Applied Physics Letters*, B74:67–76, 2002.

[146] Y. Chen, F. Théberge, O. Kosareva, N. Panov, V. P. Kandidov, and S. L. Chin. Evolution and termination of a femtosecond laser filament in air. *Optics Letters*, 32(24):3477–3479, 2007.

[147] S. Petit, A. Talebpour, A. Proulx, and S. L. Chin. Polarization dependence of the propagation of intense laser pulses in air. *Optics Communication*, 175:323–327, 2000.

[148] P.P. Kiran, S. Bagchi, C.L. Arnold, S.R. Krishnan, G. R. Kumar, and A. Couairon. Filamentation without inten- sity clamping. *Opt. Express*, 18(20):21504–21510, September 2010.

[149] A. Srivastava and D. Goswami. Polarization-induced modulation of a femtosecond nonlinear process. *Phys. Lett. A*, 341:523, 2005.

[150] A. S. Sandhu amd S. Banerjee and D. Goswami. Suppression of supercontinuum generation with circularly polarized light. *Opt. Commun.*, 181(1):101–107, July 2000.

[151] J. Liu, X. W. Chen, R. X. Li, and T. Kobayashi (1984). Polarization-dependent pulse com- pression in an argon-filled cell through filamentation. *Laser Phys. Lett.*, 5(1):45–47, Jan 2008.

[152] H. Yang, J. Zhang, Q. Zhang, Z. Hao, Y. Li, Z. Zheng, Z. Wang, Q. Dong, X. Lu, Z. Wei, and Z. M. Sheng. Polarization-dependent

supercontinuum generation from light filaments in air. *Optics letters*, pages 534–536, 2005.

[153] Oscar Varela, Amelle Zair, Julio San Roman, Benjamyn Alonso, Nigo Juan Sola, Camilo Prieto, and Luis Roso. Above-millijoule supercontinuum generation using polarisation dependent filamentation in atoms and molecules. *Optics Express*, 17:3630–3639, 2009.

[154] B. Webb et al. CLEO 2014, Science and Innovations (Optical Society of America, 2014.

[155] K. Lim, M. Durand, M. Baudelet, and M. Richardson. Transition from linear- to nonlinear-focusing regime in filamentation. *Science Reports*, 4:7217, 2014.

[156] S. Rostami, M. Chini, K. Lim, J. Palastro, M. Durand, J.-C. Diels, L. Arissian, M. Baudelet, and M. Richardson. Enhanced supercontinuum generation by polarization control of filamentation in molecular gases. In *CLEO, 2015*, number SF2D.5, San Jose, CA, May 2015.

[157] J. K. Wahlstrand, Y. H. Cheng, and H. M. Milchberg. Absolute measurement of the transient optical nonlinearity in N_2, O_2, N_2O, and Ar. *Phys. Rev. A.*, 85:043820, 2012.

[158] C. H. Lin, J. P. Heritage, T. K. Gustafson, R. Y. Chiao, and J. P. McTague. Birefringence arising from the reorientation of the polarizability anisotropy of molecules in collisionless gases. *Phys. Rev. A.*, 13: 813–829, 1976.

[159] S. V. Popruzhenko, V. D. Mur V. S. Popov, and D. Bauer. Strong field ionization rate for arbitrary laser frequencies. *Phys. Rev. Lett.*, 101: 193003, 2008.

[160] S. Mitryukovskiy, Y. Liu, P. Ding, A. Houard, A. Couairon, and A. Mysyrowicz. Plasma luminescence from femtosecond filaments in air: Evidence for impact excitation with circularly polarized pulses. *Phys. Rev. Lett.*, 114:063003, 2015.

[161] J. H. Poynting. The wave motion of a revolving shaft, and a suggestion as to the angular momentum in a beam of circularly polarised light. *Proc. R. Soc. Lond. A.*, 82:560–567, July 1909.

[162] L. Allen, M. W. Beijersbergen, R. J. C. Spreeuw, and J. P. Woerdman. Orbital angular momentum of light and the transformation of laguerre-gaussian laser modes. *Phys. Rev. A*, 45:8185, June 1992.

[163] O. Bryngdahl. Radial- and circular-fringe interferograms. *J. Opt. Soc. Am*, 63(9):1098–1104, 1973.

[164] J. F. Nye and M. V. Berry. Dislocations in wave trains. *Proc. R. Soc. Lond. A.*, 336:165–190, 1974.

[165] M. V. Berry. Singularities in waves and rays. In R. Balian, M. Kleman, and J. P Poirier, editors, *Physics of Defects, Les Houches Session 35*, pages 453–543. North-Holland, Amsterdam, 1981.

[166] P. Coullet, L. Gil, and F. Rocca. Optical vortices. *Opt. Comm.*, 73(5): 403–408, 1989.

[167] M. W. Beijersbergen, L. Allen, H. E. L. O. van der Veen, and J. P. Woerdman. Astigmatic laser mode converters and transfer of orbital angular momentum. *Opt. Commun.*, 96:123–132, 1993.

[168] N. R. Heckenberg, R. McDuff, C. P. Smith, and A. G. White. Generation of optical phase singularities by computer-generated holograms. *Opt. Lett.*, 17:221–223, 1992.

[169] Z. S. Sacks, D. Rozas, and G. A. Swartzlander. Holographic formation of optical-vortex filaments. *Jr. Opt. Soc. Am. B.*, 15(8):2226–2234, 1998.

[170] J. Masajadaa, A. Popiołek-Masajadaa, and D. M. Wieliczkab. The interferometric system using optical vortices as phase markers. *Optics Commun.*, 207(1-6):85–93, June 2002.

[171] P. Senthilkumaran. Optical phase singularities in detection of laser beam collimation. *Applied Optics*, 42(31):6314–6320, 2003.

[172] V. Westphal and S. W. Hell. Nanoscale resolution in the focal plane of an optical microscope. *Phys. Rev. Lett.*, 94:143903, April 2005.

[173] M. D. Levenson, T. J. Ebihara, G. Dai, Y. Morikawa, N. Hayashi, and S. M. Tan. Optical vortex masks for via levels. *J. Micro/Nanolith. MEMS MOEMS.*, 3(2):293–304, April 2004.

[174] R. Menon and H. I. Smith. Absorbance-modulation optical lithography. *J. Opt. Soc. Am. A*, 23(9):2290–2294, 2006.

[175] A. Mair, A. Vaziri, G. Weihs, and A. Zeilinger. Entanglement of the orbital angular momentum states of photons. *Nature*, 412(7):313–316, 2001.

[176] H. H. Arnaut and G.A. Barbosa. Orbital and intrinsic angular momentum of single photons and entangled pairs of photons generated by parametric down-conversion. *Phys. Rev. Lett.*, 85(2):286–289, 2000.

[177] S. Franke-Arnold, S. M. Barnett, M. J. Padgett, and L. Allen. Two-photon entanglement of orbital angular momentum states. *Phys. Rev. A.*, 65(3):033823, 2002.

[178] M. Alshershby, Z. Hao, and Jingquan Lin. Guiding microwave radiation using laser-induced filaments: the hollow conducting waveguide concept. *J. Phys. D.*, 45:265401, 2012.

[179] R. Y. Chiao, E. Garmire, and C. H. Townes. Self-trapping of optical beams. *Physics Review Letter*, 13:479–482, 1964.

[180] K. D. Moll, G. Fibich, and A. L. Gaeta. Self-similar optical wave collapse: Observation of the townes profile. *Phys. Rev. Lett.*, 90:203902, 2003.

[181] V. I. Kruglov, Y. A. Logvin, and V. M. Volkov. The theory of spiral laser beams in nonlinear media. *J. Mod. Opt.*, 39:2277, 1992.

[182] Antoine Vincotte and Luc Berge. Femtosecond optical vortices in air. *Phys. Rev. Lett.*, 95:193901, 2005.

[183] L.T. Vuong, T.D. Grow, A. Ishaaya, A.L. Gaeta, G. W. Hooft, E. E. Eliel, and G. Fibich. Collapse of optical vortices. *Phys. Rev. Lett.*, 96: 133901, 2006.

[184] M. S. Bigelow, P. Zerom, and R. W. Boyd. Breakup of ring beams carrying orbital angular momentum in sodium vapor. *Phys. Rev. Lett*, 92:083902, February 2004.

[185] W. J. Firth and D. V. Skryabin. Optical solitons carrying orbital angular momentum. *Phys. Rev. Lett.*, 79:2450, September 1997.

[186] G. Fibich and N. Gavish. Critical power of collapsing vortices. *Phys. Rev. A.*, 77:045803, 2008.

[187] P. Polynkin, C. Ament, and J. V. Moloney. Self-focusing of ultraintense femtosecond optical vortices in air. *Phys. Rev. Lett.*, 111:023901, July 2013.

[188] H. I. Sztul, V. Kartazayev, and R. R. Alfano. Laguerre–gaussian supercontinuum. *Optics letters*, 31(18):2725–2727, 2006.

[189] D. N. Neshev, A. Dreischuh, G. Maleshkov, M. Samoc, and Y. S. Kivshar. Supercontinuum generation with optical vortices. *Opt. Express*, 18(17):18368–18373, 2010.

[190] R. A. Vlasov, V. M. Volkov, and D. Yu. Dedkov. Spectrum superbroadening in self-focusing of pulsed vortex beams in air. *Quantum Electroincs*, 43(2):157, 2013.

[191] M. Pitchumani, H. Hockel, W. Mohammed, and E. G. Johnson. Additive lithography for fabrication of diffractive optics," applied optics, vol. 41, no. 29, pp. 6176-6181, october 2002. additive lithography for fabrication of diffractive optics. *Applied Optics*, 41(29):6176–6181, 2002.

[192] A. Sukhinin and A. B. Aceves. Optical uv filament and vortex dynamics. *Journal of Optics*, 15:044010, 2013.

[193] M. Morgen, W. Price, L. Hunziker, P. Ludowise, M. Blackwell, and Y. Chen. Femtosecond raman-induced polarization spectroscopy studies of rotational coherence in o_2, n_2 and co_2. *Chem. Phys. Lett.*, 209: 1–9, 1993.

[194] G. Herzberg. *Molecular Spectra and Molecular Structure: I. Spectra of Diatomic Molecules*. Krieger Pub Co, New York, 1989.

[195] B. Friedrich and D. Herschbach. Alignment and trapping of molecules in intense laser fields. *Phys. Rev. Lett.* , 74:4623, 1995.

[196] H. Stapelfeldt and T.Seideman. Colloquium: Aligning molecules with strong laser pulses. *Rev. Mod. Phys.*, 75:543–557, 2003.

[197] T. Seideman and E. Hamilton. Nonadiabatic alignment by intense pulses. concepts, theory, and directions. *Adv. At. Mol. Opt. Phys.*, 52: 289–329, 2006.

[198] J. H. Eberly, N. B. Narozhny, and J. J. Sanchez-Mondragon. Periodic spontaneous collapse and revival in a simple quantum model. *Phys. Rev. Lett.*, 44:1323, May 1980.

[199] I. Sh. Averbukh and N. F. Perelman. Fractional revival: Universality in the long-term evolution of quantum wave packets beyond the correspondence principle dynamics. *Phys. Lett. A*, 139:449, 1989.

[200] V. Renard, O. Faucher, and B. Lavorel. Measurement of laser-induced alignment of molecules by cross defocusing. *Opt. Lett.* , 30:70, 2005.

[201] H. Cai, J. Wu, A. Couairon, and H. Zeng. Spectral modulation of femtosecond laser pulse induced by molecular alignment revivals. *Opt. Lett.*, 34:827–829, 2009.

[202] R. A. Bartels, T. C. Weinacht, N. Wagner, M. Baertschy, Chris H. Greene, M. M. Murnane, and H. C. Kapteyn. Phase modulation of ultrashort light pulses using molecular rotational wave packets. *Phys. Rev. Lett*, 88:013903, 2001.

[203] DW. Schumacher, F. Weihe, HG. Muller, and PH. Bucksbaum. Phase dependence of intense field ionization: A study using two colors. *Phys. Rev. Lett.*, 73:1344–1347, 1994.

[204] A. Azarm, S. Ramakrishna, A. Talebpour, S. Hosseini, Y. Teranishi, H. L. Xu, Y. Kamali, J. Bernhardt, S. H. Lin, T. Seideman, and S. L. Chin. Population trapping and rotational revival of N_2 molecules during filamentation of a femtosecond laser pulse in air. *J. Phys. B.*, 43: 235602, 2010.

[205] I. V. Litvinyuk, K. F. Lee, P. W. Dooley, D. M. Rayner, D. M. Villeneuve, and P. B. Corkum. Alignment-dependent strong field ionization of molecules. *Phys. Rev. Lett*, 90:233003, 2003.

[206] Andreas Velten, Thomas Willwacher, Otkrist Gupta, Ashok Veeraraghavan, Moungi G. Bawendi, and Ramesh Raskar. Recovering three-dimensional shape around a corner using ultrafast time-of-flight imaging. *Nature Communications*, 3(745):1181–1183, 2012. doi: 10.1038/ncomms1747.

[207] R. P. Fischer, A. C. Ting, D. F. Gordon, R. F. Fernsler, R. P. DiComo, and P. Sprangle. Conductivity measurements of femtosecond laser plasma laments. *IEEE Transactions on Plasma Science*, 35:1430–1436, 2007.

[208] J Papeer, M Botton, D Gordon, P Sprangle, A Zigler, and Z Henis. Extended lifetime of high density plasma filament generated by a dual femtosecond nanosecond laser pulse in air. *New Journal of Physics*, 16: 123046, 2014.

[209] Andreas Schmitt-Sody, A. Lucero, B. Kamer, and D. French. Plasma generation by laser filamentation ikn air. *IEEE transactions on plasma science*, 42:2692–2693, 2014.

[210] Daniil Kartashov, Skirmantas Alisauskas, Giedrius Andriukaitis, Audrius Pugzlys, Mikhail Shneider, Aleksei Zheltikov, See Leang Chin, and Andrius Baltuska. Free-space nitrogen gas laser driven by a femtosecond filament. *Physical Review A*, 86:033831, 2012.